

Electrical Impedance Based Spectroscopy and Tomography Techniques for Obesity and Heart Diseases

Thesis by

Shell Xiaoxiao Zhang

In Partial Fulfillment of the Requirements

for the degree of

Doctor of Philosophy

The logo for the California Institute of Technology (Caltech), featuring the word "Caltech" in a bold, orange, sans-serif font.

CALIFORNIA INSTITUTE OF TECHNOLOGY

Pasadena, California

2017

(Defended 09/20/2016)

© 2016

Shell Xiaoxiao Zhang

All Rights Reserved

To my father.

ACKNOWLEDGEMENTS

I would like to express my special appreciation and thanks to my advisor Professor Yu-Chong Tai. Professor Tai has been a tremendous mentor for the past five years for me. He has taught me how to conduct research in world class, and perhaps even more importantly, how to think deeply and critically about matters in hand. Professor Tai's never-ending supply of fresh ideas and enthusiasm for research has been a source of inspiration for my own work. I am extremely fortunate to have conducted my graduate work under his guidance.

I would like to thank Professor Hsiai for his guidance and invaluable effort in our collaboration. He was the steering wheel for our projects, without Professor Hsiai's efforts both the EIS and EIT project would not have reached their milestones.

I would like to express my gratitude towards my colleagues Dr. Luo Yuan, Dr. Lei Xu, and Dr. Ming Xu. My work would never have been successful without their dedication and tremendous effort to our project. I was very fortunate to have such capable and wonderful colleagues to be able to conduct and finish all aspects of both EIS and EIT projects. I would also like to acknowledge all members of Professor Tai's lab, who have helped me along the way, and have been inspirations and sounding boards of my research.

I would like to thank my parents. Especially my father, to whom this thesis is dedicated, who has inspired me and encouraged me to be curious through out my life. Father would

have been very proud of me today. Last but not least, I would like to thank my husband, Eduardo, who has given me unwavering support in whichever way I needed him. Without his encouragement and ideas, this Ph.D. would not have been possible.

ABSTRACT

Despite advances in diagnosis and therapy, atherosclerotic cardiovascular disease remains the leading cause of morbidity and mortality. Predicting metabolically active atherosclerotic lesions has remained an unmet clinical need. Specially, atherosclerotic plaques that are prone to rupture are of extremely high-risk and can cause detrimental heart attacks and/or strokes, leading to sudden death. It has been shown that atherosclerosis is correlated to the level of obesity of an individual [1] Usually in clinical practice, the doctor will assess a patient's "risk factor" based on his or her Body Mass Index (BMS), and measurement of the waist circumference. Meanwhile the level of fatty droplet deposits in the liver is an important bio-marker to assess the patient's risk factor, however the patient will need to undergo radiation imaging such as CT scan or MRI scan.

For the vulnerable plaques that can lead to sudden rupture, the ability to distinguish them at an early stage remains largely lacking. Therefore it is of great clinical interest to find improved diagnostic techniques to identify and localize such vulnerable plaques. Meanwhile, lipid has significantly lower electrical impedance than the rest of the vessel tissues in certain frequency bands [2]. In this thesis we explore spectroscopic and tomographic methods to characterize such plaques. In addition, with the Electrical Impedance Tomography method we will propose a novel method to detect fatty liver in an early stage with non-radiating and non-invasive manner.

PUBLISHED CONTENT AND CONTRIBUTIONS

Packard, R. R. S., Zhang, X., Luo, Y., Ma, T., Jen, N., Ma, J., Hsiai, T. K. (2016). Two-Point Stretchable Electrode Array for Endoluminal Electrochemical Impedance Spectroscopy Measurements of Lipid-Laden Atherosclerotic Plaques. *Ann Biomed Eng*, 44(9), 2695–2706. doi:10.1007/s10439-016-1559-9

Shell (Xiaoxiao) participated in the conception of the project, designed and fabricated the device, participated in the data collection during experiment, prepared the data, and participated in the writing of the manuscript.

Packard, Rene., Zhang, Xiaoxiao., Luo, Yuan., et al., “The next generation of stretchable sensors for intravascular electrochemical impedance spectroscopy of varying levels of lipid burden and atherosclerosis,” *American Heart Association (AHA) Health Tech, Session Title” Emerging Technologies (November 2015), vol. 132 no. Suppl 3 A18004. doi: 10.1016/j.bios.2013.11.059*

Shell participated in the conception of the project, designed and fabricated the device, participated in the data collection during experiment, prepared the data, and participated in the writing of the manuscript.

Zhao Y., Cao H., Beebe T., Zhang H., Zhang X., Chang, H., Scremin O., Lien C., Tai, YC. and Hsiai T., “Dry-contact microelectrode membranes for wireless detection of electrical phenotypes in neonatal mouse hearts,” *Biomedical Microdevices (2015), on pp. 17-40. doi:10.1007/s10544-014-9912y*

Shell participated in the conception of the project, designed and fabricated the device, participated in the data collection during experiment, prepared the data, and participated in the writing of the manuscript.

Cao, Hung, Fei Yu, Yu Zhao, Xiaoxiao Zhang, Joyce Tai, et al. "Wearable multi-channel microelectrode membranes for elucidating electrophysiological phenotypes of injured myocardium." *Integrative Biology* 6, no. 8 (2014): 789-795. doi:10.1039/c4ib00052h

Shell participated in the conception of the project, designed and fabricated the device, participated in the data collection during experiment, prepared the data, and participated in the writing of the manuscript.

Zhang, Xiaoxiao, Beebe Tyler, et al. "Wearable flexible micro electrode for adult zebrafish long term ecg monitoring," In *Micro Electro Mechanical Systems (MEMS), 2015 IEEE 28th International Conference*. doi:10.1109/memsys.2015.7051051

Shell participated in the conception of the project, designed and fabricated the device, participated in the data collection during experiment, prepared the data, and participated in the writing of the manuscript.

Zhang, Xiaoxiao, Joyce Tai, Jungwook Park, and Yu-Chong Tai. "Flexible MEA for adult zebrafish ECG recording covering both ventricle and atrium." In *Micro Electro Mechanical Systems (MEMS), 2014 IEEE 27th International Conference* on pp. 841-844. IEEE, 2014. doi:10.1109/memsys.2014.6765772

Shell participated in the conception of the project, designed and fabricated the

device, participated in the data collection during experiment, prepared the data, and participated in the writing of the manuscript.

Zhao, Yu, Fei Yu, Hung Cao, Honglong Chang, Xiaoxiao Zhang, Tzung K. Hsiai, and Yu-Chong Tai. "A wearable percutaneous implant for long term zebrafish epicardial ECG recording." In Solid-State Sensors, Actuators and Microsystems (TRANSDUCERS & EUROSENSORS XXVII), 2013 Transducers & Eurosensors XXVII: The 17th International Conference on, pp. 756-759. IEEE, 2013. doi:10.1109/transducers.2013.6626876

Shell participated in the conception of the project, designed and fabricated the device, participated in the data collection during experiment, prepared the data, and participated in the writing of the manuscript.

TABLE OF CONTENTS

Acknowledgements.....	ii
Abstract	iii
Published Content and Contributions.....	iv
Table of Contents.....	v
List of Figures and Tables.....	vi
Chapter I: Introduction.....	1
1.1 Bio-electricity in the human body.....	1
1.2 State of the art Bio-impedance based tools.....	3
1.3 Applications in this thesis.....	6
1.3.1 Endoluminal vulnerable plaque detection.....	7
1.3.1.1 Introduction to the disease.....	7
1.3.1.2 Current diagnostic tools and limitations.....	9
1.3.2 Fatty liver early detection.....	12
1.3.2.1 Introduction to the diseases.....	12
1.3.2.2 Current diagnostic tools and limitations.....	14
1.4 Safety considerations.....	14

1.5 Thesis organization.....	15
Chapter II: Electrical Properties of Biological Tissues.....	18
2.1 The cell.....	18
2.1.1 The Cell Membrane.....	18
2.2 Tissue as a Volume Conductor.....	21
2.2.1 Nernst Equation.....	22
2.3 Tissue as a Volume Conductor.....	25
Chapter III: Electrical Impedance Spectroscopy.....	29
3.1 Concept of AC impedance.....	30
3.2 The Sensitivity distribution.....	31
3.3 The electrode-electrolyte interface.....	37
3.4 Bode-plot and Nyquist plot.....	42
3.5 Lumped circuit model.....	46
Chapter IV: Electrical Impedance Tomography.....	49
4.1 The instrument and setup.....	49
4.2 The mathematical framework.....	54
4.2.1 The inverse problem.....	54

4.2.2 The forward problem.....	59
4.3 EIDORS Library.....	64
Chapter V: EIS for Endoluminal Plaque Detection.....	66
5.1 Two point vs. Four point electrode.....	68
5.2 Sensor design and fabrication.....	73
5.3 Animal experiments.....	75
5.3.1 <i>Ex-vivo</i> animal experiments.....	75
5.3.2 <i>In-vivo</i> animal experiments.....	80
Chapter VI: EIT for Endoluminal Plaque Detection.....	85
6.1 Electrode configuration.....	85
6.2 Resolution study.....	87
6.3 Simulated experiments.....	96
6.4 <i>Ex-vivo</i> experiments.....	98
Chapter VII: EIT for Fatty Liver Early Detection.....	103
7.1 Electrode configuration.....	103
7.2 Conductivity of organs and Multi-frequency difference imaging...	104
7.3 Simulated experiments.....	106

7.4 Phantom experiments.....	112
7.5 <i>Ex-vivo</i> experiments.....	119
7.6 <i>In-vivo</i> human experiments.....	122
Chapter VIII: Conclusions.....	127
Bibliography.....	129
Appendix A: Partial Matlab Code.....	144

LIST OF FIGURES AND TABLES

<i>Number</i>	<i>Page</i>
1. Fig. 1.3.1.1.1: Histology of a lipid-rich “vulnerable” coronary plaque.	Pg 8
2. Fig. 1.3.1.1.2: Morphological traits associated with vulnerable plaques	Pg 8
3. Table. 1.3.1.2.1: Comparison of Noninvasive and Invasive imaging modalities for detection of individual characteristics of vulnerable plaques.....	Pg 11
4. Fig. 2.1.1: A diagram illustrating how the phosphoglyceride (or phospholipid) molecules behave in water.....	Pg 20
5. Fig. 2.1.2: The structure of a cell membrane with one ion channel.....	Pg 20
6. Fig. 2.3.1: Diagram of equivalent circuit of a cell model.....	Pg 27
7. Fig. 2.3.2: Permittivity variation of a tissue as a function of frequency.....	Pg 28
8. Fig. 3.1: Energy vs. frequency band for Electromagnetic waves.....	Pg 31
9. Fig 3.2.1: volume conductor with four electrode.....	Pg 35
10. Fig. 3.4.1: Esin and Markov, Grahame, and Devanathan model.....	Pg 40

11. Fig. 3.4.2: Randle's circuit.....	Pg 41
12. Fig. 3.4.3: Electrode-electrolyte equivalent circuit w/ small perturbation.....	Pg 41
13. Fig. 3.5.3: Effect of Structural Design of Silver/Silver Chloride Electrodes on Stability and Response Time	Pg 43
14. Fig. 3.5.1.: Simulated amplitude Bode plot (up) and phase Bode plot (down) based on Randle's circuit in Fig. 3.4.2.....	Pg 45
15. Fig. 3.5.2: Simulated Nyquist plot of a of an ideal Randle's circuit based on Randle's circuit in Fig. 3.4.2.....	Pg 46
16. Fig. 3.5.1: tissue and electrode model for EIS measurement.....	Pg 47
17. Fig. 3.5.2: equivalent circuit of tissue and electrode model.....	Pg 48
18. Fig. 3.5.3: Impedance Bode-plot on log-log scale showing three corners....	Pg 49
19. Fig 4.1.1: System diagram of the Labview Based system.....	Pg 51
20. Fig 4.1.2: Pre-amp circuit diagram.....	Pg 52
21. Fig 4.1.3: Time domain waveforms.....	Pg 53

22. Fig 4.1.4: Swisstom noise performance over 10 consecutive frames. LabView noise plot.....Pg 54

23. Figure 5.1.1: (a): meshed artery segment with lesion..... Pg 72

24. Figure 5.1.2: sensitivity field of different lengthsPg 74

25. Figure 5.2.1: (a) Design diagram of the Parylene-C electrode design.....Pg 75

26. Figure 5.2.2: Finished integrated catheter device.....Pg 76

27. Figure 5.3.1.1: Bottom: Parylene-C based micro electrode array.Pg 77

28. Figure 5.3.1.2: (a): ex-vivo mouse aorta EIS measurement setup. Pg 78

29. Figure 5.3.1.3: Left: Impedance amplitude and phase curves of lean muscle.
Right: Impedance amplitude and phase curves of fat..... Pg 79

30. Figure 5.3.1.4: Impedance modulus of sample I, II and III mice aortas..... Pg 79

31. Figure 5.3.2.1: Finished integrated catheter device.....Pg 82

32. Figure 5.3.2.2: (a) & (b) Intravascular Ultrasound (IVUS) images of aorta intersection.....Pg 84

- 34. Figure 5.3.2.3: EIS results from different sites showing the impedance (top) and phase (bottom) differences between plaques of conditions from control (i.e., no plaque) to severe plaque.....Pg 85

- 35. Fig 6.1.1 Inward imaging and outward imagingIn contrast to inward imaging, as a new imaging modality, we have developed “outward imaging”. Pg 88

- 36. Fig 6.2.1: Spread vs. number of electrodes. Spread is defined by the area of the reconstructed image divided by the area of the real object..... Pg 89

- 37. Fig 6.2.1: Reconstructed image of same 1mm diameter object placed at different distances away from the probe edge..... Pg 90

- 38. Fig 6.2.2: 100um – 2mm distances (first row of Fig 6.2.1) after 10% threshold crop, we define these to be the constructed object size..... Pg 90

- 39. Fig 6.2.3: left: resolution vs. distance. Right: spread vs. distance..... Pg 91

40. Fig 6.2.4: reconstructed image of radius r at distance 100 μ m from the probe edge..... Pg 92

41. Fig 6.2.5: 10% threshold cropped images from Fig 6.2.4, used to define the reconstructed image area and size.....Pg 93

42. Fig 6.2.6: Left: resolution of the reconstructed image with radius r at distance 100 μ m to probe edge. Right spread of the reconstructed image with radius r at distance 100 μ m to probe edge. Distance and object size.....Pg 94

43. Fig 6.2.7 Combined result of varied radius vs. varied distance.....Pg 95

44. Fig 6.2.8: Left: resolution vs. distance (blue object $r = 0.5$ mm, red $r = 2$ mm, green $r = 4$ mm) Right: spread vs. distance (blue object $r = 0.5$ mm, red $r = 2$ mm, green $r = 4$ mm)..... Pg 95

45. Table 6.3.1: Conductivity values used in FEM simulation.....Pg 97

46. Fig 6.3.1: (a) 3D FEM model used generated with Netgen..... Pg 98

47. Fig 6.4.1: Top left: electrode in saline. Top right: electrode zoom-in view.
Middle row: “pen in saline” experiment setup. Bottom row: reconstructed images corresponding to pen location..... Pg 100
48. Fig 6.4.2: (a) shows the EIT imaging results with the swine aorta sample and subcutaneous fat mimicking plaques through implementing a one-step fast algorithm..... Pg 101
49. Fig 6.4.3: (a) red-blue scale reconstructed image with ex-vivo aorta tissue..... Pg 102
50. Fig. 6.4.4: phantom tank with $\frac{1}{8}$ normal saline conductivity agar gel and $\frac{1}{4}$ normal saline background. Pg 118
51. Fig. 6.4.5: Difference imaging reconstruction Pg 119
52. Fig. 6.4.6: Absolute imaging reconstruction. The scale bar shows correct conductivity reading. Pg 119
53. Fig. 7.1.1: relative position of liver inside the human body..... Pg 123
54. Fig. 7.1.2: (a): CT scan of upper abdominal cross section. (b) major organ highlighted (large blue region is liver)..... Pg 123

55. Fig. 7.1.3: electrode placement on human thorax..... Pg 124

56. Table 7.2.1: conductivity major abdominal tissues from literature Pg 125

57. Fig 7.2.2: The effect of temperature on the electrical impedance spectra of
(a) 100% liver and (b) 100% fat..... Pg
126

58. Fig. 7.3.1: Left: FEM model used to generate voltage data. Right:
Conductivity of each organ at 50Khz and
250Khz. Pg 127

59. Fig. 7.3.2: From left to right: 100% liver conductivity (healthy), 95%
conductivity, 90% conductivity, 80% conductivity, and 70%
conductivity..... Pg 128

60. Fig 7.3.3: Reconstructed “effective” conductivity in the liver region vs.
the modeled liver conductivity plot..... Pg
129

61. Fig 7.3.4: Left: FEM model used to generate voltage data. Right:
Reconstructed image with 1% added random
noise..... Pg 130

62. Fig. 7.3.5: Left: FEM model (b) reconstructed image with inaccurate thorax geometry

Pg 130

63. Fig. 7.3.6: Left: FEM model used for simulation study based on the CT scan. Right: CT scan image (mirrored).....

Pg 131

64. Fig. 7.3.7: (a) FEM model to generate voltage data (b) nconstrained higher order solver (c) smoothness constrain with a priori matrix in the liver region (d) smoothness constrain with a priori matrix in the liver region with shape

error..... Pg 134

65. Fig. 7.4.1: Left: tank setup with 32 stainless steel

electrodes..... Pg 140

66. Fig. 7.4.2. (a)(b)sensitivity field of adjacent injection pattern (c)(d) sensitivity field of opposite injection

patter..... Pg 146

67. Fig. 7.4.3 current lines near electrode with different contact impedance values from $z=0.01$ Ohm to $z = 10$ Ohm. Pg 146

68. Fig. 7.4.4: Top: electrode pair contact impedance in series with saline. Bottom: Calculated contact impedance for each electrode. The last impedance is the resistance of saline..... Pg 148

69. Fig. 7.4.5: Left: reconstructed image with no contact impedance. Right: reconstructed image with calculated contact impedance incorporated..... Pg 148

70. Fig. 7.5.1: Impedance modulus (left) and phase angle (right) EIS with two electrode method..... Pg 150

71. Fig. 7.5.2: Agar gel mimicing subcutaneous fat in saline. Left: experimental setup. Right: Reconstructed image..... Pg 150

72. Fig. 7.5.3: Subcutaneous fat experiment with pork fat in saline. Left: experimental setup. Right: Reconstructed image..... Pg 151

73. Fig. 7.5.4: Liver experiment with pork liver. Left: experimental setup..... Pg 122

74. Fig. 7.6.1: Electrode numbering on test person..... Pg 153

75. Fig. 7.6.2: Left: experiment setup. Right: Reconstructed image with location difference data. Pg 154

76. Fig. 7.6.3: Left: two male test subjects with electrode belt position shown. Right: Reconstructed images correspondingly.....Pg 155

77. Fig. 7.6.4: Reconstructed images with conductivity readings from simulation study ignoring different neighboring electrodes. Pg 155

Chapter 1

INTRODUCTION

1.1 Bio-electricity in the human body

An important area of research concerns itself with the theoretical, modeling, and experimental results of current flow through and on the boundary of human tissue. Current flow within tissue is the result of electric potential gradients as part of internal biological functions as observed in cardiomyocytes and neurons. This line of research started in 1876 when Luigi Galvani began investigating the effect of current flow through the legs of frogs. Today cable theory with its mathematical derivatives provides a solid model for understanding neuronal electronic potentials.

Current can also flow through tissue from active injection from outside the solid body. The key characteristic of current flow through human tissue is called bio-impedance and is modulated by tissue type and physiological tissue status. Capacitors in a circuit delay current flow, for any complex circuit such as the human body, there will be a delay caused by the body's overall Reactance to current flow. Reactance is analogous to resistance, a high reactance has a high effective resistance to alternating current. Like resistance, its value is in Ohms, but it depends on the applied frequency. There is a large

resistivity contrast (up to about 200:1) between a wide range of tissue types in the human body (Geddes and Baker, 1967). It is this characteristic of tissue that has been utilized to differentiate between tissue and reconstruct spatial impedance maps of solid bodies. These impedance maps are calculated as an inverse problem using Laplace's equation. This way to visualize the human body is commonly known as electrical impedance tomography. EIT adds a soft field imaging modality to the repertoire of hard field imaging techniques in prevalence today.

1.2 Bio-impedance based diagnosis

Let us use the term EI imaging as an umbrella for various bio-impedance based imaging modalities which include EIS electrical impedance spectroscopy, EIT electrical impedance tomography, EFT electrical field tomography, MREIT magnetic resonance electrical impedance tomography, and MIT magnetic induction tomography.

Electrical Impedance Spectroscopy (EIS), This modality measures the impedance of a solid body over a range of frequencies, and therefore the frequency response of the body. The properties that can be resolved include the energy storage and dissipation property. Data from EIS is often represented as a Nyquist plot.

Electrical impedance Tomography (EIT), is a non-invasive medical imaging modality in which an image of the conductivity or permittivity of part of the body is inferred from surface electrode measurements. EIT systems typically apply alternating currents at a single frequency. EIT systems can also use multiple frequencies to better differentiate

between normal and suspected abnormal tissue within the same organ (multifrequency-EIT).

Electric Field Tomography (EFT), is an imaging modality which enables contact-less sensing of spatial impedance maps in solid bodies. The body is probed by alternating quasistatic electric fields, with wavelengths much longer than the object of interest. Free charge carriers in the solid body can not redistribute immediately to compensate for changes in the external field producing a weak secondary field (Maxwell-Wagner relaxation) This weak secondary field depends on the conductivity, permittivity, geometry, and frequency of active current.

Magnetic Resonance Electrical impedance Tomography (MREIT), Is a dual imaging modality that utilizes the internal data of magnetic flux density in addition to the boundary current-voltage measurements to stitch together three-dimensional maps of conductivity and current density distributions.

Magnetic induction tomography (MIT) is an imaging modality used to image electromagnetic properties of an object by using the eddy current effect.

EIT has been adopted in clinical practice by the medical professionals due to its lower cost with respect to traditional imaging modalities such as Magnetic Resonance Imaging (MRI). Both from a capital layout and operation cost perspective, EIT is orders of magnitude cheaper than Magnetic Resonance Imaging MRI, Computed Tomography CT,

or Positron Emission Tomography PET. The size, weight and complexity of the probing apparatus and processing hardware is also greatly reduced with EIT.

The need for robust and cost effective imaging solutions for the medical industry is driven by the ever greater use of imaging modalities for the diagnosis and treatment of human pathologies. Clinically EIT has found strong uptake in the monitoring of human lungs, and cardiac function. Bedside monitoring of pulmonary and cardiac function is ubiquitous in hospitals around the world and makes a good target for EIT. These applications do not require high spatial image resolution but do require continuous non-invasive, low-power monitoring. Imaging of the human thorax with EIT was done at its inception by Henderson and Webster [3], using an array of 100 electrodes and sampling at 32 frames per second. The breakthrough in EIT for clinical use came with the design of robust electrodes that minimize contact impedance and their configuration into a belt for ease of application onto the patient. The Dräger company (Germany) has been a pioneer in bringing EIT to the marketplace for the monitoring of pulmonary ventilation. In a similar vein to lung ventilation EIT has been widely used for the study of gastric emptying. Many pathological conditions are associated with delayed gastric emptying; common causes are gastroparesis secondary to diabetes, surgery, gastric ulcer, or gastritis. EIT is applied to the measurement of gastric motility by imaging conductivity changes in the abdomen after ingestion of liquid.

Because electric properties of tissues are correlated with cell fluids, membranes, cell structure, any change to the measure of electrical scalar potential distribution and current flow through the body is a change in impedance due to a pathology or biological function change in the body. A transient decrease of cell membrane resistance during activity was proven by the experiments of Cole and Curtis [4]. Weinhold et al. [5] have used thoracic electrical impedance measures for early diagnosis of organ rejection in transplant recipients. Differentiation of tissue has been long researched but has not found its way into wide clinical adoption and points to an under-served opportunity.

1.3 Applications in this thesis

In this thesis we explore impedance based diagnoses for two important diseases: endoluminal vulnerable plaque detection and fatty liver early detection. Despite advances in diagnosis and therapy, atherosclerotic cardiovascular disease remains the leading cause of morbidity and mortality. Predicting metabolically active atherosclerotic lesions has remained an unmet clinical need. Specially, atherosclerotic plaques that are prone to rupture are of extremely high-risk and can cause detrimental heart attacks and/or strokes, leading to sudden death. It has been shown that atherosclerosis is correlated to the level of obesity of an individual [1] Usually in clinical practice, the doctor will assess a patient's "risk factor" based on his or her Body Mass Index (BMS), and measurement of the waist circumference. Meanwhile the level of fatty droplet deposits in the liver is an important bio-marker to assess the patient's risk factor, however the patient will need to undergo radiation imaging such as CT scan or MRI scan.

For the vulnerable plaques that can lead to sudden rupture, the ability to distinguish them at an early stage remains largely lacking. Therefore it is of great clinical interest to find improved diagnostic techniques to identify and localize such vulnerable plaques. Meanwhile, lipid has significantly lower electrical impedance than the rest of the vessel tissues in certain frequency bands [2]. In this thesis we explore spectroscopic and tomographic methods to characterize such plaques. In addition, with the Electrical Impedance Tomography method we will propose a novel method to detect fatty liver in an early stage with non-radiating and non-invasive manner.

1.3.1 Endoluminal Vulnerable Plaque Detection

1.3.1.1 Introduction to the Disease

Although formation of atheromatous plaque has been well understood and lesion types characterized, the concept of the “vulnerable” plaque is a novel one. [6] The term vulnerable plaque refers to a subgroup of often modestly stenotic plaques yet prone to rupture. The ruptured plaque often results in acute coronary syndromes, and sudden cardiac death. The lack of prior symptoms make this disease especially dangerous.

Postmortem evaluation shows that these rupture-prone vulnerable plaques share certain characteristics: a thin fibrous cap (usually $<65 \mu\text{m}$), a large lipid-rich pool inside (See Fig. 1.3.1.1.1), and increased macrophage activity. Plaque disruption is ultimately triggered by extrinsic forces, including shear stress and wall stress. Rupture of the cap releases pro-coagulant factors leading the potential for an acute coronary event [7].

Despite the on-going research effort and the progress that has been made, however, the exact factors that determine the fate of a plaque rupture are still unknown to-date.

There are currently several diagnostic tools that attempt to diagnose vulnerable plaques based on the above mentioned common characteristics. In the following section a brief overview of the state of the art diagnostic tools are provided.

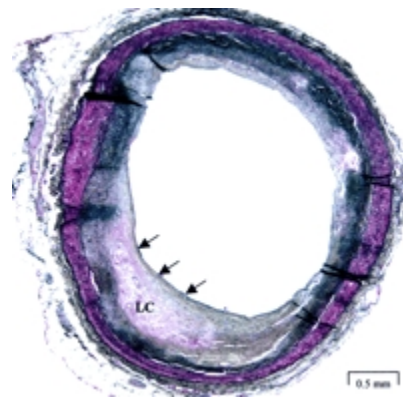


Fig. 1.3.1.1.1: Histology of a lipid-rich “vulnerable” coronary plaque. The thin fibrous cap is pointed to by arrows and lipid core is marked as “LC”. These are the known features of vulnerable plaque.

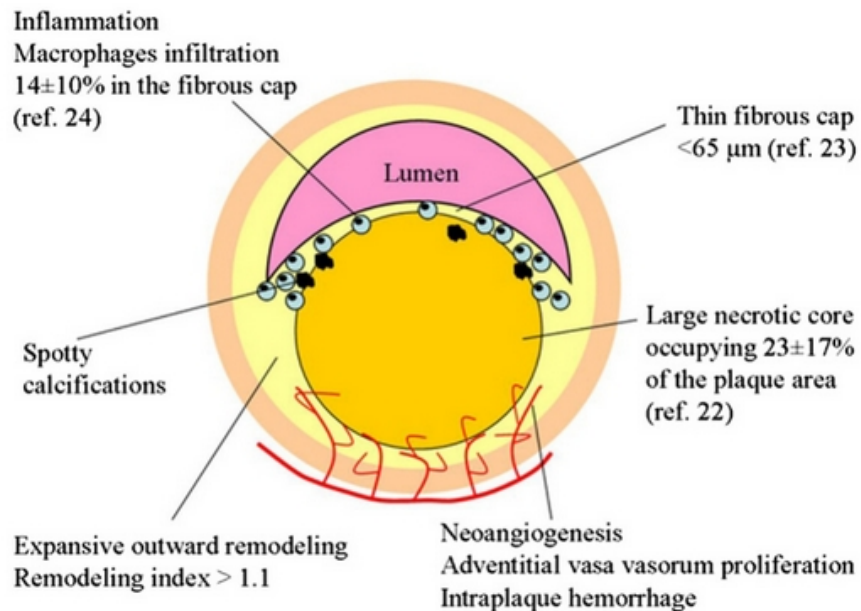


Fig. 1.3.1.1.2: Typical morphological traits associated with vulnerable plaques

1.3.1.2 State of the Art Diagnostic Tools and Limitations

In recent years, cardiovascular research has sought potential strategies for detecting high-risk plaques before their disruption. These potentially powerful techniques are aimed at identification of populations at risk and plaque monitoring and might eventually guide targeted therapy.

Angioscopy: Angioscopy is the “gold stand” of characterizing the blockage of atherosclerosis. However since the vulnerable plaque is not characterized by its blockage of the lumen but rather most has an outward remodeling (meaning they expand outward expanding the artery vessel), Angioscopy is of limited benefit to the vulnerable plaque detection.

Intra-vascular Ultrasound (IVUS): Intravascular ultrasound (IVUS) is one of the first techniques used to assess the morphological features of coronary plaques. An interrogation catheter enters through the femoral artery into the coronary artery. The head of the IVUS transducer spins, meanwhile it sends out and receives a reflected ultrasound signals. Ultrasound is based on The received reflected amplitude data are then stitched to make a cross-sectional view of the artery wall. Ultrasound is a density based imaging modality, so for matters of similar density the brightness of the displayed image will be similar as well. The intensity of the backscatter signal is processed into gray scale with a spatial resolution of 150 μ m at a frame rate of 10 to 30 frames/s. IVUS provides

information on the anatomical characteristics of the plaque but, to a lesser extent, on its composition [8,9] it is hard to distinguish the lipid core from other kinds of tissues. Because of this IVUS is hardly used alone in the detection of vulnerable plaques.

IVUS-radiofrequency analysis (IVUS-RF): Making use of the phase data as well as the amplitude data can overcome some of the limitations inherent to conventional gray-scale IVUS imaging. Different tissue will cause difference in delay of the reflected signal. Different mathematical methods have been used for RF data analysis, including autoregressive modeling (known as virtual histology [VH]), fast Fourier transformation, and wavelet analysis. IVUS-RF as an area of active research, has become a promising tool in determining the tissue content.

Coherence Tomography (OCT): OCT was developed for cross-sectional imaging in biological systems. OCT uses low-coherence interferometry to generate a 2-dimensional image of optical scattering. Due to the optical frequency the resolution is very good (4 to 20 μm), which constitutes a definite advantage as an imaging tool. However, also because OCT uses optical frequency signal, it has limited tissue penetration (2 to 3 mm), and the signal is attenuated by blood and requires the use of saline flushes, occlusion balloons, or other techniques to obtain good-quality images.

Intra-vascular Magnetic Resonance (IVMRI): Pulsed field gradient magnetic resonance imaging (MRI) has recently been used to calculate the water diffusion coefficient in atherosclerotic plaques [10]. Because water diffusion is less in lipid-rich than in fibrous plaques, this approach offers the opportunity to assess and quantify lipid

content in vessels with plaque. The spatial resolution is about 100 μm . However, the need to stabilize the catheter by use of an occlusion balloon and to mechanically rotate the catheter are the main limitations of this new method.

Near-Infrared Spectroscopy (NIRS): Near-infrared spectroscopy (NIRS) is based on the absorbance of light by organic molecules. Because different molecules absorb and scatter near-infrared light differently [11], NIRS enables chemical characterization of biological tissues and can be used to assess lipid and protein content in atherosclerotic plaques. Although looking to be a potentially very useful tool, further studies are nonetheless needed to establish the accuracy and reproducibility of this new method.

Intra-vesicular Thermography: Thermography is based on the assumption that plaque inflammation produces heat that can be measured at the surface of the plaque with a dedicated catheter [12]. Because vulnerable plaques are more cellular and inflammatory than stable plaques, they could be detected with this technique. Ex vivo experiments on carotid samples have shown that plaque temperature correlated positively with cell density and macrophage content and inversely with plaque thickness and the distance between the cell clusters and the luminal surface [13-15]. The major limitation of the method relates to the blood flow “cooling effect”, which might require systematic interruption of blood flow to achieve consistent and reproducible results [16].

Imaging Modality	Resolution	Penetration	Fibrous Cap	Lipid Core	Inflammation	Calcium	Thrombus	Current Status
IVUS	100 µm	Good	+	++	–	+++	+	CS/CA
Angioscopy	UK	Poor	+	++	–	–	+++	CS/CA*
OCT	10 µm	Poor	+++	+++	+	+++	+	CS
Thermography	0.5 mm	Poor	–	–	+++	–	–	CS
Spectroscopy	NA	Poor	+	++	++	++	–	PCS
Intravascular MRI	160 µm	Good	+	++	++	++	+	PCS
NA indicates not applicable; CS, clinical studies; CA, clinically approved for commercial use; CA								
*, clinically approved commercial use in Japan; PCS, preclinical studies; UK, unknown.								
+++ = sensitivity > 90%; ++ = sensitivity 80% to 90%; + = sensitivity 50% to 80%; [en] = sensitivity < 50%.								

Table. 1.3.1.2.1: Comparison of Noninvasive and Invasive imaging modalities for detection of individual characteristics of vulnerable plaque [17].

1.3.2 Fatty Liver Early Detection

1.3.2.1 Introduction to the Disease

Nonalcoholic fatty liver disease (NAFLD) is a term used to describe the accumulation of fat in the liver cells of an individual who drinks little or no alcohol. Such accumulated fat can cause inflammation and scarring in the liver and eventually may lead to liver failure.

The NAFLD is characterized by four stages:

Simple fatty liver (steatosis): a largely harmless build-up of fat in the liver cells that is without any symptoms.

Non-alcoholic steatohepatitis (NASH): a more serious form where liver has become inflamed. An early fatty liver detection focuses on detecting the NAFLD in this stage so that preventative measures can take place.

Fibrosis: where persistent inflammation causes scar tissue around the liver and nearby blood vessels. Liver is still able to function normally at this stage.

Cirrhosis: the most severe stage, occurring after years of inflammation, where the liver shrinks and becomes scarred and lumpy. Such damage is permanent and can lead to liver failure and liver cancer.

NAFLD tends to develop in people who are overweight or obese or have diabetes, high cholesterol or high triglycerides. According to the American Liver Foundation up to 25% of the general population in the United States are affected by NAFLD. Furthermore evidence to date confirms that early stage NAFLD has a probability of 18%–39% to progress to more advanced stages of hepatic fibrosis within a few years [18-20]. Given the current high prevalence of NAFLD in the general population and earlier intervention may reduce overall mortality [21], it has even been suggested that early liver biopsy may be indicated in all NAFLD patients.

In addition, recently there has been growing evidence that Nonalcoholic Fatty Liver is closely correlated to the risk of rupture-prone vulnerable artery plaques [22]. Nonalcoholic hepatic steatosis can be a valuable predictor of high-risk plaques.

1.3.2.2 State of the Art Diagnostic Tools and Limitations

Currently, the diagnosis of NAFLD requires biopsy and liver histology results. Liver biopsy is considered the gold standard to detect and stage liver cell injury from NAFLD [23-26]. However, liver biopsy has several disadvantages, one of the biggest being its invasive nature, others including sampling error, inter- and intra- variability, poor patient acceptance, and potential complications including excessive bleeding and death [21-23]. On the other hand, traditional imaging modalities, such as ultrasound, computed tomography [CT], and magnetic resonance [MR] imaging can help to detect the presence of hepatic steatosis; however, none of them can help to distinguish necroinflammation and mild fibrosis from simple steatosis. New noninvasive methods have been in development to distinguish necroinflammation, mild fibrosis and steatosis and have shown promising results, yet further validation is still required [27-29]. Based upon the fact that each biological tissue has distinguishable electrical characteristics, Electrical Impedance tomography presents a new way of diagnosing the stage of the fatty liver condition by determining the liver's electrical impedance.

1.4 Safety Considerations

All systems that measure transfer impedance from biological tissue require the maximum electrical current injection level: too high of the injection current can cause undesirable effects to the patient such as electrolysis, heating and neuromuscular stimulation. A current level that starts to cause sensation is called the threshold current . This threshold of sensation rises with increasing frequency of applied current (Brown et al 1999 [30]).

Once a current is applied through the skin through electrode, based on the current density into the tissue the membrane potential of some neurons may cause cell activation, and such activated cells will activate its neighboring neurons thus cause propagation of a nerve action potential. With higher frequency the neuron cells will not be able to react to the fast oscillating electrical field to undergo activation and propagation, hence neural stimulation will not occur. Hence the threshold current increases as injection current frequency increases.

Among the activation of excitable cells by injected current, the most dangerous is vagal and myocardial stimulation, either of which can cause ventricular fibrillation. It is generally agreed that safe intensity level of the injected current at the body surface should be lower than 1 mA_{rms} at a frequency of 100 Hz Valentinuzzi (1996) [31]. According to the IEC601 regulations, the maximum direct current, i.e. current at zero frequency, must be less than 10 μA_{rms} and less than 100 μA_{rms} at 1 kHz. IEC601 also establishes the maximum root-mean-square current for frequencies above 1 kHz, which must be calculated according to equation 1.4.1 with an upper limit of 10 mA_{rms}.

$$I_{\max}(f) = 10^{-7} \cdot f \quad 1.4.1$$

Where f is the frequency of the injection current.

1.5 Thesis Organization

Chapter 1 gives an introduction to the use of electrical impedance as a diagnostic tool in clinical applications and includes brief review of the state of the art electromagnetic

based tools in use today. The second half of Chapter 1 describes the applications explored in this thesis which includes an introduction to the disease itself and the state of the art diagnostic tools and their limitations.

Chapter 2 reviews the bio-tissue's electrical characteristics, starting with the single cell and its structure, arriving at the concept of volume conductor and tissue's conductivity and permittivity, and finally introducing lumped circuit models for electrode-tissue interface and the biological tissue.

Chapter 3 reviews the basis of electrical impedance spectroscopy which includes the concept of sensitivity distribution which is useful for both EIS and EIT.

Chapter 4 reviews the basis for electrical impedance tomography. In this chapter the hardware design and implementation is first presented. The mathematical framework is then laid out for the reconstruction where higher order approximations are also included in a brief discussion at the end.

Chapter 5 presents the experimental EIS result for vulnerable plaque diagnostics investigation. First, the 2-electrode and 4-electrode schemes are discussed and compared. Second data from both schemes are presented. In the end ex-vivo and in-vivo data with New Zealand White Rabbit data with micro fabricated EIS intra-vascular catheter is presented and discussed.

Chapter 6 presents the experimental EIT result for vulnerable plaque diagnostics investigation. These experiments use a novel “outward” imaging scheme. This chapter

start with a simulated study to explore the achievable resolution in our given parameters. Second, tank experiment with a moving pen is first demonstrated to prove the imaging capacity of the system, then image of ex-vivo data with pig aorta with fatty tissue mimicking vulnerable plaque is presented.

Chapter 7 presents the experimental EIT result for non-invasive fatty liver early detection investigation. These experiments are novel in the sense of the application. It is for the first time known to author of the thesis that EIT is tested for a diagnostic tool for the fatty liver disease. This chapter starts with simulated studies, a new a priori matrix is proposed to better estimate the conductivity values. It then follows with “agar gel in the tank experiment”, afterwards tank and ex-vivo tissues (fatty tissue and liver) in tank experiments demonstrated. In the end preliminary human experiments are presented. Both difference and absolute imaging are used throughout the chapter, showing the potential for estimating the absolute liver conductivity promising.

Finally, Chapter 8 includes conclusions of previous work and suggestions for future work.

ELECTRICAL PROPERTIES OF BIOLOGICAL TISSUES

2.1 The Cell

In order to understand the electrical properties of biological tissues, we need to start with its building block – the cells. Of course there are many kinds of cells in a human body in terms of biological functionality, here we categorize them based on whether a cell can produce electrochemical impulses. The first category is excitable cells, namely the muscle cells, nerve cells and some endocrine cells. The other category is non-excitable cells, which includes all other cells in the body (fat cells for example).

Among the excitable cells, the most common are nerve cells and muscle cells. For both types the cell membrane can produce electrochemical impulses and conduct them along the cell membrane. For the excitable endocrine cells (such as β cells in the pancreas) the electrochemical impulse on the membrane is known to start the physiological function of the cell. The origin of the membrane potential are the same for all excitable cells.

2.1.1 The Cell Membrane

For both excitable cells and non-excitable cells, the cell's content is enclosed by a membrane whose thickness is about 7.5 nm - 10.0 nm. The membrane structure mainly consists of fatty acids called *phosphoglycerides*. A phosphoglyceride is made up of

phosphoric acid and fatty acids called *glycerides* (see Figure 2.3). The head of this molecule is phosphoglyceride, which is *hydrophilic*. The tail consists of hydrocarbon chains which are *hydrophobic*. This polar structure give rise to the elementary cell membrane structure.

If fatty acid molecules are placed in water, they form clumps (see Fig. 2.1.1(B)), with the hydrophilic acid heads attracted to water on the outside, and the hydrophobic hydrocarbon tails repelled by water on the inside. If these molecules are very carefully placed on a water surface, the hydrophilic heads will be attracted to the water molecules and the tails repelled outside of the water boundary (See Fig. 2.1.1(C)). If we pack The acid heads would protrude into the water on each side and the hydrocarbons would fill the space between. This bilayer is the basic structure of the cell membrane. Another stable form in water is a bi-layer structure shown in Fig. 2.1.1(D). At relatively low concentrations, fatty acids will form micelles, which can be thought of as tiny spheres of fatty acids. At higher concentrations and under the appropriate pH conditions, fatty acids micelles can form vesicles, which is the bilayer structure described above. Such bi-layer vesicles are the basic structure of a cell membrane.

In the cell membrane there are pore-forming proteins making up what is called *ion channels*. From the bio-electric viewpoint, the *ionic channels* play an important role in maintaining a *resting membrane potential*. The *ion channels* are macromolecular pores through which sodium, potassium, and chloride ions flow through the membrane. The

flow of these ions forms the basis of bio-electrical phenomena. Fig. 2.1.2 illustrates the construction of a cell membrane.

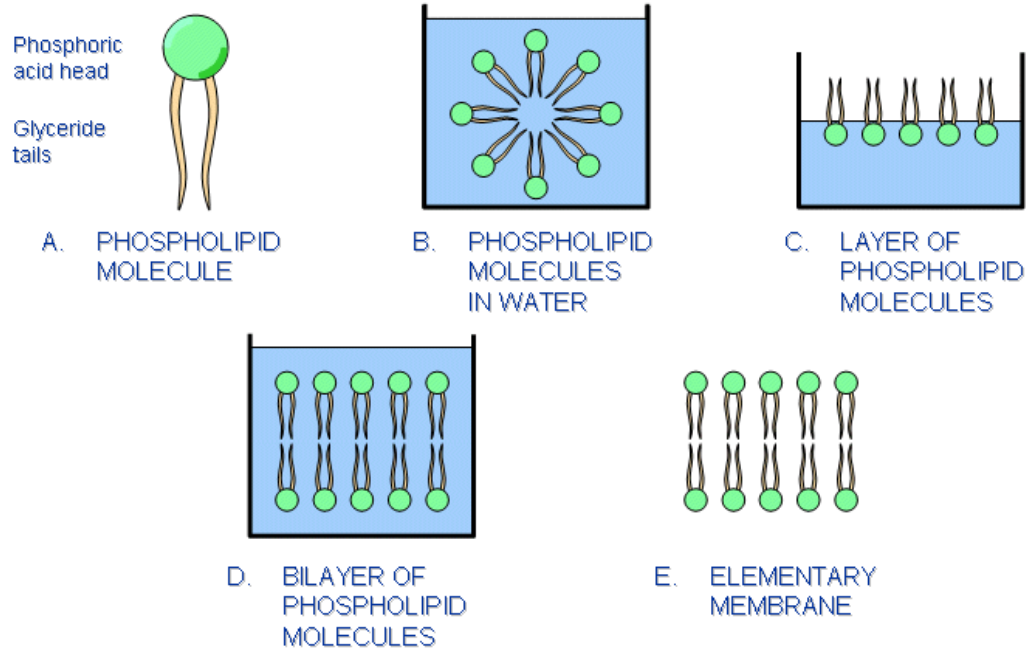


Fig. 2.1.1: A diagram illustrating how the phosphoglyceride (or phospholipid) molecules behave in water.

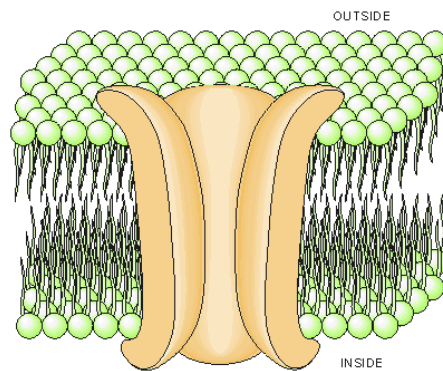


Fig. 2.1.2: The structure of a cell membrane with one ion channel.

2.2 Sub-threshold Cell Membrane models

By regulating ion movements between the extracellular and intracellular spaces, the cell membrane plays an important role in establishing the resting and active electrical properties of an excitable cell. The ease with which an ion crosses the membrane, the *membrane permeability* differs significantly within an ion channel, this characteristic is named as the ion channel's *selective permeability*. Activation of a cell affects its ion channels' behavior by altering these permeabilities. Another important consideration for trans-membrane ion movement is the fact that the ionic composition inside the cell differs greatly from that outside the cell. Consequently, concentration gradient is the driving force for all permeable ions that contribute to the net ion movement or flux.

Due to the selective permittivity, certain species of ions tend to accumulate at the inner and outer membrane surfaces (a diffusion process), which establishes potential difference, hence an electric field within the membrane. This electric field become the driving force for additional ion flow. Thus to describe membrane ion movements electric-field forces as well as diffusional forces should be considered. Equilibrium is achieved when the diffusional force balances the electric field force for all permeable ions.

Although out of scope of this thesis, a more detailed discussion of physical chemistry of the cell membrane can be found in standard textbooks such as Edsall and Wyman (1958) and Moore (1972).

2.2.1 Nernst Equation

If we consider one kind of ion, the *Nernst equation* gives the equilibrium voltage associated with a given concentration. The Nernst equation is derived from the electric field force and the diffusion force. For a more rigorous thermodynamic treatment see Katchalsky and Curran 1965 [32].

The current (ion flux) due to the electric field can be written as:

$$\bar{j}_{ke} = -u_k \frac{z_k}{|z_k|} c_k \nabla \Phi \quad 2.2.1.1$$

\bar{j}_{ke} = ionic flux (due to electric field) [mol/(cm²·s)]

where

u_k = ionic mobility [cm²/(V·s)]

z_k = valence of the ion

c_k = ionic concentration [mol/cm³]

The current (ion flux) due to diffusion force can be written as:

$$\bar{j}_{kD} = -D_k \nabla c_k \quad 2.2.1.2$$

\bar{j}_{kD} = ionic flux (due to diffusion) [mol/(cm²·s)]

where

D_k = Fick's constant (diffusion constant) [cm²/s]

c_k = ion concentration [mol/cm³]

The Diffusion constant and the ion mobility is closely related: in each case the ion flux is limited by the same factors of collision with solvent molecules. The relation between the mobility and diffusion constant was first derived by Nernst (1889):

$$D_k = \frac{u_k R T}{|z_k| F} \quad 2.2.1.3$$

where $T = \text{absolute temperature [K]}$
 $R = \text{gas constant [8.314 J/(mol}\cdot\text{K)]}$

At equilibrium the two current will balance out and the total current for the kth ion species is zero:

$$\bar{J}_k = 0 = -D_k z_k F \left(\nabla c_k + \frac{c_k z_k F}{R T} \nabla \Phi \right) \quad 2.2.1.4$$

Separating out the potential gradient and integrate over the membrane thickness we obtain:

$$\int_i^o \frac{dc_k}{c_k} = -\frac{z_k F}{R T} \int_i^o d\Phi \quad 2.2.1.5$$

where i stands for intracellular space and o stands for extracellular space. Carrying out the integration in 2.2.1.5 we have:

$$\ln \frac{c_{o,k}}{c_{i,k}} = -\frac{z_k F}{R T} (\Phi_o - \Phi_i) \quad 2.2.1.6$$

where $c_{i,k}$ and $c_{o,k}$ are the intracellular and extracellular concentrations of the kth ion respectively. The voltage across the membrane is defined as $\Phi_o - \Phi_i$, rearranging 2.2.1.6 with this notion we have:

$$V_k = -\frac{R T}{z_k F} \ln \frac{c_{i,k}}{c_{o,k}} \quad 2.2.1.7$$

where

- V_k = equilibrium voltage for the k^{th} ion across the membrane $\Phi_i - \Phi_o$ i.e., the Nernst voltage [V]
- R = gas constant [8.314 J/(mol·K)]
- T = absolute temperature [K]
- z_k = valence of the k^{th} ion
- F = Faraday's constant [9.649×10^4 C/mol]
- $c_{i,k}$ = intracellular concentration of the k^{th} ion
- $c_{o,k}$ = extracellular concentration of the k^{th} ion

We now have arrived the Nernst equation. If we take the human body's normal temperature 37 °C (310 °K), and +1 for the ion charge, and write 2.2.1.7 in base ten logarithm form. We obtain a simply form for human cell membrane voltage:

$$V = -61 \cdot \log_{10} \frac{c_i}{c_o} [mV] \quad 2.2.1.8$$

So for all living cells at equilibrium, we can estimate their voltage between the cell membrane expressed as in 2.2.1.8. This voltage is called the resting voltage or resting potential.

Similarly if we consider all three major ions involved a resting voltage can be derived in the following form David Goldman (1943) [33] and Hodgkin and Katz (1949) [34]:

$$V_m = -\frac{RT}{F} \ln \frac{P_K c_{i,K} + P_{Na} c_{i,Na} + P_{Cl} c_{o,Cl}}{P_K c_{o,K} + P_{Na} c_{o,Na} + P_{Cl} c_{i,Cl}} \quad 2.2.1.9$$

Substituting with human body's normal temperature and +1 for charge for Na^+ , K^+ and -1 for Cl^- , we have:

$$V_m = -61.1 \log_{10} \frac{P_{\text{K}} c_{i,\text{K}} + P_{\text{Na}} c_{i,\text{Na}} + P_{\text{Cl}} c_{o,\text{Cl}}}{P_{\text{K}} c_{o,\text{K}} + P_{\text{Na}} c_{o,\text{Na}} + P_{\text{Cl}} c_{i,\text{Cl}}} \text{ [mV]} \quad 2.2.1.10$$

The resting voltage of a neuron cell is about -70mV, and about -95mV for a skeletal muscle cell. The resting voltage is important because a change in the resting voltage over a threshold will activate an excitable cell. Stimulation based applications inject high level currents so that the desirable cells (neuron cells, muscle cells etc.) are activated. For the applications of EIS and EIT we will be injecting <10mA alternating current which introduces very low potential gradient across the membranes, equilibrium state is assumed. As we will discuss in the following section, in the frequency we apply (1Hz – 250KHz) the cell's capacitive behavior is from the change of distribution of ions at the membrane on the inner-cellular and the intracellular side.

2.3 Tissue as a Volume Conductor

In modeling the electric behavior of many cells (a tissue), while understanding the discrete cell structure is important, macroscopic estimates are also necessary to adequately describe the phenomena of interest. It is possible to replace the discrete structure with an averaged continuum. The goal of this section is to formulate a continuum model to express tissue's averaged electrical characteristics..

In most tissues we are interested in, it can be assumed that individual cells are roughly spheres with a diameter of around 10 μm . The cells are stacked together a lot like bricks and are held together by *tight junctions* (analogous to "spot welds"). In addition, there are *gap junctions acting as channels for inter-cellular* communication. The gap junction is a direct inter-cellular providing paths for ions and small molecules to travel between neighboring cells. Since such paths are limited in numbers and have very small cross-sectional areas, the effective junction resistance is rather large. In fact, the net junction resistance between two adjoining cells is thought to be in the same order of magnitude as the end-to-end resistance of the myoplasm (extra-cellular electrolyte) of either cell. It is worth mentioning though without the junction gaps among cells the effective resistance is several orders of magnitude higher for ions to go through the bi-layer fatty acid membrane.

When studying a tissue comprising many cells, the complex tissue may be replaced by intracellular and interstitial continua. The electrical conductivity and permittivity of the continua represent suitable average of the actual structure. The membrane separates both domain at each point. This model is known as *Bi-domain* Miller and Geselowitz, 1978; Tung in 1978 [35].

Based on the Bi-domain model, we can propose an equivalent circuit model for the cell and the extra-cellular electrolyte surrounding it (Fig. 2.3.1)

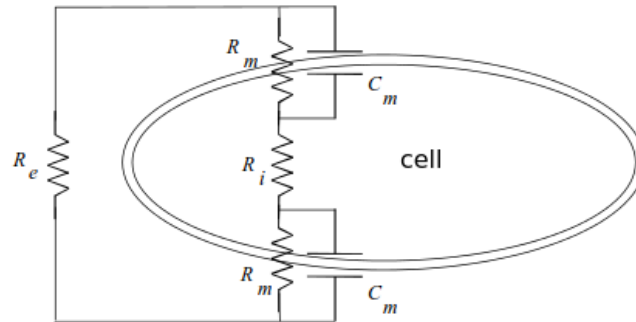


Fig. 2.3.1: Diagram of equivalent circuit of a cell model (overlaid with the cell structure). R_e is the extra-cellular resistance, R_i is the intra-cellular resistance, R_m is the membrane resistance and C_m is the membrane capacitance (image from Webster 1990).

With many cells in the tissue, we consider the tissue to have a effective point wise conductivity and permittivity distribution.

Frequency dependent of Tissue's Dielectric Behavior

As we can see from 2.1.1 the cell membrane presents a capacitive behavior. Moreover, the membrane's capacitance varies with frequency. Schwan [36] introduced three dispersion mechanisms (α , β , and γ) within the biological tissue. Under low frequency (1Hz to a few hundred Hz) is dominated by the α dispersion, which is associated with double layer at cell membranes. Between 1kHz to a few MHz is dominated by the β dispersion, which is associated with the polarization of the bi-layer fatty acid membrane molecules themselves, and other large polar molecules such as proteins. Above 10 GHz is dominated by the γ dispersion which is associated with the polarization of water

molecules. Fig. 2.3.1 shows a representative plot of the permittivity change vs. frequency.

The frequencies we applied in this thesis are under the α and β dispersion range.

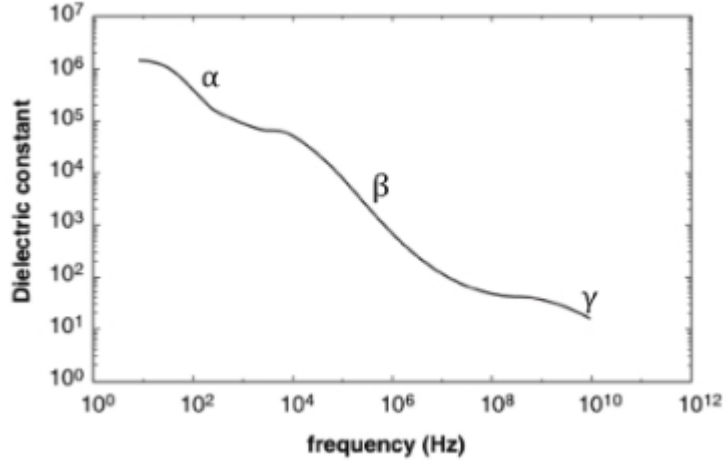


Fig. 2.3.2: Permittivity variation of a tissue as a function of frequency [37]

An electric model of such point-wise permittivity's frequency dependence can be written as below [38]:

$$\epsilon^*(\omega) = \epsilon_{\infty} + (\epsilon_s - \epsilon_{\infty}) / (1 + j\omega\tau) \quad 2.3.1$$

where ϵ_{∞} is the high frequency permittivity at which no polarizable element is able to respond, ϵ_s is the low frequency permittivity where all polarizable elements are fully polarized, ω is the angular frequency, and τ is the characteristic relaxation time of the tissue.

ELECTRICAL IMPEDANCE SPECTROSCOPY

The world we live in is filled with Electromagnetic (EM) waves or EM radiation. The amount of energy such waves carry follow Planck's Equation $E=h\nu$, where ν is the frequency of the wave and $h=6.626\times 10^{-34}$ is the Plank's constant (see Fig. 3.1). EM waves in different frequency bands display different characteristics based on the amount energy they carry. For instance, very high frequency EM waves are ionizing, as the frequency drops the waves become non-ionizing. An ionization wave is usually considered to have above 10eV in energy which includes the extremely high end of the spectrum to higher frequencies of ultra-violet light. The spectrum used in Electrical Impedance Spectroscopy (EIS) is considered within the radio frequency and very low frequency (VLF) bands and are non ionizing, namely 1Hz – 250KHz range. In EIS we study the interaction between alternating electric field and biological tissue in such frequency band.

The general approach in EIS is to apply a known electrical stimulus (current or voltage) to the material under study and then observe the resulting voltage or current response. Although technically the stimulus can take any form (pulse function, step function, sinusoidal etc.) we will limit our selves to applying sinusoidal stimulus. It is worth noting that if we impose a small perturbation the tissue can be seen as a linear volume conductor, in this case reciprocity theorem applies [39]. This means we can either inject current and measure voltage, or apply voltage and measure current, the impedance

obtained will be the same. This technique is actually being used in many commercialized EIS systems to insure the measurement data is within the linear region. The applied voltage or measured voltage due to current injection to stay in the linear region is usually considered to be $<10\text{mV}$.

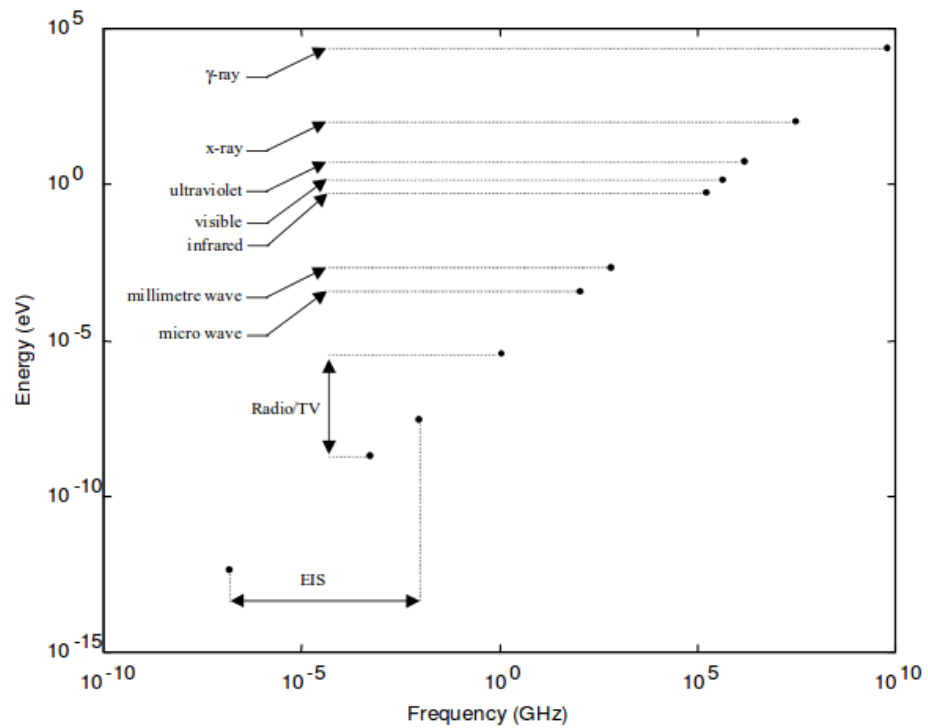


Fig. 3.1: Energy vs. frequency band for Electromagnetic waves.

3.1 Concept of AC impedance

EIS is based on perturbation of an equilibrium state. When a small alternating current (AC current) is applied in time domain in the form of a sinusoidal function, without

biological changes in the cell (surface and volume changes, phase transitions, electrolyte oxidation/reduction etc.) we can see the tissue as a passive linear volume conductor and Ohm's law applies. Then the voltage measured across tissue is also a sinusoidal function of the same frequency. If we express the current and voltage in tensor form we have:

$$I = |I| e^{j\omega t} \quad 3.1.1$$

$$V = |V| e^{j(\omega t - \theta)} \quad 3.1.2$$

Where ω is the radial frequency and θ is the phase delay. Then by definition, the impedance is the quotient of voltage and current:

$$Z = \frac{V}{I} = \frac{|V| e^{j\omega t}}{|I| e^{j(\omega t - \theta)}} \quad 3.1.3$$

or:

$$Z = \frac{|V|}{|I|} e^{j\theta} \quad 3.1.4$$

We call $|Z|$ the magnitude of the impedance and θ the phase. If we have a purely resistive load then 3.1.4 reduces to Ohm's law in DC form $R=V/I$, and phase is zero. However real tissues possess capacitive characteristic as well as resistive so the impedance is complex.

3.2 The sensitivity distribution

The sensitivity distribution is crucial to understanding how the transfer impedance is related to the tissue admittivity. For any non-regular geometries we Let's consider a tissue volume with a certain admittivity distribution γ , when we inject an AC current I through a drive electrode pair, and measure voltage V . We have the transfer impedance Z defined as:

$$Z = \frac{V}{I} \quad 3.2.1$$

Now if the conductivity distribution γ is perturbed with $\delta \gamma$, assuming linearity within the tissue volume, the impedance now becomes:

$$Z' = \frac{V + \Delta V}{I} \quad 3.2.2$$

or

$$Z + \Delta Z = \frac{V + \Delta V}{I} \quad 3.2.3$$

We can see that the change in transfer impedance is caused directly from change in voltage. We define the perturbation of voltage caused by the perturbation of admittivity to be the sensitivity distribution:

$$J = \frac{\partial V}{\partial \gamma}$$

3.2.4

In order to derive the sensitivity distribution, we consider the divergence theorem in an a closed volume region Ω , whose boundary $\partial \Omega$ is a piecewise smooth surface (Fig. 3.2.1), if we imagine to inject uniform current I into the drive pair and sense pair respectively, then the following relation holds as shown in 3.2.5.

$$\int_{\partial \Omega} \gamma(\phi_s \nabla \phi_d) ds = \int_{\Omega} \gamma(\nabla \phi_s \cdot \nabla \phi_d) dv$$

3.2.5

where ϕ_d and ϕ_s are the potential field of the drive and sense current respectively.

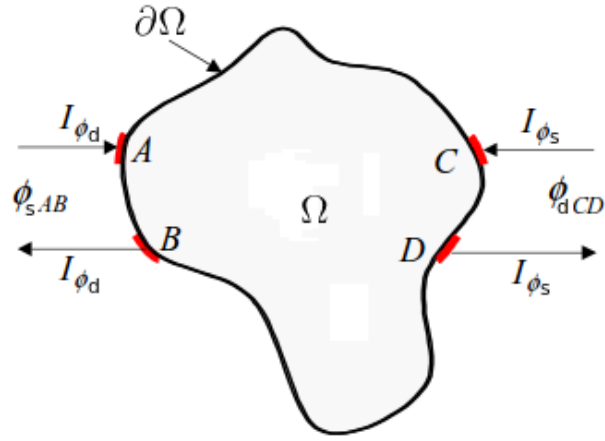


Fig 3.2.1: volume conductor with four electrode. A and B are the drive electrodes and C and D are the sense electrodes.

Taken the boundary condition into consideration, no current induced by the drive pair normal to the boundary occurs except at the driving electrodes A and B, hence the left-hand side of equation 3.2.5 becomes:

$$\int_{\partial\Omega} \gamma(\phi_s \nabla \phi_d) ds = I_{\phi_d}(\phi_{sA} - \phi_{sB}) = I_{\phi_d}(\phi_{sAB}) \quad 3.2.6$$

Similarly if we switch s and d in 3.2.5. and we obtain:

$$\int_{\partial\Omega} \gamma(\phi_d \nabla \phi_s) ds = I_{\phi_s}(\phi_{dC} - \phi_{dD}) = I_{\phi_s}(\phi_{dCD}) \quad 3.2.7$$

Combining 3.2.5-3.2.7 we obtain:

$$I_{\phi_d}(\phi_{sAB}) = I_{\phi_s}(\phi_{dCD}) \quad 3.2.8$$

Now if we I_{ϕ_d} and I_{ϕ_s} are equal and then the voltages observed on the other pair would be equal. We have arrived the reciprocity principle [40], namely if the same voltage will be measured if we switch the drive and sense pairs.

We can divide both sides by I^2 in 3.2.6 and rewrite the potential gradient in terms of Ohm's law:

$$j = \gamma \nabla \phi \quad 3.2.9$$

then we arrive at the formula for trans-impedance Z in an arbitrary volume conductor:

$$Z = \frac{1}{I^2} \int_{\Omega} \frac{1}{\gamma} (j_d \cdot j_s) dv \quad 3.2.10$$

If we inject unit current then Z simply becomes:

$$Z = \int_{\Omega} \frac{1}{\gamma} (j_d \cdot j_s) dv \quad 3.2.11$$

Above representation of the trans-impedance implies that with four point electrode EIS the measured impedance is the integration of the point-wise resistivity (1/admittivity) scaled by the dot product of the current densities of the drive pair and sense pair. The reciprocity theorem is also obvious here because switching the drive and sense electrode pairs will not change the trans-impedance.

If we combine the drive and sense electrodes, we arrive at the trans-impedance formulation of the 2 electrode scheme:

$$Z = \int_{\Omega} \frac{1}{\gamma} j^2 dv$$

3.2.12

With two electrode EIS, the current drive and sense current densities are identical and hence we have a strictly positive scaling factor shown in 3.2.12.

With small perturbation in the admittivity, we will have perturbation in measured voltage V .

$$\gamma \rightarrow \gamma + \delta\gamma$$

$$V \rightarrow V + \delta V$$

It is calculated that the perturbation in V follows the form [41]:

$$\delta V = \int_{\Omega} \delta\gamma (\nabla\phi_s \cdot \nabla\phi_d) dv$$

3.2.13

Hence the sensitivity field can be expressed as:

$$J = \frac{\partial V}{\partial \gamma} = \int_{\Omega} (\nabla\phi_s \cdot \nabla\phi_d) dv$$

3.2.14

Here we see, similar to the Trans-impedance, the sensitivity distribution is the integration of the dot product of the shape function of the gradient of the electric potential of the drive and sense pair. Depending on the position of the electrodes, unless two electrode measurement is carried out, the sensitivity distribution in certain areas can be zero or negative. This indeed creates complexity in attempting to correlate tissue properties to their trans-impedance. One of the most fundamental design principals is to design the positioning of the electrodes such that positive, and ideally uniform sensitivity distribution is achieved. Chapter 5 discusses this aspect in detail.

3.3 The electrode-electrolyte interface

When an electrode is in contact with tissue, the electrode is in fact in contact with intracellular electrolyte. In an ideal situation charges at this interface can flow through between the electrode and the electrolyte freely without any impedance. However reality

is far from the ideal case. At initial contact, due to mismatch of the Fermi-levels in the electrode and the electrolyte, current flow will occur. Along with other reasons (adsorbed atoms on the electrode surface for example), a “double layer” establishes at the interface upon equilibrium. This double layer differ in electrical, compositional and structural characteristics.

Considering the intracellular electrolyte is a low concentration aquatic solution, we consider the Gouy-Chapman-Stern model [42], as seen in Fig. 3.4.1 the inner layer consists the adsorbed polarized ions in Boltzmann distribution fixed on the surface of the electrode. Such adsorbed ions are not affected by the concentration of the solution but rather the available sites for adsorption. The outer layer consists of free ions attracted by the electric field created by the mismatched potential on the electrode surface and in the electrolyte solution. The concentration of this outer layer drops exponentially following the Boltzmann distribution for diffusion. We can think of this model as a crowd of people waiting at a fence attempting to go through. The first comers will be waiting right at the fence securing their position, while as more people come the available sites along the fence become all occupied, the late comers will move around to find a less crowded spot. The concentration of people drops further away from the fence, and the free moving people form a distribution of Boltzmann diffusion. The inner layer and outer layer are called the inner Helmholtz layer and outer Helmholtz layer respectively to honor the physicist Helmholtz who pioneered this field of study [43].

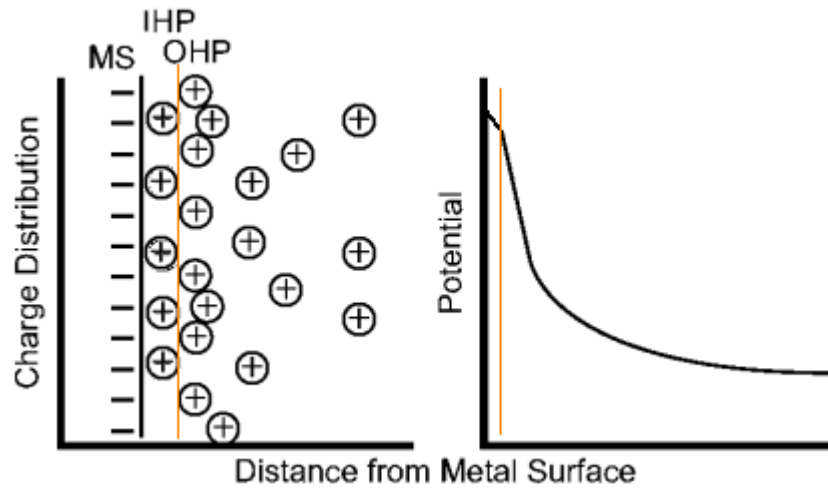


Fig. 3.4.1: Esin and Markov, Grahame, and Devanathan model. [44]

The equivalent circuit is two capacitors in series:

$$\frac{1}{C} = \frac{1}{C_1} + \frac{1}{C_2} \quad 3.4.1$$

where C is the total double layer capacitance of the double layer capacitor, C_1 is the capacitance of the inner Helmholtz layer which can be roughly modeled as a plate capacitor, and C_2 is the outer Helmholtz layer whose capacitance changes mainly with the concentration of the electrolyte solution. As the solution concentration increases the diffusion layer becomes small and hence C_2 becomes large, so the $1/C_2$ term drop out in very high concentrations in 3.4.1. On the other hand, in low concentrations

concentrations the outer Helmholtz diffusion layer can be large hence C_2 dominates the double layer capacitance. The latter is the case for intracellular electrolyte.

Equivalent circuit model of the double layer

In addition to the double layer capacitance, there is also DC resistance due related to ion movement etc. Equation 3.4.2 shows the simplified equivalent circuit model at the electrode-electrolyte interface [45].

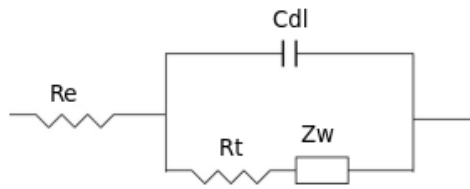


Fig. 3.4.2: Randle's circuit

C_{dl} is the double layer capacitor, the resistor in series R_e is the electrolyte resistance due to ion movement, R_t is the active charge transfer resistance associated with reduction/oxidation (redox) chemical reaction and W is an element of diffusion of such chemical reagents and is called Warburg element. In the case of small voltage and current perturbation we assume there is no redox reaction hence the parallel resistance is not existent. Fig. 3.4.3 shows the equivalent circuit in small perturbation case such as EIS.



Fig. 3.4.3: Electrode-electrolyte equivalent circuit with small perturbation

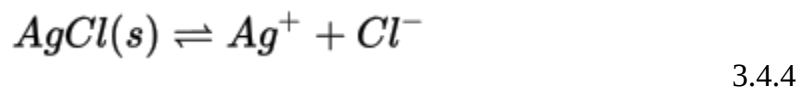
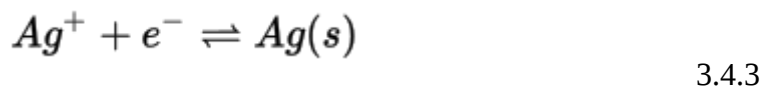
In addition, through experiments the double layer capacitor is more appropriate replaced with a constant phase element. It is an empirical model with a constant phase that is < 90 degrees.

$$Z_{CPE} = \frac{1}{C(j\omega)^n} \quad 3.4.2$$

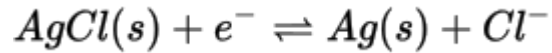
where Z_{CPE} is the constant phase element, n is between 0 and 1, and the phase is $90 \cdot n$. We can see that this non-ideal capacitor has resistant elements also with less than perfect phase. Such empirical correction is based on the observation of a depressed Nyquist plot, which will be talked about in the following section. Although the definitive explanation is still in debate it is in general agreement that the phase depression is due to some kind of dispersion at the electrode surface.

Ag/AgCl electrode

So far we have focused on polarizing electrodes such as most metals, another electrode that is largely used for non-invasive Bio-electricity applications is made of Ag/AgCl (for example electrodes used for ECG recording). Ag/AgCl are also used as the reference electrode for 3 electrode setup and as the reference electrode in pH meters. In contrary to the metal electrodes, these electrodes function as a redox electrode with no double layer charge accumulation. The reaction is between the silver metal and silver chloride salt.



With an overall reaction of:



3.4.5

The fact that Ag/AgCl electrode is a redox electrode makes it important to look at the reaction kinetics and obtain its frequency response over the EIS band. In the figure below shows a magnitude Bode plot of an Ag/AgCl in 0.01M HCL.

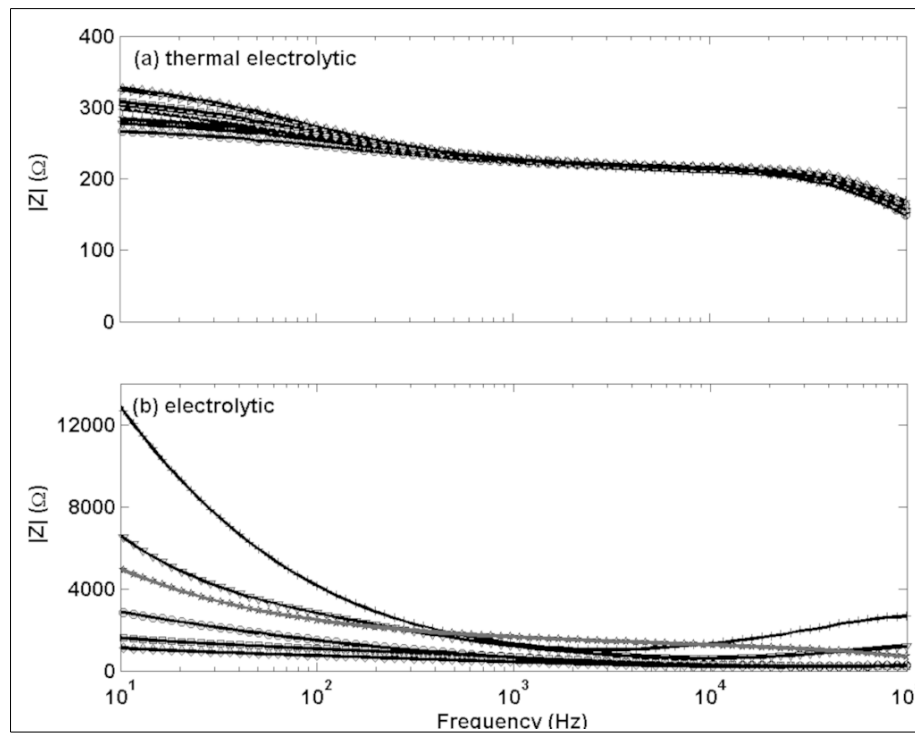


Fig. 3.5.3: Effect of Structural Design of Silver/Silver Chloride Electrodes on Stability and Response Time and the Implications for Improved Accuracy in pH Measurement [46]

3.4 Bode plot and Nyquist plot

Bode plots are the most widely used method of displaying frequency response information of a system. Bode plot is on a log-log scale or semi-log scale, and it is

capable of displaying a wide range of system response vs. a wide range of frequencies. Bode plot is used to assess stability of poles and zeros of a system. In EIS the impedance magnitude is usually shown as a log-log bode plot while the phase is shown on a semi-log scale plot.

Nyquist plots are parametric plots of a system response. It is often used in a feedback system to assess stability. Here in EIS, The x axis of a Nyquist plot is the real component of the impedance and the y axis the imaginary. Each point on the plot is a complex impedance measured at a certain frequency.

In the following we show the Bode plot and Nyquist plot of the Bode plot and Nyquist plot for an ideal Randle's circuit. It should be pointed out that the double layer capacitor is not an ideal capacitor in practice (hence the CPE model), and the capacitance changes with frequency, however it is still of value to simulate the ideal model so that we can familiar ourselves with what to come with practical cases.

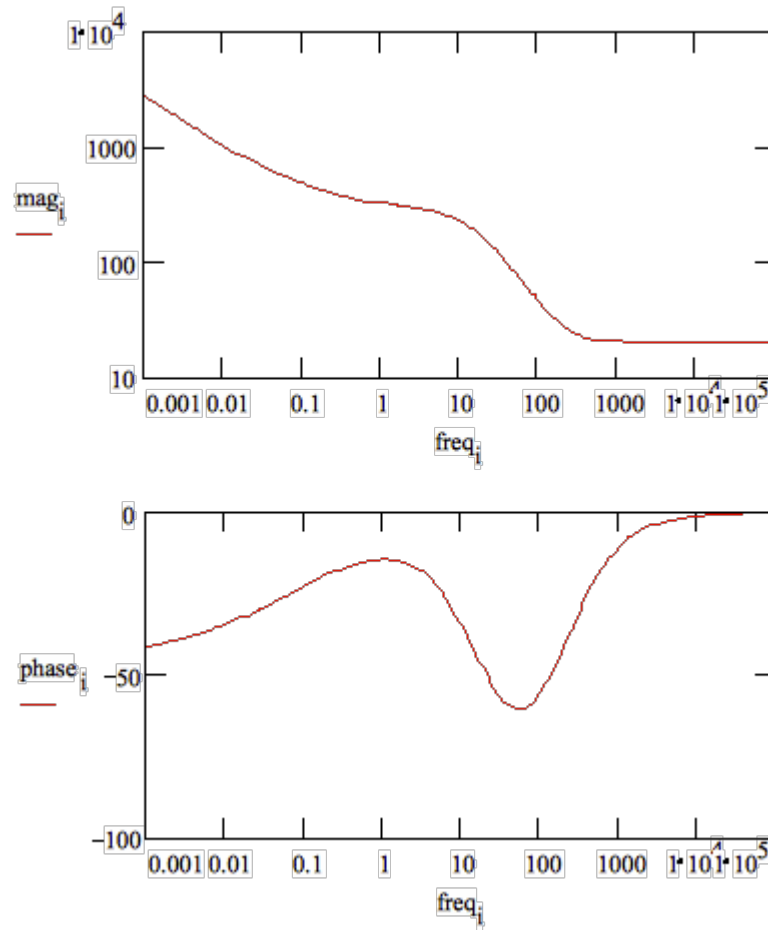


Fig. 3.5.1.: Simulated amplitude Bode plot (up) and phase Bode plot (down) based on Randle's circuit in Fig. 3.4.2

In the above simulations, the parameters assumed are $R_e = 20 \Omega$, $R_t = 250 \Omega$ and $C_{dl} = 40 \mu\text{F}$. As we can see in the Bode plot, for the particular double layer capacitor of $40 \mu\text{F}$, there is a pole at around 10Hz and a zero at around 500Hz. Eventually the impedance from the capacitor drops out and the circuit is dominated by the resistor and magnitude becomes flat, phase becomes zero in the Bode plots. This corner shifts to higher frequency as the electrode area decreases and the capacitance decreases proportionally.

The capacitance per unit area is dependent on the kind of metal and the electrolyte. A rule of thumb for gold electrode is $60 \mu\text{F}/\text{cm}^2$.

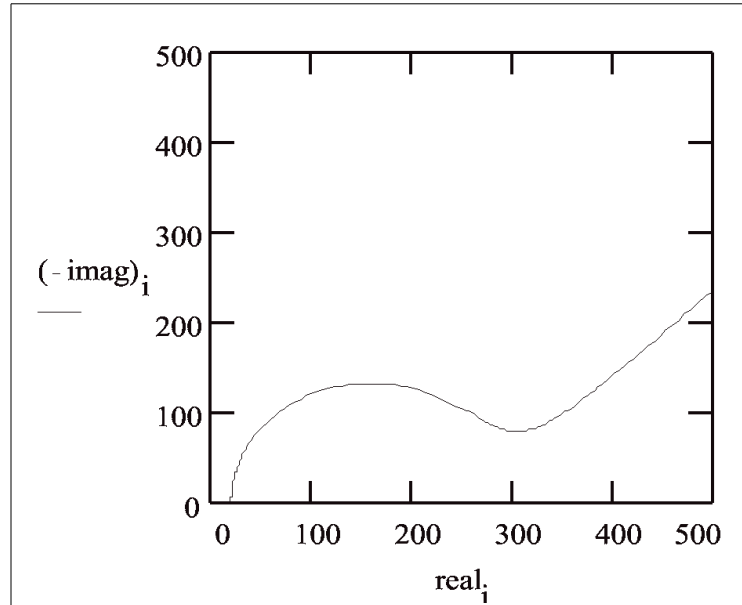


Fig. 3.5.2: Simulated Nyquist plot of a of an ideal Randle's circuit based on Randle's circuit in Fig. 3.4.2.

In the Nyquist plot we can see a semi-circle connected to a line of 45 degree angle (equal dynamic phase delay). The 45 degree line occurs in the low frequency region and is associated with the Warburg element. As the frequency increases the double layer capacitor's impedance becomes dominant and we show a typical semicircle of RC circuit. At extremely high frequencies we arrive at the left end of the semicircle, at this time only the series resistance R_e is effect. Without the active reaction parallel circuit the Nyquist plot will be only a semicircle with no line. The constant phase characteristic is due to the fact that experiments show that the semicircle is usually rotated with some angle

clockwise [47], hence instead of having a 90 degree angle. The CPE's phase delay is less than 90 degrees.

3.5 Lumped circuit model

If we approximate the tissue to be isotropic and uniform and has a regular shape of Fig. 3.5.1, with metal plate electrodes on each end (see Fig. 3.5.1).

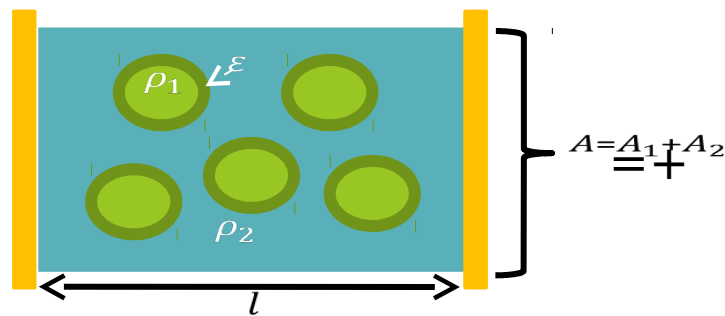


Fig. 3.5.1: tissue and electrode model for EIS measurement

The equivalent of such model with lumped circuit elements can be shown in Fig. 3.5.2.

Using a simplistic model, the cross section A is comprised two materials: the cells taking up A_1 , and the extracellular electrolyte taking up A_2 , where $A_1 + A_2 = A$. The cell can be modeled as a capacitor (double layer at the cell membrane) and resistor (inner-cellular electrolyte), lump up the cells we get R_1 and C to model the cells (see Fig. 3.5.2). The extracellular electrolyte can be modeled with resistor R_2 (Fig. 3.5.2). Now we can derive the equivalent circuit model for tissue to be the following.

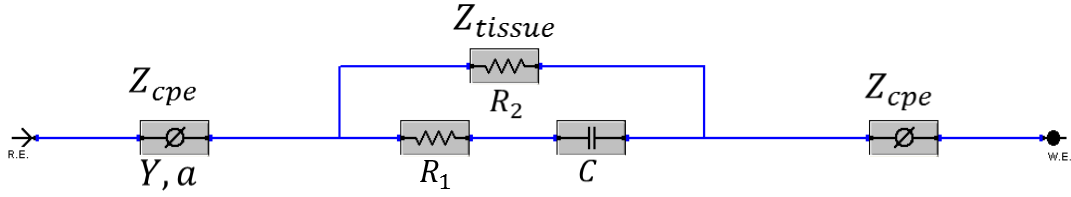


Fig. 3.5.2: equivalent circuit of tissue and electrode model

$$Z_{tissue} = \frac{\left(\frac{1}{j\omega C} + R_1\right) \cdot R_2}{\left(\frac{1}{j\omega C} + R_1\right) + R_2} = \frac{(1 + j\omega R_1) \cdot R_2}{1 + j\omega(R_1 + R_2)} \quad 3.5.1$$

Where

$$R_1 = \rho_1 \cdot \frac{l}{A_1} \quad 3.5.2$$

$$R_2 = \rho_2 \cdot \frac{l}{A_2} \quad 3.5.3$$

$$C = \varepsilon \cdot \frac{A_1}{D_{cell}} \quad 3.5.4$$

With the constant phase element model for the electrode-electrolyte interface in 3.3.2 in series, we have the Bode plot of the equivalent circuit. We can see three corners which are determined by the double layer impedance and the tissue impedance. The calculation of the corner frequencies are shown in Fig. 3.5.3. The second corner and third corner are closely related to both the tissue's inner and intra cellular properties (for example the

content of the cell, the cell geometry, and the packing density etc.), hence the tissue's impedance properties can be correlated to corner frequencies along with the levels of the flat band between first and second corner. In Chapter 4 we will see the biological tissues follow roughly the shape. The exact corner frequencies are determined by the electrode effective surface area and the tissue itself.

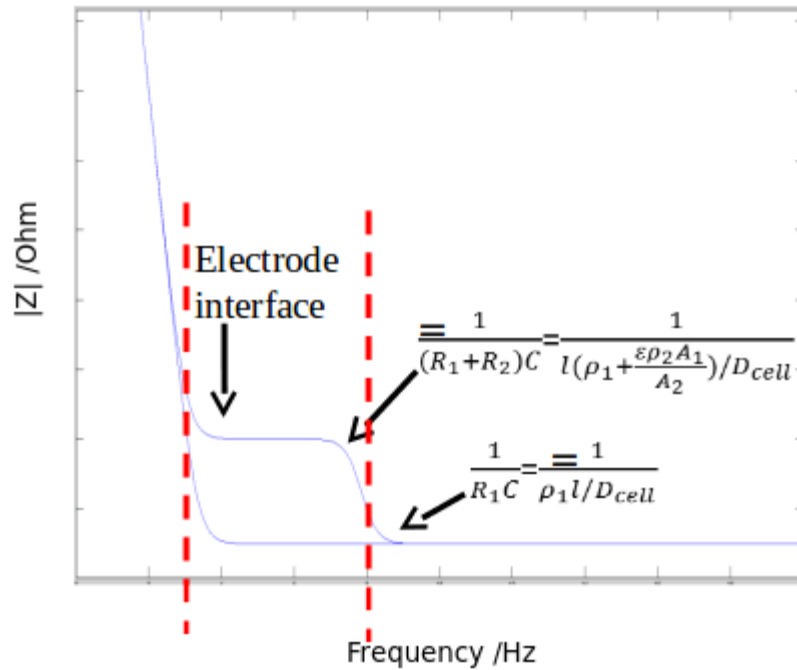


Fig. 3.5.3: Impedance Bode-plot on log-log scale showing three corners.

ELECTRICAL IMPEDANCE TOMOGRAPHY

In electrical impedance tomography (EIT) voltage data measured at the boundary of a conductive domain are used to reconstruct the spatial distribution of its electrical conductivity (admittivity). The technique has been widely applied in geophysics such as oil exploration, and nondestructive testing of materials [48-52]. EIT has been recently applied in the bio-imaging field such as bed-side lung ventilation monitoring [53,54]. In this chapter we explore the possibility to apply EIT in novel applications of vulnerable plaque imaging and fatty liver early detection, both of which are closely related diseases and can become fatal if not detected in time and yet treatable if detected early.

4.1 The instrumental setup

For the experiments, we employ two hardware systems: Swisstom (Switzerland) and NI Labview (National Instruments, USA) system made in house. Both have 32 electrodes with the capability of doing injection pattern from neighboring scheme to skipping arbitrary number of electrodes. The reason to develop the Labview system is that Swisstom has a limited voltage range (4.5Vp-p). For measurements with high impedance tissues such as fat with small electrodes we need a bigger voltage swing range to keep the SNR acceptable. In addition, with human body measurements often times difference imaging at different frequencies are needed. Swisstom system has a limited frequency range of 50khz to 150khz. With NI DAQ card and an AC current generator we can inject

currents of 1kHz – 100kHz range. The upper limit was determined by the current source Keithley 6221 to be 100kHz, the maximum sampling rate of the NI DAQ is 1M samples/sec so it can achieve theoretically 500K samples/sec, or practically 200K samples/sec (Nyquist rate of $\frac{1}{2}$ sample frequency is hard to achieve in practice, it is good to leave some margin). Although it is recognized that recent years have seen developments and commercialization of several new multi-frequency EIT systems that are capable of scanning a wide range of frequencies [55-57].

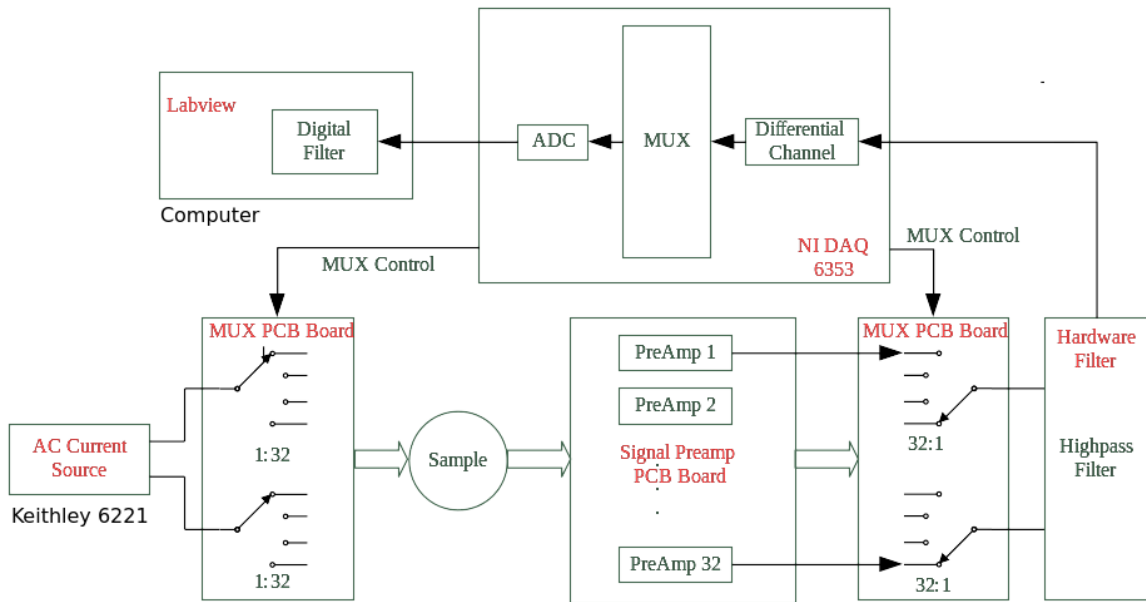


Fig 4.1.1: System diagram of the Labview Based system.

The Labview based system diagram is shown in Figure 4.1.1. The Labview program controls the multiplexer for current pair and voltage pair through the NI DAQ card. The

actually current injection is by AC current source Keithley 6221 (Keithley, USA). For the voltage measurement, each channel goes through a pre-amplifier stage prior going through the multiplexer board, the selected signal then goes into the hardware filter. The filtered signal then feeds into the DAQ differential analog channel to be read by the Labview program. An additional bandpass digital filtering is performed for the voltage reading in Labview.

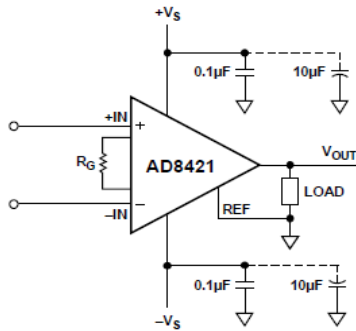
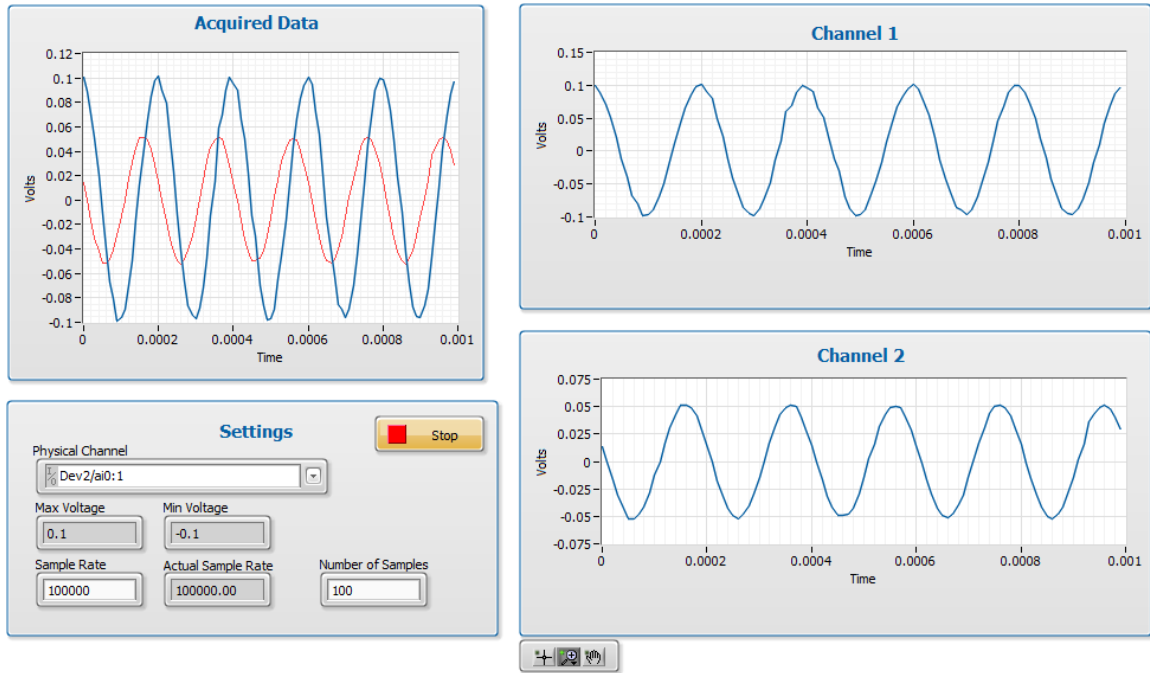


Fig 4.1.2: Pre-amp circuit diagram. $R_G=200\Omega$ (0.1%, 15 ppm/ $^{\circ}\text{C}$) Gain = $1+9.9\text{k}\Omega/R_G=50.5\text{x}$

The pre-amp before each multiplexer channel for voltage measurement is shown in Fig 4.1.2. The time domain waveform is shown in Fig 4.1.3.

Fig 4.1.3: Time domain waveforms. Upper left: Signal out of pre-amp (blue), signal out



of hardware filter (red). Lower left: DAQ settings, sampling rate is 100Khz. Voltage range is +/-0.1V. Upper right: signal after pre-amp, before hardware filter. Lower right: signal out of hardware filter. Noise performance of Swisstom and Labview System.

Noise performance is critically important for the reconstruction quality. Higher noise means we need to use bigger regularization parameter which compromises the fitting of the data that resembles the conductivity distribution.

We define the noise in each voltage channel (totaling $32 \times 32 = 1024$ channels) to be the quotient of the the average of the signal over 10 frames of data to the standard deviation of such data.

$$\text{SNR}_i = \frac{[\bar{\mathbf{v}}]_i}{\text{SD}[\mathbf{v}]_i}$$

Where $i= 1,2,\dots,1024$. And SNR in db form is $20 \log_{10}(\text{SNR})$.

The following Figures show the noise comparison of Swisstom system in noise performance.

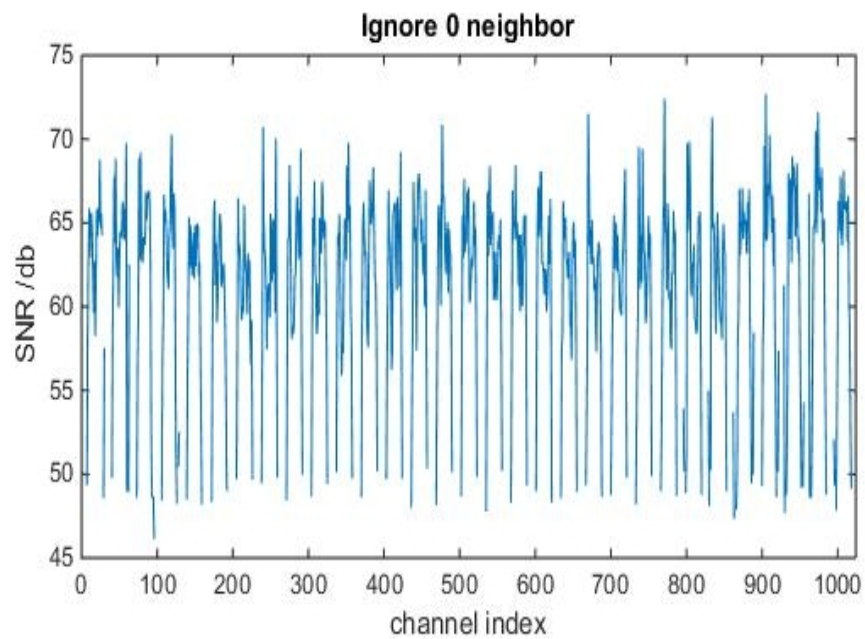


Fig 4.1.4: Swisstom noise performance over 10 consecutive frames.

4.2 The mathematical framework

EIT has seen numerous theoretical and computational developments since the beginning of its time in the 1980s [58-62]. However, two fundamental challenges remain that limit EIT's accuracy and resolution, namely the nonlinearity of the forward problem and ill-posedness of the inverse problem. From the mathematical perspective, this inverse boundary value problem, formalized by the Caldéron's first paper on EIT of [58], presents a number of implications on the existence, uniqueness, and numerical stability of the solution [62]. Although the issues of existence and uniqueness can be eradicated with reasonable assumptions about the conducting body, instability causes the solution to be extremely sensitive to noise in the voltage data. Such instability is caused by the severely lack of full boundary voltage data. To alleviate the ill-posedness one usually resorts to implementing some type of regularization strategy to stabilize the solution based on a priori knowledge about the conducting body (differentiability, smoothness etc.)

The inverse problem is usually solved as an optimization problem with constrained (regularized) Gauss-Newton (GN) type solver. In order to calculate the residual error in the above inverse problem, a forward problem also needs to be solved. In the sub sections below we layout the mathematical framework of the EIT problem.

4.2.1 The inverse problem

We consider the problem given conductivity σ , the boundary voltages can be expressed as 4.2.1.1, where ε is the noise in the measurement instrument, and $f(\sigma)$ is considered the

“forward problem” obeying the governing Maxwell equations (more details in 4.2.2).

4.2.1.1

To take a Gauss-Newton approach, the solution of σ would be which that minimizes the

L-2 norm of the error:

$$\phi = \|\varepsilon\|^2 = \|V - f(\sigma)\|^2 \quad 4.2.1.2$$

Hence the objective function to be minimized is:

$$\sigma = \underset{\sigma}{\operatorname{argmin}} \left\{ \|\varepsilon\|^2 \right\} \quad 4.2.1.3$$

If we take the first order of Taylor series expansion of the forward problem function can

be approximated as:

$$f(\sigma) \simeq f(\sigma_o) + J(\sigma - \sigma_o) \quad 4.2.1.4$$

Then the objective function becomes:

$$\phi = \|(V - f(\sigma_o)) - J(\sigma - \sigma_o)\|^2 \quad 4.2.1.5$$

To minimize Φ , we set $\frac{\partial \phi}{\partial \sigma} = 0$ and solve for σ , from 4.2.1.5 we have:

$$\sigma = \sigma_o + (J^T J)^{-1} J^T (V - f(\sigma_o)) \quad 4.2.1.6$$

Solution in 3.2.1.6 shows the scheme of the so called “absolute imaging”, where only one voltage data set is measured and subtract by the calculated voltage data set.

Since the nature of the forward function is not linear, solving 3.2.1.6 iteratively are needed in order to converge σ to a meaningful solution. However, since error from the forward calculation (mainly due to geometry mismatch especially around the electrodes) is added to the measurement noise thus influences the direction of the solution in each step, convergence to is not guaranteed [63-65]. However the GN algorithm converges well if the forward problem is very close to linear, which is true when only when the σ perturbation is small. Then the forward problem can be written as :

$$f(\sigma) = J\sigma \tag{4.2.1.7}$$

And the solution becomes:

$$\sigma = (J^T J)^{-1} J^T V \tag{4.2.1.8}$$

This has inspired the so called “difference imaging”, which measures two data sets before and after a small σ change. Hence the forward problem can be approximated as linear and the difference in σ is computed:

$$\Delta\sigma = (J^T J)^{-1} J^T \Delta V \tag{4.2.1.9}$$

In the difference imaging scheme, the calculated voltage set is not present and does not influence the solution direction. In fact with small σ perturbations the one-step solution is usually satisfactory.

Regularization

Above we have arrived at the unconstrained GN solver. However in practical situations the unconstrained GN form cannot be used due to the following 2 reasons: First, since J is far from full rank $J^T J$ is not full rank, hence inverse of $J^T J$ does not exist. Second, due to the ill-posed nature of the inverse problem, the solution σ is heavily sensitive to the perturbation in measurement voltage V , which means a small noise in V can result in a big change in the solution σ . The treatment for such condition is to introduce a constraint so that the solution will favor those that we prefer.

$$\phi = \|\epsilon\|^2 + \lambda \|\sigma\|^2$$

4.2.1.10

Here we add a constraint term to the objective function. The term in 3.2.1.10 is the L-2 norm of the solution σ . This means we will punish the large conductivity spikes in the solution space. The coefficient lambda is the regularization parameter, we will be setting this parameter such that we balance the trade off between fitting the error and constraining the solution from undesired properties.

A more general form of constraint term we will use is as below:

$$\phi = \|\varepsilon\|^2 + \lambda \|\Gamma\sigma\|^2 \quad 4.2.1.11$$

The above form is known as the Tikhonov Regularization. The term Γ is introduced to enable us to select more properties of the σ . For example if we know the solution is smooth Γ can be a Laplacian operator to punish the non smoothness in solutions. Or if we know in a priori that certain area of the conductivity is the same or similar Γ can be a “weighted” Laplacian operator that punishes non-smoothness heavily in these regions. This is applicable in medical imaging where EIT is to obtain the conductivity information of certain organs, and information of location of the organs may be obtained a priori with other imaging modality (CT, ultrasound, etc.). In this scenario the conductivity of the organs of interest may be determined more accurately with such a priori information (details in following experimental section).

The solution to 3.2.1.11 after setting the gradient to zero is the following:

$$\sigma = \sigma_o + (J^T J + \lambda \Gamma^T \Gamma)^{-1} J^T (V - f(\sigma_o)) \quad 4.2.1.12$$

Similarly the difference imaging solution under the linearized forward problem becomes:

$$\Delta\sigma = (J^T J + \lambda \Gamma^T \Gamma)^{-1} J^T \Delta V \quad 4.2.1.13$$

4.2.2 The forward problem

The forward problem is that given conductivity distribution of a domain, under certain current excitation pattern we find the voltage distribution on the boundary of the domain.

To write out the forward problem function explicitly 3.2.1.1 can be expressed as:

$$V = f(\sigma, I) \quad 4.2.2.1$$

Where I is the current injection pattern. According to linearity of Maxwells equations we can write this function as matrix form :

$$V = \Upsilon I \quad 4.2.2.2$$

Where Upsilon is the the linear operator that is determined by σ . It is the Dirichlet to Neumann operator associated to conductivity σ . You may encounter Upsilon in other names such as the system matrix, the stiff matrix, etc. As we have seen in section 3.2.1 each GN inverse step involves solving for this forward problem and/or the Jacobian derived from this forward problem. In the following section will show the formulation of such Upsilon operator and the method to solve it numerically.

Governing equations

In order to formulate Γ we first introduce the governing equations for this problem. We assume the biological domain is source free. Then within the domain the Laplace equation holds:

$$\nabla \cdot (-\sigma \nabla u) = 0$$

4.2.2.3

Of course in a human body we will have heart ECG and muscle EMG inevitably occurring. These electrical signals are modeled as electrical dipoles propagating at the signal front. The electrical dipole is formed due to the reverse polarity of the cell membrane in the activated cell. It is apparent that the dipole distance is on a cellular level (distance between two cells) and is far less than the distance we observe from. Hence we can use the dipole's far field formulation as the potential field solution. One can verify that a dipole's far field solution approaches the Laplace equation 4.2.2.3.

In addition to satisfying the Laplace equation, at the boundary we should satisfy:

$$\sigma \nabla u \cdot \hat{n} = 0 \quad \partial\Omega \setminus \Gamma_{el} \quad 4.2.2.4$$

$$\int_{el} \sigma \nabla u \cdot \hat{n} ds = I_l \quad \Gamma_{el} \quad 4.2.2.5$$

$$u + z_l \sigma \nabla u \cdot \hat{n} = V_l \quad \Gamma_{el} \quad 4.2.2.6$$

Where Γ_{el} is the boundary where electrodes are present. The boundary conditions simply means that the current flux at the boundary is zero where there is no electrode and total current under a certain electrode should sum up to be I_l , the current on the l th electrode based on the current injection pattern I , where $l = 1, 2, \dots, L$. The third boundary condition in 3.2.2.6 is to specify that the potential on the l th electrode V_l , is the potential u on the boundary plus the potential difference due to existence of contact impedance. Above 3 boundary conditions form the so called “complete electrode model”. One point that is worth noticing is that, however, in the complete electrode model we assume the conductivity σ , or $1/\sigma$ as z_1 , is the same within all points of the boundary under an electrode. This may not be the case under practical situations in tank experiments as an electrode surface may not be in the same condition everywhere. This can lead to additional errors in forward calculation as 3.2.2.6 is not accurate anymore. However it is assume Ag/AgCl ECG type electrodes have uniform conductivity and the skin underneath is in similar condition and thus has uniform conductivity.

It has been proven that with vanishing currents on the boundary surface and a defined ground 4.2.2.3 – 4.2.2.6 has unique solution [66]. Hence we have simply:

$$\sum_{l=1}^L I_l = 0 \quad 4.2.2.7$$

$$\int_{\partial\Omega} u ds = 0 \quad 4.2.2.8$$

To satisfy 4.2.2.7 we will balanced charges injected and for we define the ground to be the sum of boundary potentials in 4.2.2.8.

Numerical method

In order to solve for Γ numerically with FEM techniques we express the governing function in its weak form, by taking the inner product of the Laplace equation with a test function φ :

$$\int_{\Omega} v \nabla \cdot \sigma \nabla u dv = 0 \quad 4.2.2.9$$

Although the detailed reason is out of scope of this thesis, the rationale to solve the weak form instead of the strong form of the PDE is that by introducing the weak form we are able to relax the smoothness requirement of the solution . This is done with integration by parts. With integration by parts from equation 4.2.2.9 and assume $u = 0$ at $\partial \Omega$ we arrive at the following equivalent form:

$$\int_{\Omega} \sigma \nabla v \cdot \nabla u dv = 0 \quad 4.2.2.10$$

We can see that after integration by parts the solution u is no longer required to be twice differentiable, but rather once differentiable, hence the solution space is relaxed.

The FEM numerical method needs a basis function in which we will for solution u . We will use a piecewise linear basis function:

$$\phi_i = \begin{cases} 1 & \text{on vertex } i \\ 0 & \text{elsewhere} \end{cases} \quad 4.2.2.11$$

Then the solution u can be expressed as a linear combination of the basis function weight coefficient U_i , where $i = 1, 2, \dots, n$:

$$u = \sum_{i=1}^n U_i \phi_i \quad 4.2.2.12$$

Now we write the weak form 4.2.2.10 in the terms of the basis function 4.2.2.12, and apply green's theorem, the left-hand side becomes:

$$\sum_{i=1}^n U_i \int_{\Omega} \sigma \nabla \phi_j \cdot \nabla \phi_i \, dv = \int_{\partial\Omega} \phi_j \sigma \nabla u \cdot ds = - \int_{\partial\Omega} \phi_j j \cdot ds$$

4.2.2.13

Where j is one particular node, and 4.2.2.13 applies to all nodes individually in the domain and at the boundary. Apply boundary conditions 4.2.2.4 – 4.2.2.6 to all j we arrive at the matrix form of 4.2.2.13.

$$\begin{bmatrix} A_M + A_Z & A_V \\ A_V^T & A_D \end{bmatrix} \begin{bmatrix} U \\ V \end{bmatrix} = \begin{bmatrix} 0 \\ I \end{bmatrix} \quad 4.2.2.14$$

$$A_M = \int_{\Omega} \sigma \nabla \phi_j \cdot \nabla \phi_i \, dv \quad 4.2.2.15$$

$$A_V = \int_{\partial\Omega} -\frac{1}{z_l} \phi_i \, ds \quad 4.2.2.16$$

$$A_D = \begin{cases} (\frac{1}{z_i})_i |E_l| & i = j = 1, 2, \dots, L \\ 0 & elsewhere \end{cases} \quad 4.2.2.17$$

$$A_Z = \int_{\partial\Omega} \frac{1}{z_i} \phi_i \phi_j ds \quad 4.2.2.18$$

U contains the coefficients to all the nodal potential basis, and V is a subset of U and contain coefficients of the electrode facing nodes. The top sub matrix is the discretized version of the Laplace equation's weak form in 4.2.2.10 and the bottom sub matrix is the boundary condition on the current injection pattern.

The forward solution U and V can be calculated with Penrose-Moore pseudo inverse.

This can be done easily with the Matlab left divide “\” command.

$$\begin{bmatrix} U \\ V \end{bmatrix} = \begin{bmatrix} A_M + A_Z & A_V \\ A_V^T & A_D \end{bmatrix}^+ \begin{bmatrix} 0 \\ I \end{bmatrix}$$

4.2.2.19

4.3 EIDORS library

EIDORS is an open source software suite for image reconstruction in electrical impedance tomography and Diffuse optical tomography. It is a collective effort written by

researchers over the years and it is under active maintenance to date. Most of the published state of the art EIT algorithms can be found in the EIDORS library.

EIDORS is available in Matlab and Octave. The most used version is the Matlab version.

More details about the EIDORS code and tutorials can be found by following the link

<http://eidors3d.sourceforge.net> [67].

EIS FOR ENDOLUMINAL PLAQUE DETECTION

It is of great clinical interest to have easy and reliable diagnostic techniques to localize and identify vulnerable plaques. Here, an *in-vivo*, catheter-integrated and balloon-mounted Parylene-C micro electrode impedance sensor was developed for intra-vascular interrogation of atherosclerotic vulnerable plaques using Electrical Impedance spectroscopy (EIS). Successful *in vivo* experiments of the EIS device were demonstrated using high-fat-dieted New Zealand rabbits. The results showed that electrical impedance spectroscopy (EIS) with micro parylene electrodes is promising to distinguish unstable plaques.

Studies have shown emerging evidence that rupture of coronary plaque containing a lipid-rich core with subsequent thrombus formation is the most frequent mechanism by which atherosclerosis leads to the acute ischaemic syndromes of unstable angina, acute myocardial infarction, and often times, sudden cardiac death. However, since the lumen is not significantly blocked in these cases, such “vulnerable” plaques show noncritical stenosis in X-ray angiography and Intravascular Ultrasound (IVUS), tools currently available to diagnose coronary artery disease. The ability to distinguish such rupture-prone vulnerable plaques remains largely lacking. Therefore it is of great clinical interest to find improved diagnostic techniques to identify and localize such rupture-prone plaques. On the other hand, lipid has significantly lower electrical impedance than the

rest of the vessel components in certain frequency bands [68]. We show in this paper that electrical impedance spectroscopy (EIS) technique can be useful to effectively distinguish plaques with such lipid cores. We include in this paper the design rationale of a four electrode EIS sensor and the measurement results between 1 Hz to 300 KHz of ex-vivo mouse aortas with plaque lesions. The impedance modulus over 200 Hz-100 KHz show consistent elevated values 2-5 times higher than their proximity control sites in all three individual mice. The promising ex-vivo EIS results show great potential for a reliable unstable plaque diagnostic tool for in-vivo catheter integrated intravascular micro EIS sensors.

Despite advances in diagnosis and therapy, atherosclerotic cardiovascular disease remains the leading cause of morbidity and mortality. Predicting metabolically active atherosclerotic lesions has remained an unmet clinical need. Specially, vulnerable atherosclerotic plaques that are prone to rupture are of extremely high-risk and can cause detrimental heart attacks and/or strokes, leading to sudden death. However, since the lumen is not significantly blocked in these cases, such unstable plaques show noncritical stenosis in X-ray angiography and Intravascular Ultrasound (IVUS), which are the two common tools currently available to diagnose coronary artery disease. The ability to distinguish such “vulnerable” plaques remains largely lacking. Therefore, it is of great clinical interest to find improved diagnostic techniques to identify and localize such vulnerable plaques.

Meanwhile, Bio-EIS measures the macroscopic electrical impedance of the tissue. Fat-free tissue is known to be a viable electrical conductor for its high water and electrolytes content. On the other hand, fatty tissue is anhydrous and thus, a poor conductor. The high lipid content, including negatively charged active lipids such as oxidized low density lipoprotein (oxLDL) and foam cells present in the plaque change the endoluminal electrochemical properties, which can be measured as impedance increase over certain frequency band [1]. In our previous work we have demonstrated the ability of EIS to distinguish vulnerable plaque from its surrounding healthy vessel tissue [2], here we demonstrate EIS in-vivo with our micro-fabricated balloon-integrated endoluminal catheter EIS sensor.

5.1 Two point vs. Four point electrode

Simulations of the sensitivity distribution with different EIS sensor designs are carried out to obtain the optimal design of the four electrode EIS sensor. According to the *Helmholtz* Reciprocity theorem, the voltage measured between the sense pair for a 4 electrode configuration, $V_{f,s}$ is shown as equation (1), where Ω is the tissue volume, γ is the point-wise admittivity ($\gamma = \sigma + i\omega\epsilon$), ϕ_f and ϕ_s are the potential field induced by injecting an imaginary normalized current into the force pair and sense pair respectively. In order to utilize numerical methods, we mesh the tissue volume Ω into an N element finite element model, then according to the superposition

theorem, the voltage contribution of the k^{th} element, with admittivity γ_k , $V_{f,s,k}$ is shown as equation (2). $V_{f,s}$ is then the sum of the voltage contributions from all N elements. We can rewrite equation (2) into (3) to obtain the sensitivity at the k^{th} element. With the element's size reducing to the infinitesimal limit, the sensitivity distribution gives us an idea of how the measured voltage changes with respect to admittivity changes in the volume.

$$Z_{4elec} = - \int_{\Omega} \frac{\vec{j}_f \cdot \vec{j}_s}{\gamma} dv \quad 5.1.1$$

$$V_{f,s} = - \int_{\Omega} \gamma \nabla \phi_f \cdot \nabla \phi_s dv \quad 5.1.2$$

$$V_{f,s,k} = -\gamma_k \int_{\Omega_k} \nabla \phi_f \cdot \nabla \phi_s dv \quad 5.1.3$$

$$J = \frac{\partial V_{f,s,k}}{\partial \gamma_k} = - \int_{\Omega_k} \nabla \phi_f \cdot \nabla \phi_s dv \quad 5.1.4$$

$$Z_{2elec} = - \int_{\Omega} \frac{j^2}{\gamma} dv \quad 5.1.5$$

$$Z_{4elec} = - \int_{\Omega} \frac{\vec{j}_f \cdot \vec{j}_s}{\gamma} dv \quad 5.1.6$$

For EIS characterization, we want the sensitivity field to be positive and uniform, which means the tissue's "true" impedance is characterized. Equation (4) shows this ideal situation. However, we cannot obtain such true impedance with tissue EIS, at least with micro electrodes, since we do not have uniform current distribution. With two-electrode scheme, equation (1) can be rewritten in terms of current in (5) to show the measurement impedance Z_{2elec} . We can see Z_{2elec} is the "true" impedance weighted point-wise by the current density j after injecting an imaginary uniform current. Similarly for the 4 electrode scheme, Z_{4elect} is weighted point-wise by the cross product of the current density j_i and j_s produced by injecting uniform currents into the force pair and sense pair respectively. We can see that the dot product in equation (6) is not only non-uniform in value at different locations but also can be zero or negative. Fig. 5.1.1 shows the sensitivity distribution with a naively selected electrode configuration and how non-positive sensitivity regions are quite large.

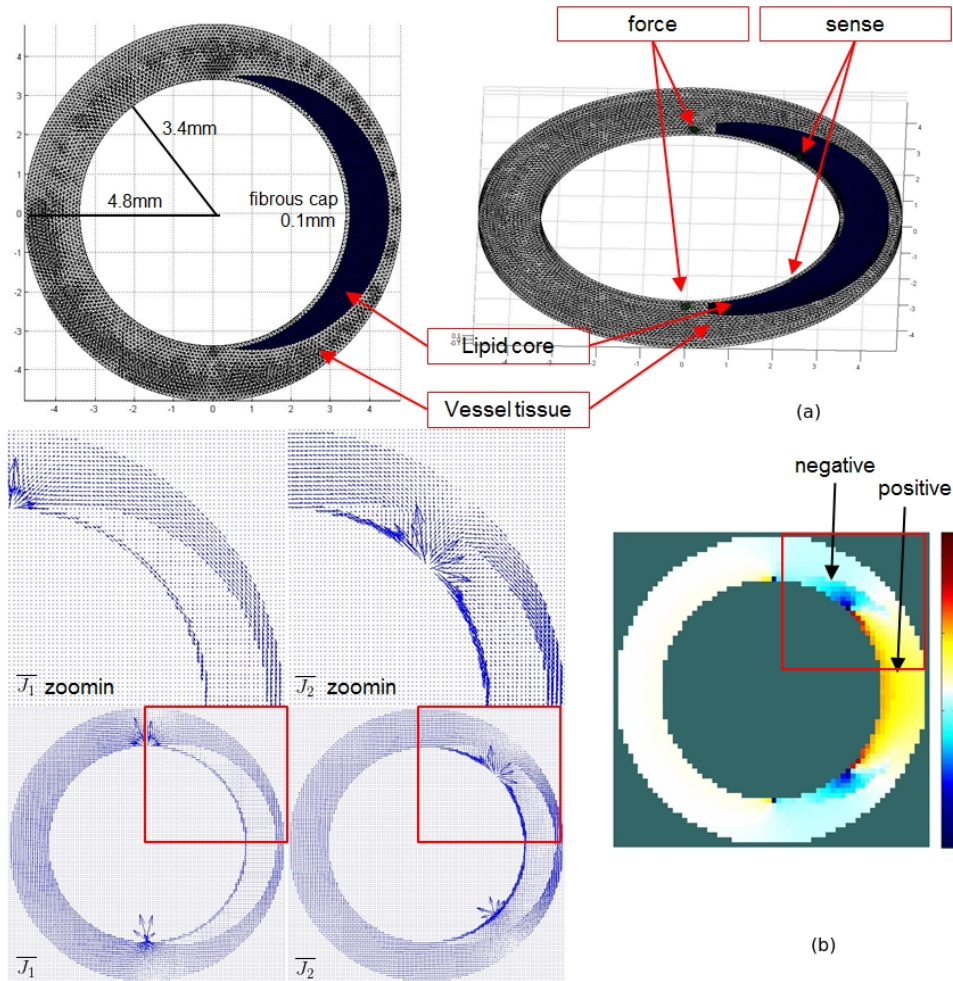
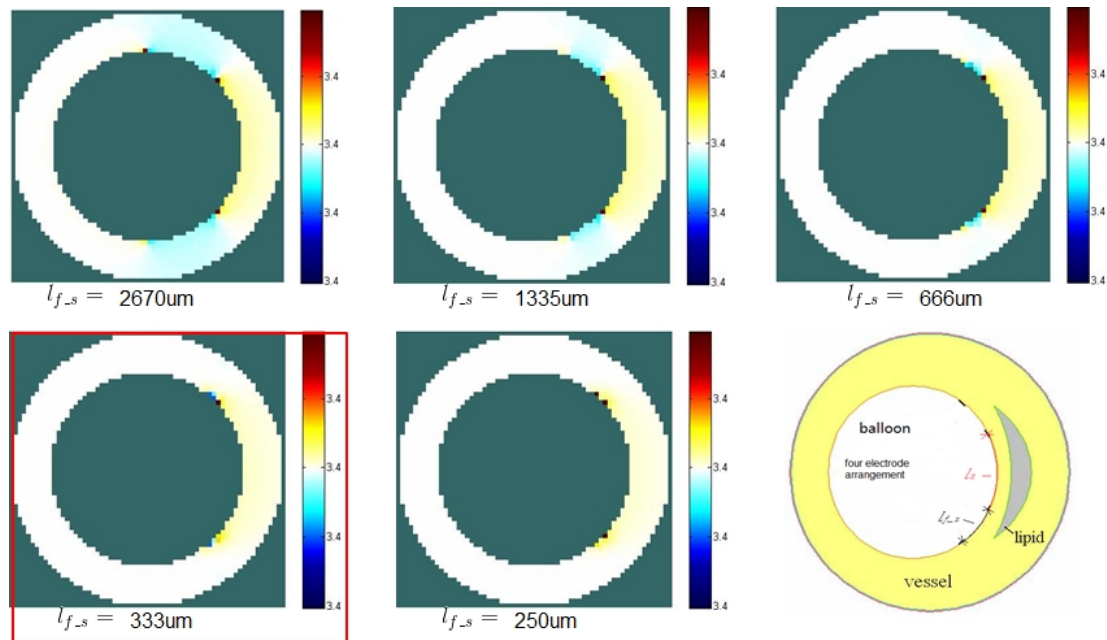


Figure 5.1.1: (a): meshed artery segment with lesion (based on human artery dimensions). (b): left: current vector field with normalized current injected into force electrode pair. middle: current vector field with normalized current injected into sense electrode pair. right: sensitivity distribution of the shown electrode configuration and with lesion present. Yellow and red means positive sensitivity, while means zero sensitivity y and blue means negative sensitivity.

Non-positive values are undesirable because for those volumes we either cannot measure any voltage change with change of impedance, or even worse, we obtain the negative correlated measurement results. Hence, in order to achieve sensible results from a 4 point EIS sensor, we simulate the sensitivity distribution with different electrode configurations (Fig. 2). We then select the sensor design with the optimal sensitivity distribution for the tissue dimensions we work with. The design parameters chosen are $333\mu\text{m}$ between the force and sense spacing (to minimize the negative sensitivity regions between the force and sense electrodes), $666\mu\text{m}$ sense electrode pair spacing (to achieve a positive sensitivity region with depth roughly 0.5 mm , in consideration of the reduced thickness of the mouse samples).



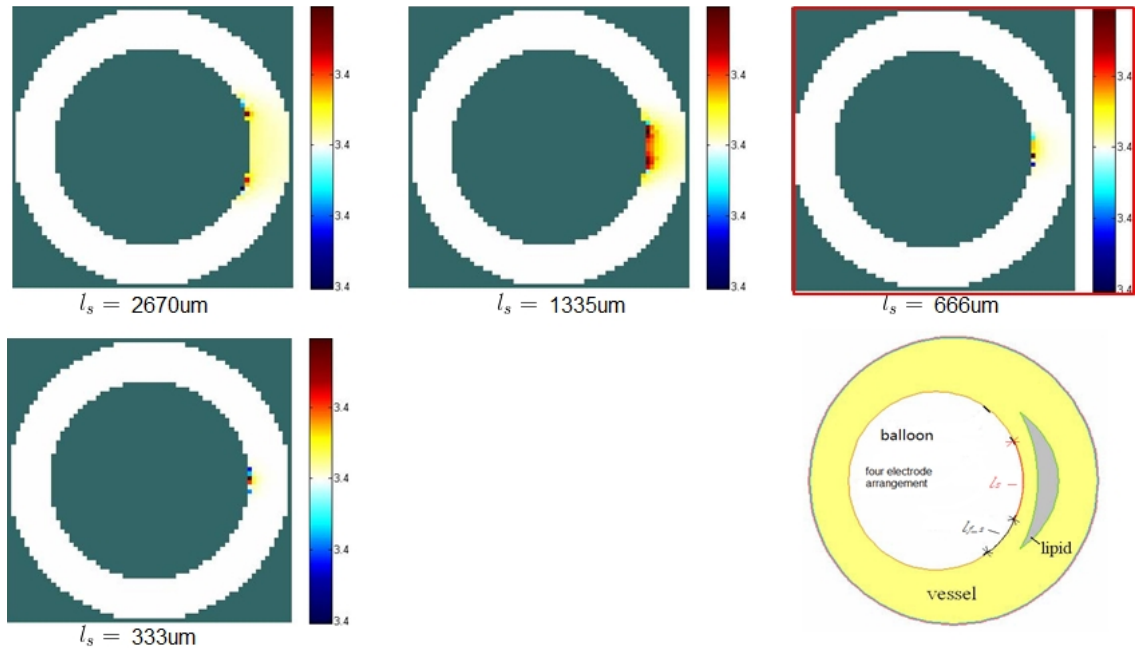


Figure 5.1.2: sensitivity field of different l_s (spacing between sense electrodes). 333 μm is chosen for the least non positive area. Fig : sensitivity fields of different l_{s-f} (spacing between sense and force electrodes). 666 μm is chosen to have a positive region with depth of $\sim 0.5\text{mm}$.

5.2 Intra vascular catheter design and fabrication

The catheter-integrated and balloon-mounted EIS sensor is built on Parylene-C (PAC), a highly flexible and bio-inert material. In addition, Parylene has been widely studied [69-72] and used in various acute and long-term implantable microdevices as a structural material because of their many excellent properties, such as superior barrier property

used to protect the microdevices from moisture. The device has a PA-C/Ti/Au/PA-C sandwich structure as in Fig. 5.2.1.

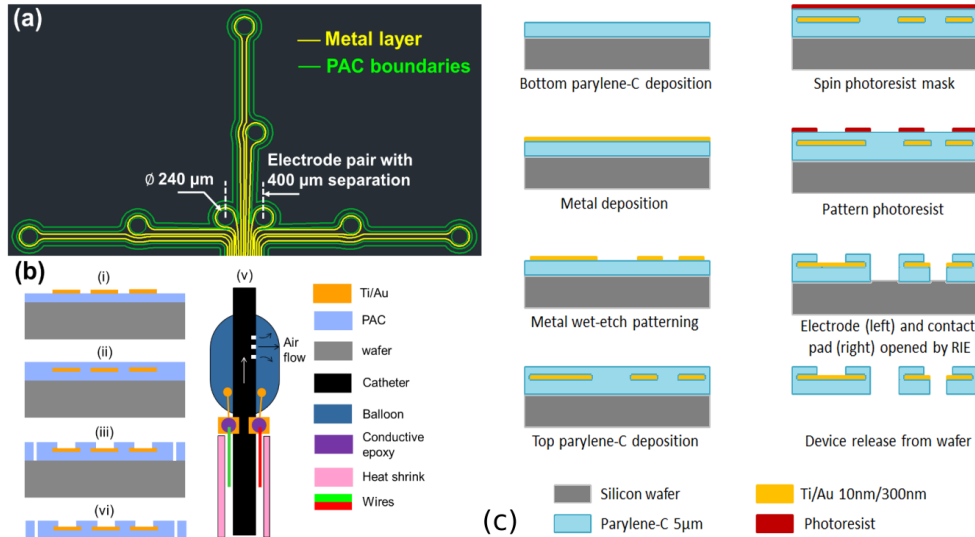


Figure 5.2.1: (a) Design diagram of the Parylene-C electrode design. (b) Assembly schematic of the electrode and balloon catheter integration. (c) Fabrication process of the Parylene-C micro electrode. The 4 layers in the sandwich structure are as follows: $5\mu\text{m}$ Parylene bottom passivation layer, 10nm Ti as adhesion layer, 300nm Au conductive layer, then $5\mu\text{m}$ Parylene top passivation layer. A 20 cm long, $800\mu\text{m}$ diameter plastic catheter with a dilatation medical balloon (Venton Medical, NH) assembled on one end was used for *in vivo* delivery of the sensor, while the other end was connected with a mechanical pump to control the balloon dilatation. Miniature holes were drilled on the catheter sidewall covered by the balloon for air delivery (Fig. 5.2.2). The flexible sensor, after connecting the contact pads with metal wires with conductive epoxy, was fixed on the surface of the balloon by silicone adhesive (Henkel, CT). An insulating heat-shrink

tube was used to wrap the wires and secure their positions alongside the catheter. These wires are then connected with 26 AWG electrical cables to interface with the EIS instrument. Fig. 5.2.2 shows the assembled EIS sensor with a close-up view showing the flexible electrode mounted on the balloon. The EIS measurement is carried out with GAMRY potentiostat (Series-g, Gamry Instruments, PA, USA). Impedance modulus and phase are measured under the frequency range of 1 Hz to 300 KHz.

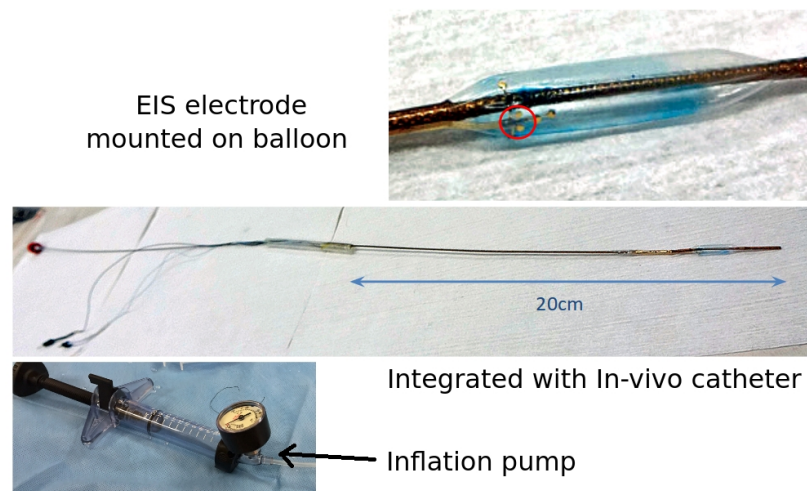


Figure 5.2.2: Finished integrated catheter device. The diameter of the folded balloon is < 1mm, and 3mm inflated. Top: MEA mounted on cardiovascular balloon. Middle: view of assembled device. Bottom: inflation pump to be connected during in-vivo measurement.

5.3 Animal experiments

5.3.1 Ex-vivo animal experiments

The EIS measurement is conducted with GAMRY Series-g Potentiostat system (Gamry Instruments, PA, USA). The EIS micro sensor is connected to the instrument under a 4-point testing scheme (shown in fig. 5.3.1.1) Current is injected into the tissue through the outer force electrode pair and sweeping a frequency range of 1 Hz to 300 KHz. The corresponding AC voltage amplitude and phase change is measured. The impedance modulus and phase are then calculated.

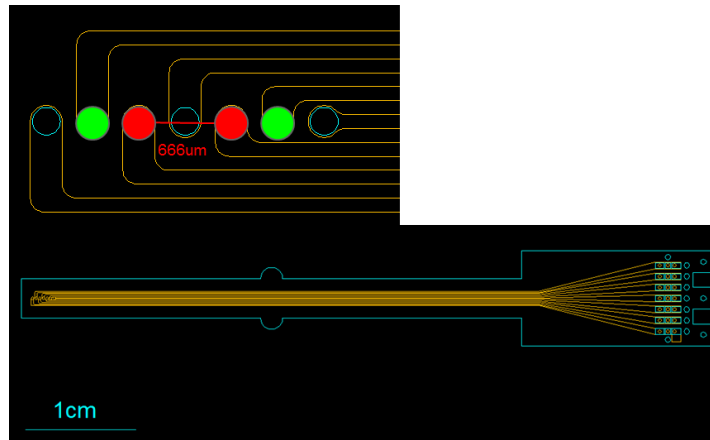


Figure 5.3.1.1: Bottom: Parylene-C based micro electrode array. The spacing between the sense (inner) electrodes is adjustable. Top: Zoomed in view on electrodes, Here it is shown with 666µm spacing. Right: Fabrication process of the micro electrode array.

The EIS sensor is first tested on lean and fatty beef samples as a baseline check. Fig. 5.3.1.3 shows the impedance modulus and phase results of the beef samples. Each data point is measured 3 times; the variation between each measurement is shown with the error bars. We observe a significant rise in impedance modulus in the band 1 KHz – 200

KHz of the fatty sample compared to the lean sample. For the mouse aorta experiment, we tested on 3 samples from 3 different individuals. The aorta samples are cut open along the vessel's longitudinal direction and pinned on a wax dissecting tray for ease of handling (Fig. 5.3.2.1). In the band of 200 Hz – 100 KHz the impedance phase is consistently lower (more capacitive) than that of the control sites. Also the impedance moduli of the lesion sites are 2-5 times higher than those of their control proximity sites for all three individuals.

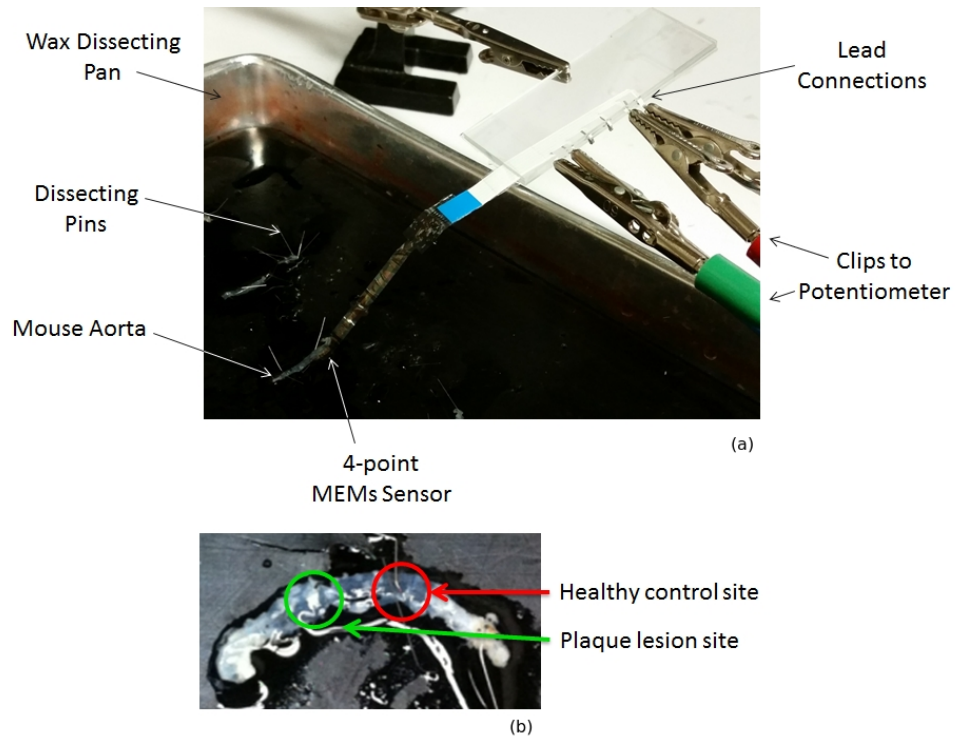


Figure 5.3.1.2: (a): ex-vivo mouse aorta EIS measurement setup. (b): An example of aorta testing sites where plaque and control data are obtained.

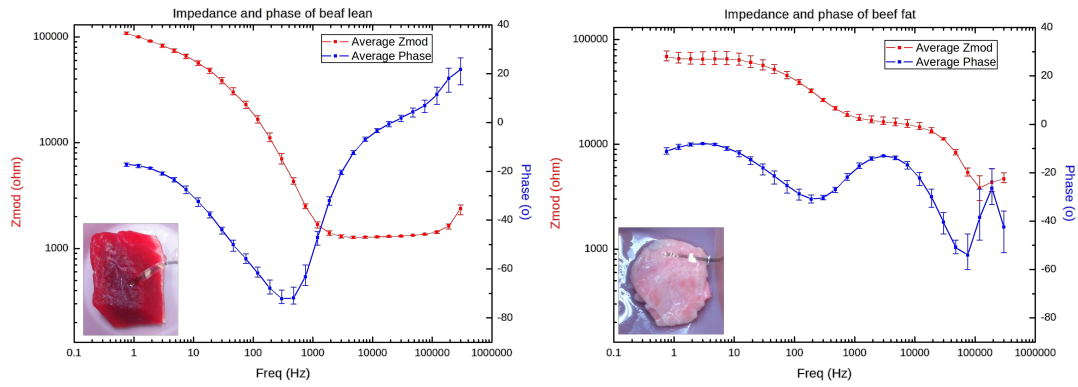


Figure 5.3.1.3: Left: Impedance amplitude and phase curves of lean muscle. Right: Impedance amplitude and phase curves of fat.

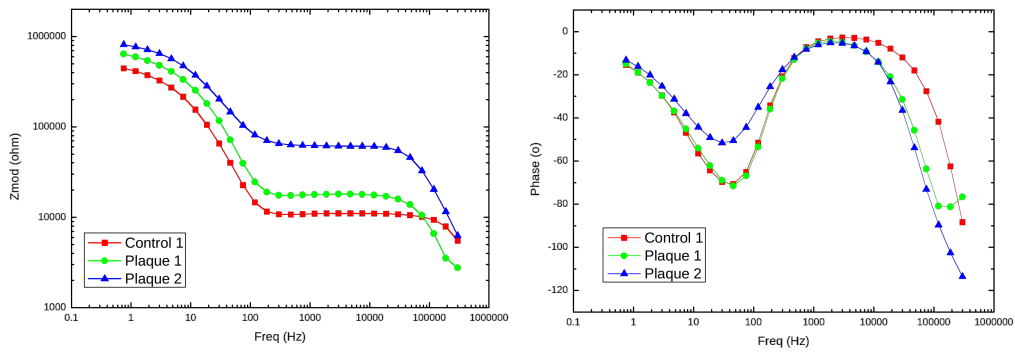


Figure 5.3.1.4: Left: impedance modulus of sample I, II and III mice aortas. We can see that from 200Hz to roughly 100KHz the lesion site has consistently higher impedance modulus than healthy sites. Right: impedance phase of sample I, II and III mice aortas.

It is well accepted that the tissue's bio-impedance has different dominating conducting mechanisms in different frequency bands [73-75]. Understanding the origin of each frequency band behavior is crucial for effective interpretation of the impedance data. On the other hand however, biological tissues have a much more complex structure than regular circuit components.

Under low frequency, the current is mostly conducted in the extra-cellular regime. From Fig. 5.3.1.4, all phase curves show low phase shift and mostly resistive behavior; the capacitive behavior in this region is mostly due to electrolyte double layers at the cell membrane. As frequency increases, the cell membrane itself starts to polarize with the alternating electric field and indicates on the impedance curve an increasing capacitive behavior. From Fig. 5.3.1.4, under 10 Hz we observe a highly resistive region, which may be the extra cellular body fluid (conducting electrolyte). Between 10 Hz to roughly 100 Hz we see a capacitive element entering the impedance curve. This may be due to the fact that the double layer capacitor regime becomes dominant. At around 100 Hz a high pass element becomes dominant and brings the tissue to a resistive behavior. The explanation of this regime needs further investigation; more knowledge of the tissue's internal structure is needed. From around 10 KHz and up a new mechanism that is mostly capacitive starts to dominate. We expect this to be the cell membrane capacitance responding to the higher frequency field. The tissue has entered the β dispersion regime. In this regime we are entering the cells. From the phase graphs in Fig. 5.3.1.4 we can tell that the plaque sites have consistently lower phases (more negative), this may be due to the higher lipid content in these lesion cells. It is possible to attempt to obtain an

equivalent circuit by fitting the impedance curve to explain each regime. However the inherent complex nature of such a distributed circuit demands a more comprehensive study to obtain informative physical meaning of any fitted circuit.

5.3.2 In-vivo animal experiments

A femoral cut-down was performed and a 4-French arterial sheath was placed in the common femoral artery. Under fluoroscopic guidance and iodinated contrast dye injection, the EIS sensor was introduced through the femoral cut and then advanced to the abdominal aorta for live interrogation. (Fig. 5.3.2.1) *In vivo* and *ex vivo* measurements were obtained in the abdominal aorta between the renal artery bifurcation and the aortic bifurcation. Following animal harvesting, *ex vivo* measurements were conducted in various segments with different levels of lipid burden in the descending thoracic aorta and abdominal aorta at the level of the renal arteries. A pair of electrodes with 400 μm separation was chosen out of eight available to conduct the electrical impedance measurement. Three replicates were performed at each interrogation site. AC signals with peak-to-peak voltages <50 mV and frequencies ranging from 1kHz to 300kHz were delivered at each site. The impedance magnitude and phase were recorded. Meanwhile Angiograms were obtained during fluoroscopy to document vessel anatomy and verify appropriate advancement of the EIS sensor. Measurements were obtained in control rabbit aortas and in various segments of the high-fat fed rabbit aortas. Segments that were analyzed were the descending thoracic aorta (severe plaque), abdominal aorta at the level of the renal artery bifurcation (moderate plaque), and abdominal aorta between the renal

artery bifurcation and the aortic bifurcation (mild plaque). Results were compared to plaque burden as assessed by lipid content and inflammatory activation by macrophage. During the in-vivo EIS measurements, the balloon on which the EIS electrodes was mounted was inflated to about 10 psi for optimal endoluminal contact. A portion of each aorta was fixed in 4% paraformaldehyde, embedded in paraffin and serially sectioned for histological analyses. Lipids were identified by hematoxylin and eosin staining and macrophages by F4/80 staining (Fig. 4) so that EIS data can be correlated.

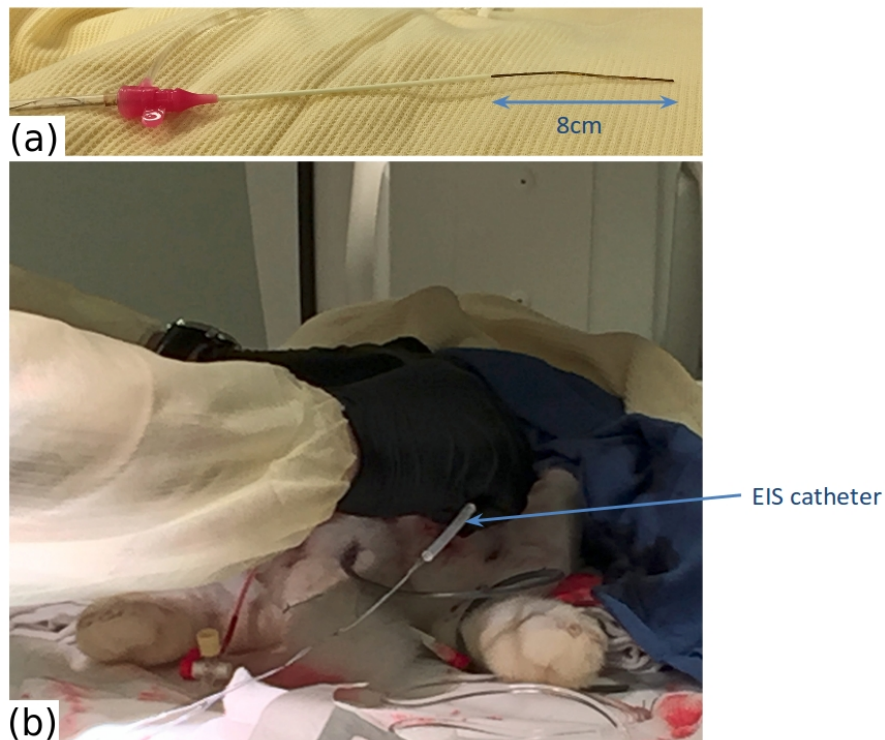


Figure 5.3.2.1: Finished integrated catheter device. The diameter of the folded balloon is $< 1\text{mm}$, and 3mm inflated. Top: MEA mounted on cardiovascular balloon. Middle: view of assembled device. Bottom: inflation pump to be connected during in-vivo measurement.

From the *in vivo* measurement data, the frequency sweep revealed similar impedance profiles in the low frequency range 1 – 10 kHz, consistent with a more resistive characteristic in tissues (Fig. 5.3.2.3) [6]. However, significant differences in impedance appeared in the high frequency range 1kHz – 300 kHz, consistent with a more capacitive behavior of the tissue ($P < 0.05$ for control vs. moderate plaque, control vs. severe plaque, and mild vs. severe plaque, $n=5$ controls, $n=3$ high fat; $P < 0.05$ for control vs. mild plaque occurred at 300 kHz; and $P > 0.05$ for moderate vs. severe plaque). Apparently, impedance magnitude increased as the plaque burden becomes more severe, which is verified using IVUS and immunohistochemistry (Fig. 5.3.2.2). The largest difference between impedances was at a frequency of 300 kHz. The impedance difference in high-frequency regime is mostly due to the fatty cellular content from the vulnerable plaques. The integrated micro EIS catheter has proven to have great potential to be a valuable vulnerable plaque diagnostic tool.

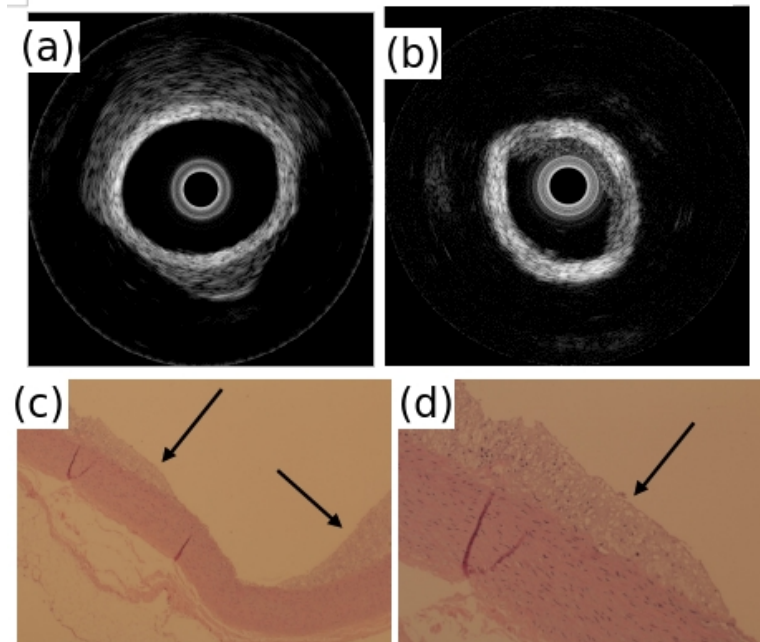


Figure 5.3.2.2: (a) & (b) Intravascular Ultrasound (IVUS) images of aorta intersection showing the existence of plaque at test site. (c) & (d) Histology of the plaque indicating high lipid content region with black arrows.

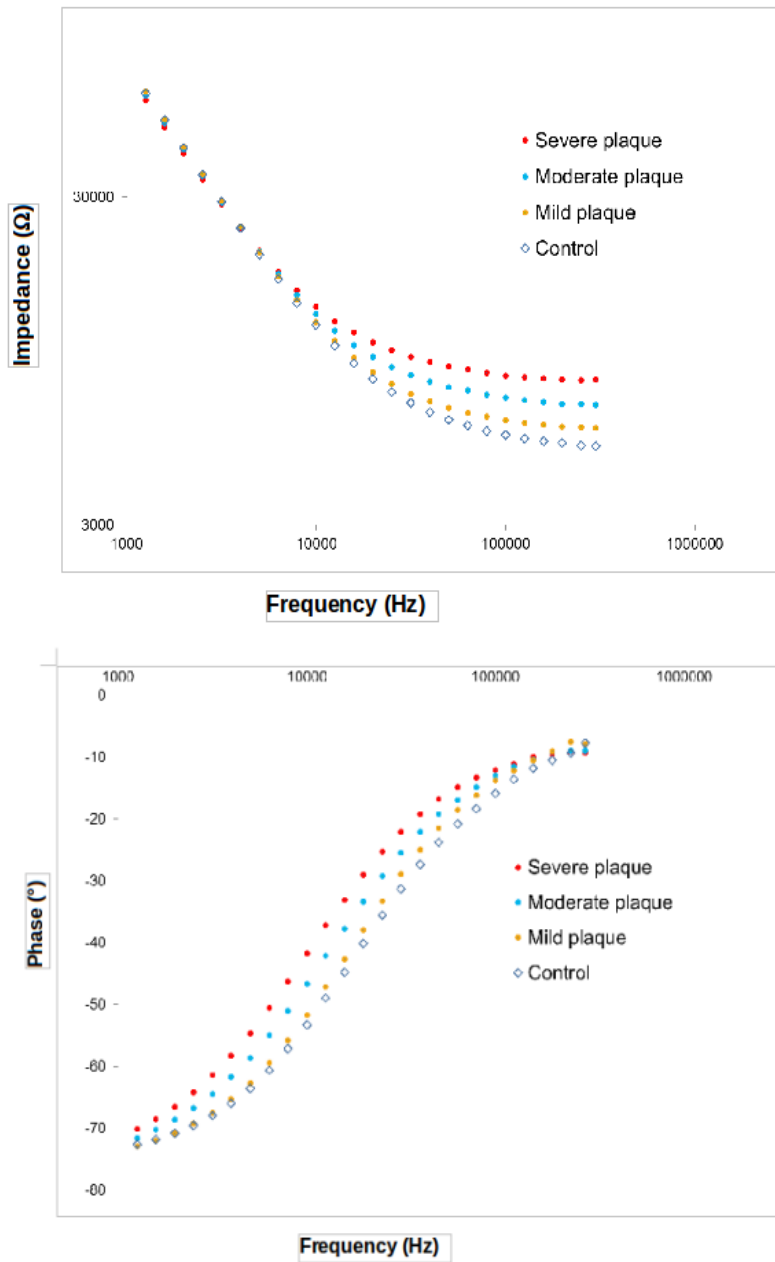


Figure 5.3.2.3: EIS results from different sites showing the impedance (top) and phase (bottom) differences between plaques of conditions from control (i.e., no plaque) to severe plaque.

EIT FOR ENDOLUMINAL PLAQUE DETECTION**6.1 Electrode Configuration**

EIT has been demonstrated as a powerful biomedical imaging modality and utilized in various practical applications. The mostly applied electrode configuration is to place multiple electrodes around the peripheral of a solid object and reconstructing the conductivity distribution within the interior region formed by the electrodes belt (2D) or array (3D). Here we call it “inward imaging” as illustrated in Fig. 6.1.1 (a). Commercialized applications including lung ventilation monitoring, brain activity detection, and breast cancer detection, etc. Inward imaging is used because it is a straight forward and non-invasive method. With fatty liver diagnoses application in the following sections we will be using the inward imaging in a belt fashion.

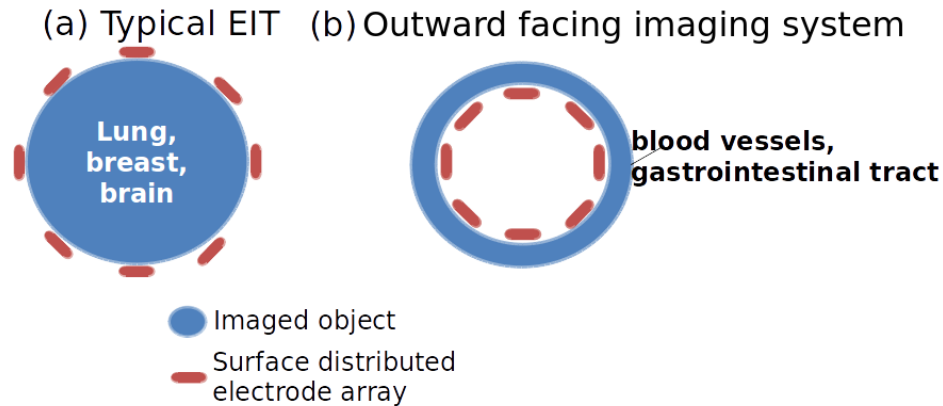


Fig 6.1.1 Inward imaging and outward imaging In contrast to inward imaging, as a new imaging modality, we have developed “outward imaging”.

Numerous bio-tissues that are of great clinical interest possess a tubular geometry, such as blood vessel, gastrointestinal tract, etc. The existing clinical tools for such tubular objects are mostly catheter-based wherein a catheter is inserted into the endoluminal space of these objects for subsequent detection. Therefore, to apply EIT on these objects, it will be critical to follow the same catheter based methodology and have necessary electrodes mounted on the catheter and placed in the endoluminal space for EIT imaging. As shown in Fig. 6.1.1 (b), we refer to such configuration as outward imaging. In the following sections we use this scheme to explore catheter mounted intra-vascular interrogation EIT probe to detect rupture prone plaques in the blood vessels.

The significance and impact of such outward imaging methodology lies in two aspects: First, this has not been demonstrated in previous literature except for a pure simulation study in [76]. It poses interesting mathematical challenges and help to broaden the

fundamental understanding of EIT theory. Second, application of EIT imaging on these tubular organs has great clinical value as EIT (utilizing voltage and current as measuring vehicles) can be advantageous as compared to existing tools since the conductivity itself is obtained.

6.2 Resolution Study

There have been numerous resolution studies with the inward system [77-82]. In this section we answer the question of the resolution resolvable in ideal from the outward imaging system in outward imaging.

Number of Electrodes

First we examine how the outward EIT system's performance varies with different number of electrodes.

Distance from probe

Similar to inward imaging, the EIT algorithm can resolve better the objects closer to the electrodes. We try to image an object of 1mm in diameter at different distances to the probe. Figure 6.2.1 shows the reconstructed image.

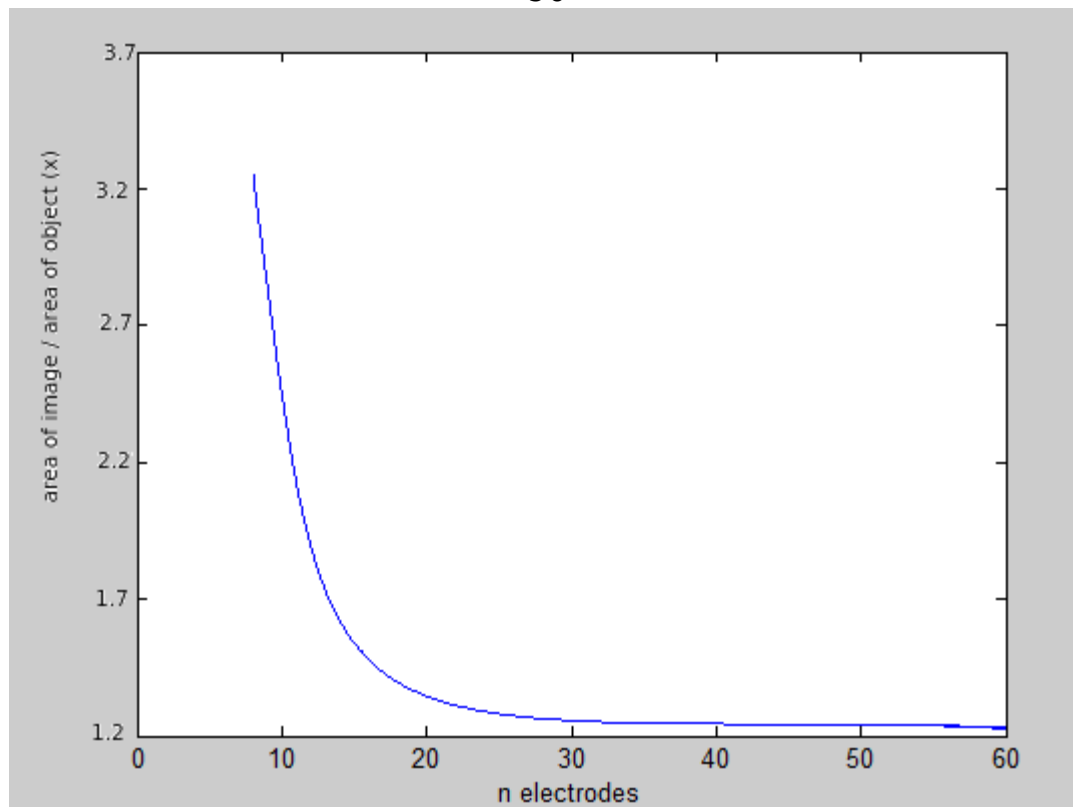


Fig 6.2.1: Spread vs. number of electrodes. Spread is defined by the area of the reconstructed image divided by the area of the real object.

We can see that the spread decreases rapidly from 4 electrodes to 30 electrodes, after 30 electrodes the performances has is only marginally improved with more electrodes. Hence the following systems we choose 32 electrode systems.

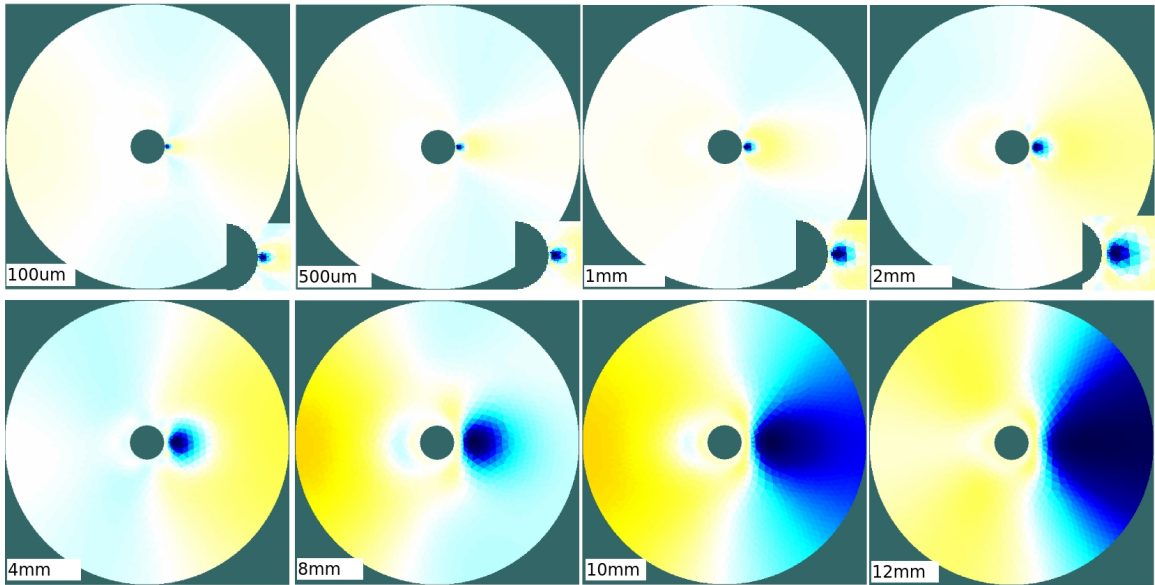


Fig 6.2.2: Reconstructed image of same 1mm diameter object placed at different distances away from the probe edge. The probe diameter is 25mm. We define the edge of a reconstructed object to be consisted of pixels valued above the 10% of the absolute peak value (maximum for high conductivity or minimum for low conductivity). Fig 6.2.2 shows the first row of Fig 6.2.1 after the 10% crop.

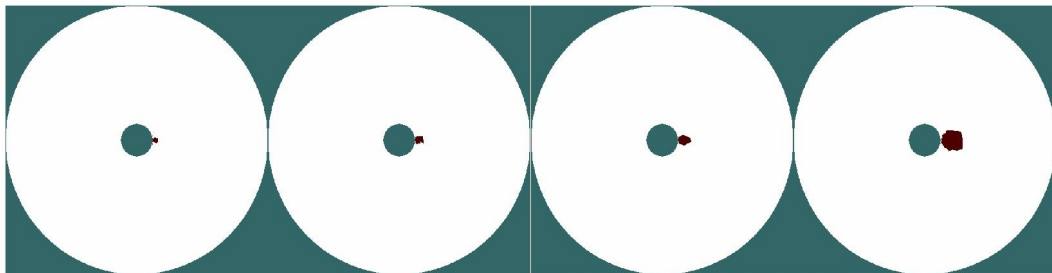


Fig 6.2.3: 100um – 2mm distances (first row of Fig 6.2.1) after 10% threshold crop, we define these to be the constructed object size. We define resolution and spread are defined as equations 6.2.1 and 6.2.2, where $|\cdot|$ means the area.

$$res = \sqrt{\frac{|reconstructed\ image|}{|tank|}}$$

$$spread = \sqrt{\frac{|reconstructed\ image|}{|model\ object|}}$$

Below we plot the resolution vs. distance and spread vs. distance for the above simulation experiment. We can see that <1mm distance both resolution and spread are relatively linear to the distance, >1mm the the resolution and spread grows rapidly as the object becomes not well defined in the reconstructed images.

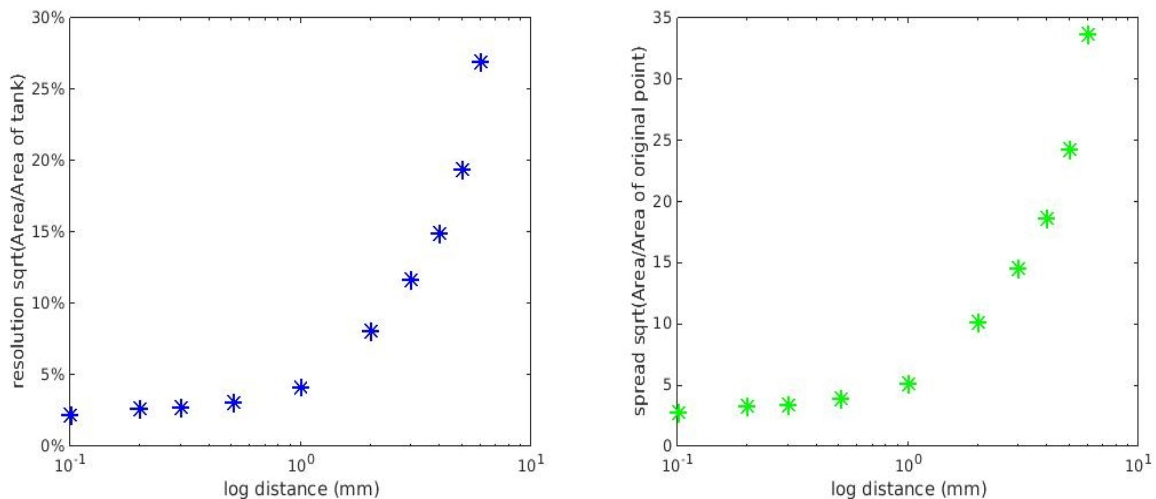


Fig 6.2.4: left: resolution vs. distance. Right: spread vs. distance. It is apparent that the object becomes large rapidly when it is > 1mm to the probe edge. We can

see that within 1mm there is a “linear” region that the reconstructed image is “grows” linearly as the distance increases. For the 25 mm diameter probe the linear region is within 1mm.

Object size

The size of the object also affects resolution and spread of a particular EIT system. Below we show object of various radius ranging from 50um to 5mm in close proximity (100um distance from the probe edge). Fig 6.2.5 shows the 10% threshold cropped image.

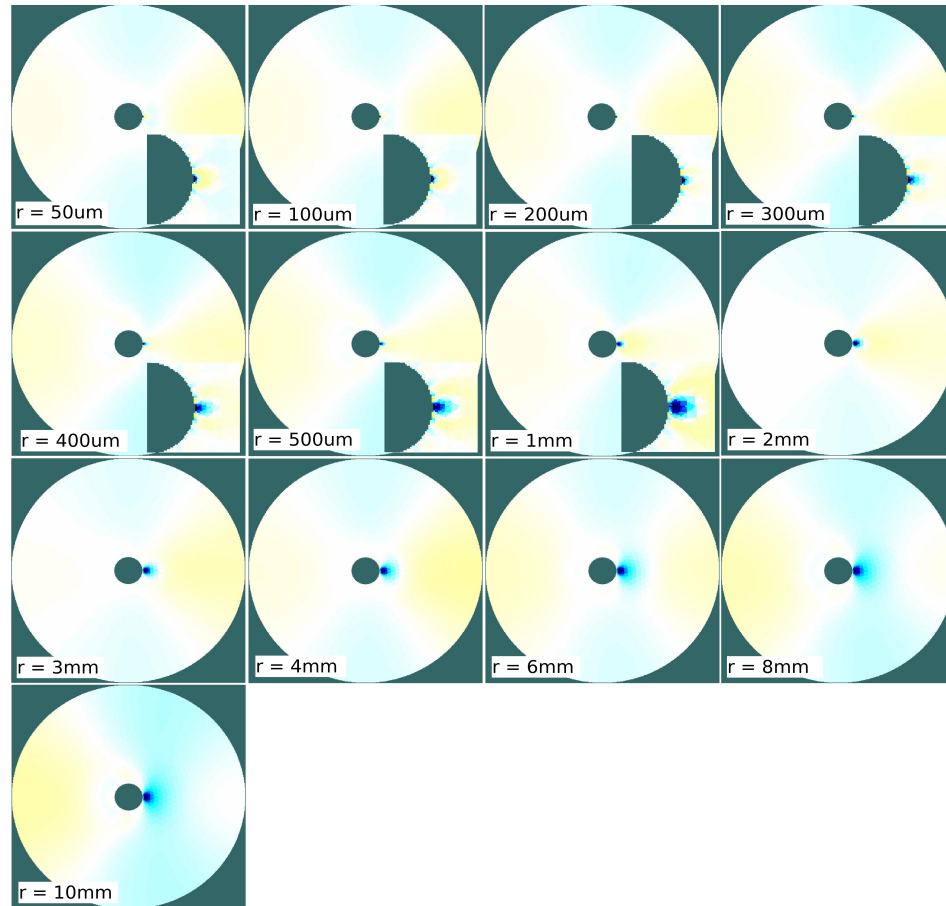


Fig 6.2.5: reconstructed image of radius r at distance $100\mu\text{m}$ from the probe edge.

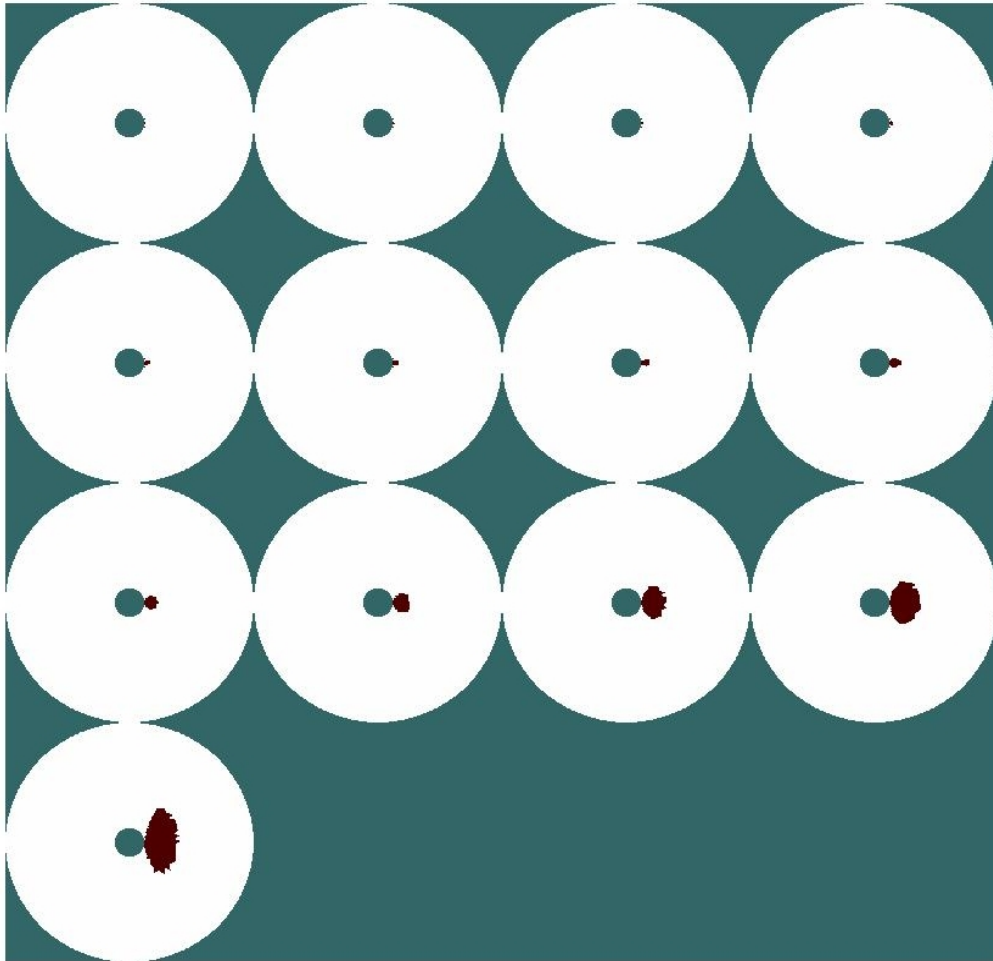


Fig 6.2.6: 10% threshold cropped images from Fig 6.2.4, used to define the reconstructed image area and size.

We can see in Fig 6.2.6 that the resolution and spread performance as the object size becomes bigger. We can see the resolution becomes bigger. This is as expected since the resolution is defined as the area of the reconstructed image to the area of the tank. What is worth noting is that the spread of the reconstructed image is very high when the object is small, then it rapidly decreases to about

1.3x as the object radius is $> 1\text{mm}$ and stays flat as the object size increases from thereon.

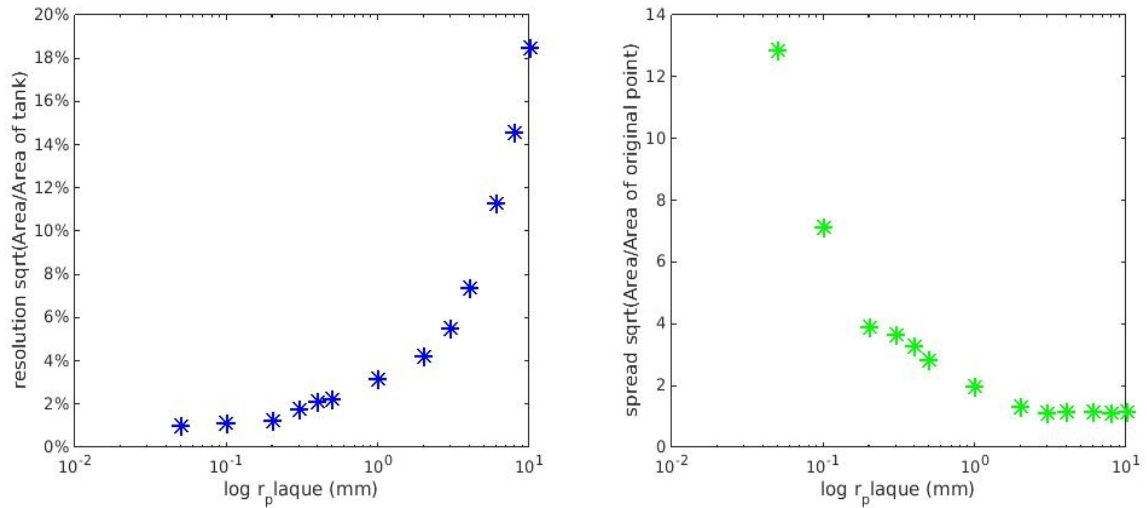


Fig 6.2.7: Left: resolution of the reconstructed image with radius r at distance 100 μm to probe edge. Right spread of the reconstructed image with radius r at distance 100 μm to probe edge. Distance and object size

Now we put the distance and object size study together and plot comprehensive results of the various sized object placed at varied distance. In Fig 4.2.7 the top two rows are object of radius 0.5mm placed at various distances of 100 μm - 6mm, row 3-4 object of radius 2mm, bottom two rows object of radius 4mm. The left shows the raw reconstructed images, the right shows the 10% cropped images. The resolution and spread curves are plotted in Fig 6.2.8.

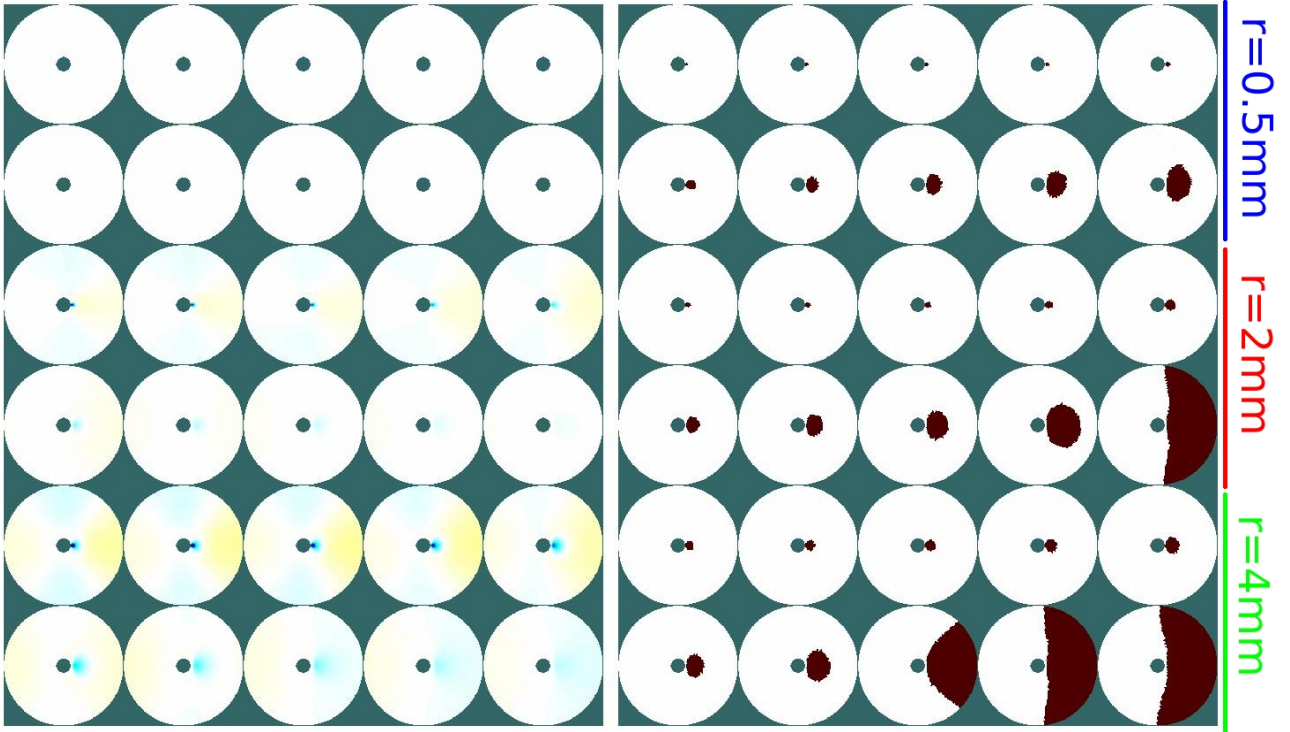


Fig 6.2.8 Combined result of varied radius vs. varied distance.

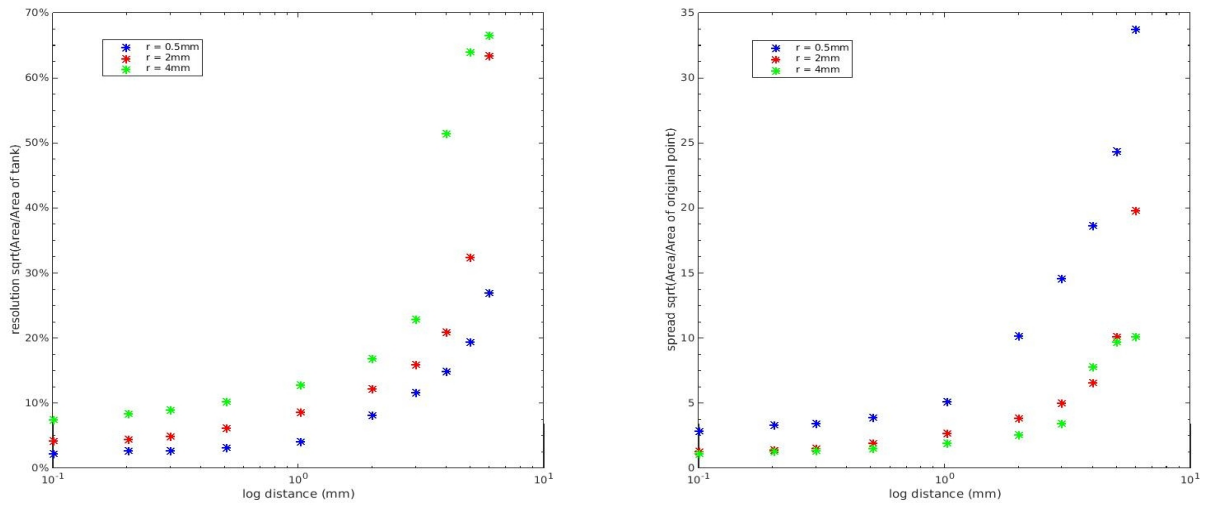


Fig 6.2.9: Left: resolution vs. distance (blue object $r = 0.5\text{mm}$, red $r = 2\text{mm}$, green $r = 4\text{mm}$) Right: spread vs. distance (blue object $r = 0.5\text{mm}$, red $r = 2\text{mm}$, green $r = 4\text{mm}$)

We see that for all three different sized objects the reconstructed resolution and spread becomes magnified as the object is further from the probe. However a consistent linear region exists for all three object, that is for this probe of 25mm in diameter, the distance of linear region is roughly $<1\text{mm}$. Worth noting is that the spread seems to become worse (bigger) as the object size is smaller.

6.3 Simulated experiments

We conduct a simulated experiment below. The volume conductor (the tissue volume) Ω is discretized as an FEM model assuming constant conductivity within each tissue type with the conductivity shown in Table 1 (Slager 1992). To simplify calculations only conductivity is used in the simulation.

The FEM artery model was designed as the following. The lipid, located on the vessel wall, had a crescent shape on the cross section. The shape of the vessel lumen on the cross section was round with a radius of 3.4 mm. The thickness of the vessel wall was 1.4 mm and the longitudinal length of the vessel was 10 mm. Each electrode was a 0.1 mm diameter circle. 3D Finite Element Model (FEM) of the atheromatous artery was then created with the mesh sized adaptive to the geometry with a max spatial resolution of $0.2 \times 0.2 \times 0.2 \text{ mm}^3$, it is shown in

Figure 6.3.1 Voltage data is generated by injected current through adjacent pairs of the 32 electrodes sequentially where the FEM model was used to solve for the potential distribution in the modeled volume. Using the adjacent electrode current injection scheme, 464 unique voltage pickup combinations occurred when not measuring from current injection electrodes. Since the ratio of vessel thickness to the separation between the adjacent electrodes is greater than 1, the voltage measurement is hardly affected by the extra-vascular conditions (Cho 2005).

Fig 6.3.1 (a) shows the 3D model generated with Netgen, an open source software for meshing. Fig 6.3.1 (b) shows the mesh in detail. There are much denser meshes close to the electrodes. Netgen does adaptive meshing to accommodate fine features in the FEM model. The FEM model shows the an oval shaped low conductivity plaque (high lipid content) in the vessel wall. Inside the vessel blood fills the volume. The inner hollow area is where the probe is. It is not meshed as the probe is not conductive electrically except the surface electrodes.

Tissue	Electrical conductivity (S/m)
Blood	0.68
Vessel	0.43
Lipid	0.034
Probe	10^{-19}

Table 6.3.1: Conductivity values used in FEM simulation [Slager 1992]

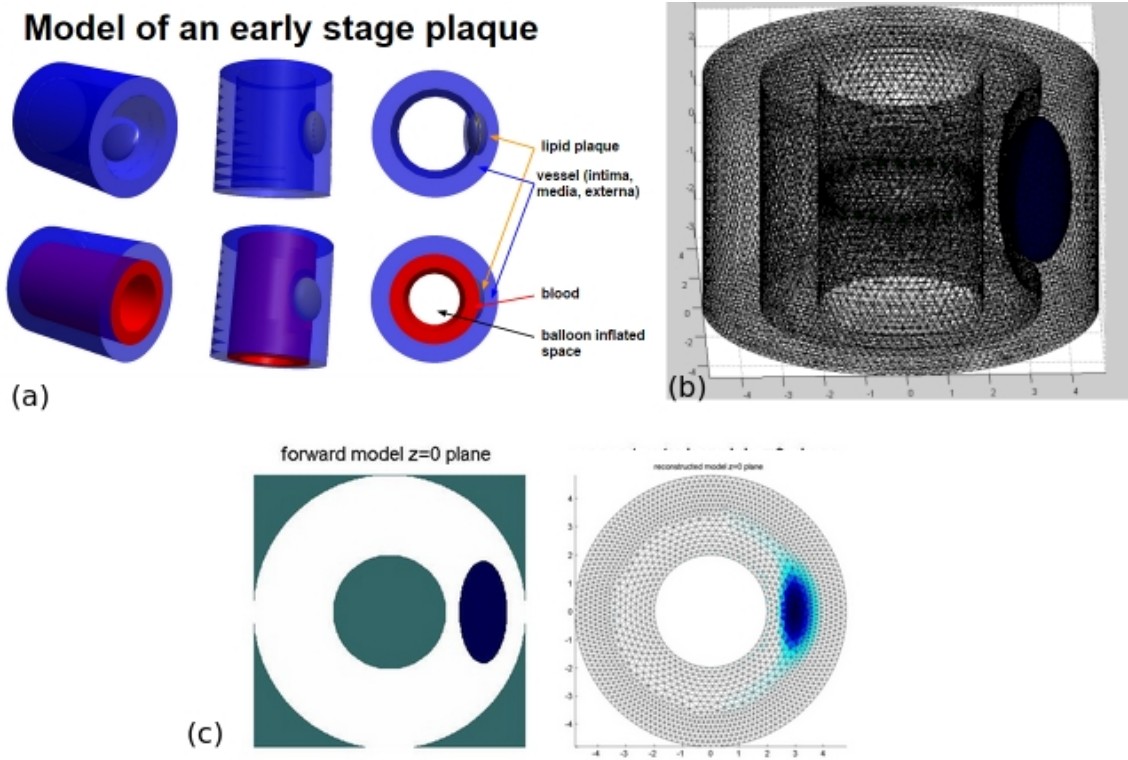


Fig 6.3.1: (a) 3D FEM model used generated with Netgen. (b) detailed mesh, the dense electrode meshes are on the inner wall and are attached to the vessel wall and are facing outward. The plaque is shown as the blue oval shaped obstacle. (c) Left: cross section (on electrode level) of the model in (b). Right: Reconstructed image shown at the same level cross section.

6.4 Ex-vivo experiments

We first do a test experiment with the outward imaging electrode probe. As shown in Fig 6.4.1 each there are 32 electrodes equally spaced and facing outward on a non-conducting rigid plastic probe. The diameter of the probe is

15mm and each individual electrode is 1mm in diameter. The electrode surfaces has been electroplated with Platinum-black in order to increase the elective surface area and reduce the double layer impedance. Fig 4.4.1 bottom row shows the reconstructed images of the “pen in saline” experiment. Difference imaging is used, reference data is taken with plain saline and inhomogeneous data is taken with the pen introduced at the shown locations.

We move on to image the aorta with “plaque” scenario. The pig aorta is purchased from saluter house and thawed overnight for experiment. Since the aorta was healthy with no plaques, we mimic the plaque with pig fat subcutaneous fat tissue. Fat tissue was purchased from local supermarket. The assumption is since vulnerable plaque has a very high content of lipids it is reasonable to assume such plaques will have high impedance similar to the fatty tissue. Fig 6.4.2 shows the experiment setup. From Fig 6.4.2 (c) and (d) we see that there are significant differences in electrical impedance properties between fat and aorta wall. If we use the impedance modulus as the voltage data for reconstruction, the fatty tissue impedance is much higher than the that of the aorta, which will translate to low conductivity of the fatty tissues on the reconstructed image. The difference in impedance modulus seem to grow bigger as the frequency increases up to our 250Khz instrument limit. Hence 250Khz was used in obtaining the voltage data.



Fig 6.4.1: Top left: electrode in saline. Top right: electrode zoom-in view. Middle row: “pen in saline” experiment setup. Bottom row: reconstructed images corresponding to pen location.

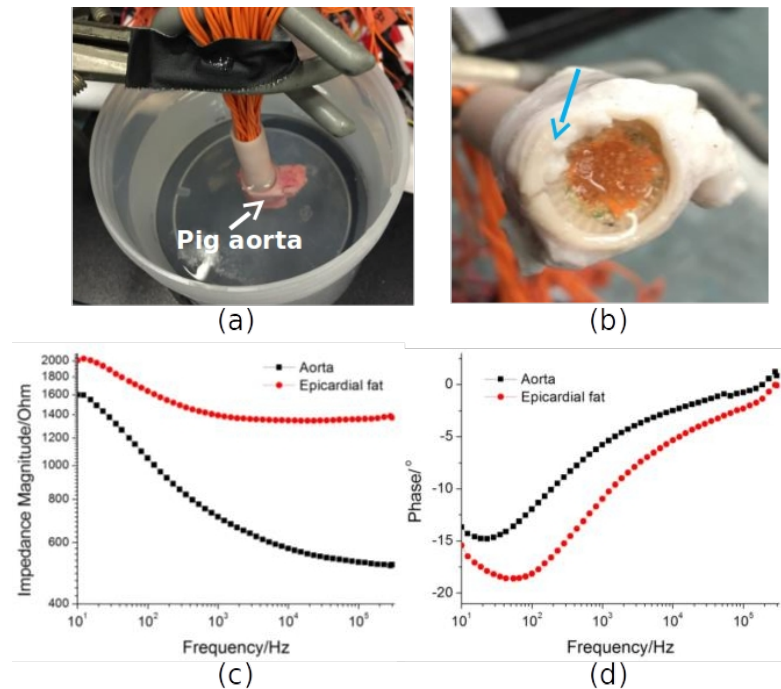


Fig 6.4.2: (a) shows the EIT imaging results with the swine aorta sample and subcutaneous fat mimicking plaques through implementing a one-step fast algorithm. (b) further highlights the dark blue regions that represent the position of the fat tissue. (c) shows the EIS impedance modulus from 10hz to 250Khz. (d) shows the EIS impedance phase from 10hz to 250Khz.

Fig 6.4.3 shows the reconstructed image from the ex-vivo experiment. We see that the reconstructed image corresponds well to the location of the fatty tissue. With 30% peak value crop (elements with conductivity lower than 30% of the absolute peak value of the feature is not accepted and cropped off), the accepted pixels seems to contain the core of the fatty tissue. Difference imaging is used in

this experiment. Reference data is aorta alone and inhomogeneous data is aorta with fatty tissue inserted.

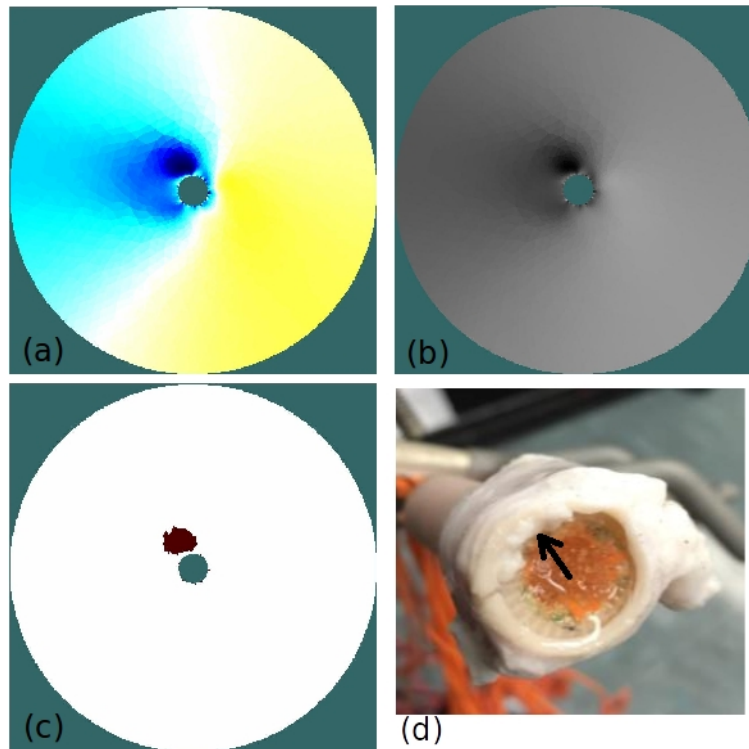


Fig 6.4.3: (a) red-blue scale reconstructed image with ex-vivo aorta tissue. (b) gray-scale reconstructed image with ex-vivo aorta tissue. (c) accepted reconstructed image with pixels above 30% peak threshold crop. (d) ex-vivo aorta tissue with fat added to mimic plaque. (black arrow).

EIT FOR FATTY LIVER EARLY DETECTION

7.1 Electrode configuration

We use the conventional inward imaging scheme for non-invasive Fatty Liver detection application. The 32 electrodes are placed at equal distance on the same level of the body. Fig. 7.1.1 shows the relative position of the liver inside a human body. Fig. 7.1.2. shows the cross sectional CT scan and major organs highlighted on this level.



Fig. 7.1.1: relative position of liver inside the human body.

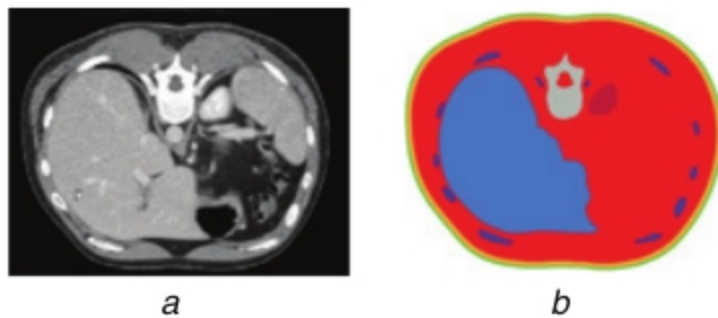


Fig. 7.1.2: (a): CT scan of upper abdominal cross section. (b) major organ highlighted (large blue region is liver).

The placement of the belt should take two factors into consideration: (1) It should maximize the the cross section of the liver we choose 1 inch above the lowest point of the rib cage. (2) It should be subjected to minimal temporal effect due to movement of other organs since the difference data (at different frequencies) are at different moments in time. The heart beats and lungs expand and contract as the patient breathes. The belt level should be relatively far away so that the voltage difference are not dominant by these organs. A good position that considers above both factors has been determined to be one inch above the lowest point of the rib cage. Fig. 7.1.3. shows the electrode placement on a human body.

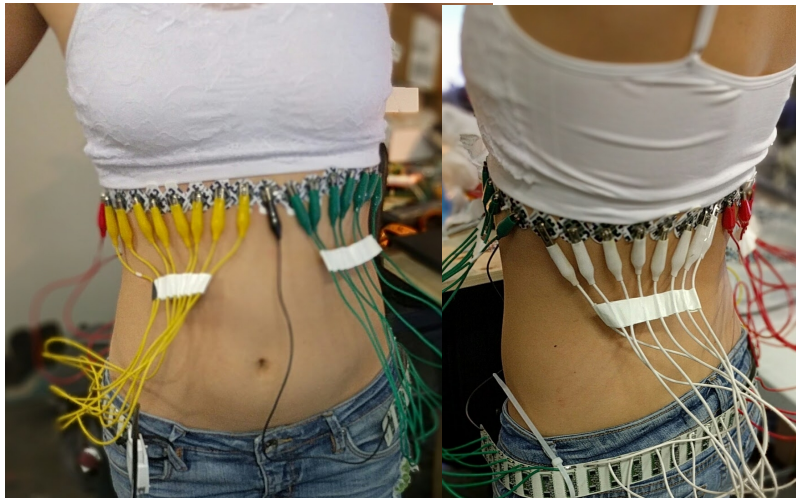


Fig. 7.1.3: electrode placement on human thorax

7.2 Conductivity of organs and Multi-frequency difference imaging

Table 7.2.1 shows the average conductivity of major abdominal tissues from historical measurement surveys [cite]. We can see that for healthy liver its conductivity is around 0.075S/m. In the surrounding area a large organ is the stomach (0.523S/m), surrounding the organs are muscle (0.266S/m) and subcutaneous fat (0.022). Considering only the large organs that will heavily influence the EIT image, we can see the body as a low conductive fat layer wrapping over a more conductive muscle layer (0.266S/m); and with a relatively low conductive large region (liver) and high conductive region (stomach) on the inside.

Component	Conductivity (S/m)	Component	Conductivity (S/m)
Liver	0.075	Muscle	0.266
Stomach	0.523	Fat	0.022
Spinal cord	0.028	Skin	0.001

Table 7.2.1: conductivity of major abdominal tissues from literature [cite].

In order to use difference imaging on the human body we need to take frequency differences

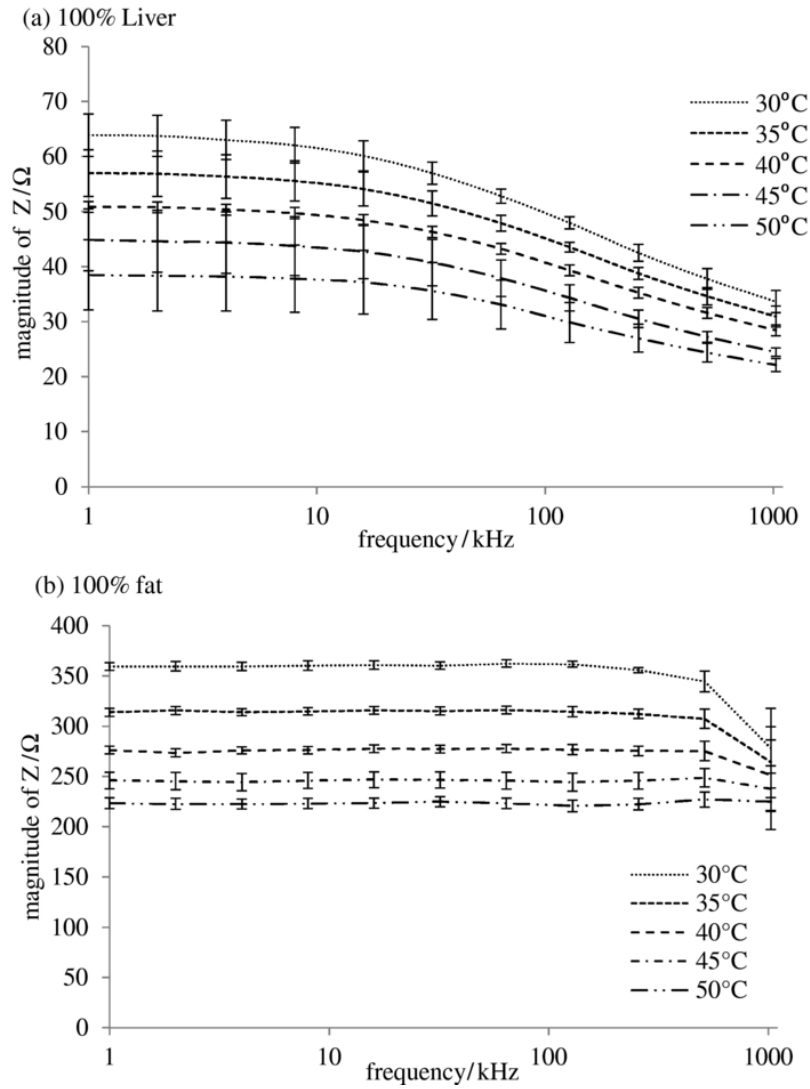


Fig 7.2.2: The effect of temperature on the electrical impedance spectra of (a) 100% liver and (b) 100% fat.

7.3 Simulated experiments

This section consists of a series of simulation studies to characterize the feasibility to reconstruct liver with accurate conductivity values, and the factors that affect the quality of the reconstruction. An FEM model that mimics the human thorax is constructed to generate the voltage data. Fig. 7.3.1 shows the FEM model and the conductivities used for each organ. Conductivities at 250Khz are used for the simulations.

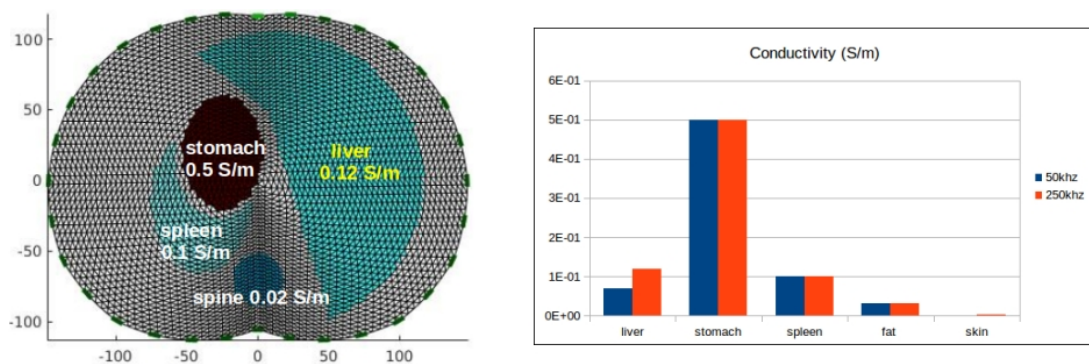


Fig. 7.3.1: Left: FEM model used to generate voltage data. Right: Conductivity of each organ at 50Khz and 250Khz.

In order to simulate various “severities” of the fatty liver, conductivity of liver are modified to be 100% normal, 95% normal, 90% normal, 80% normal and 70% normal. Fig. 7.3.2 shows from left to right, the reconstructed images of healthy liver to severely fatty respectively. We can see that the reconstructed conductivity of liver becomes lower in general as the model changes.

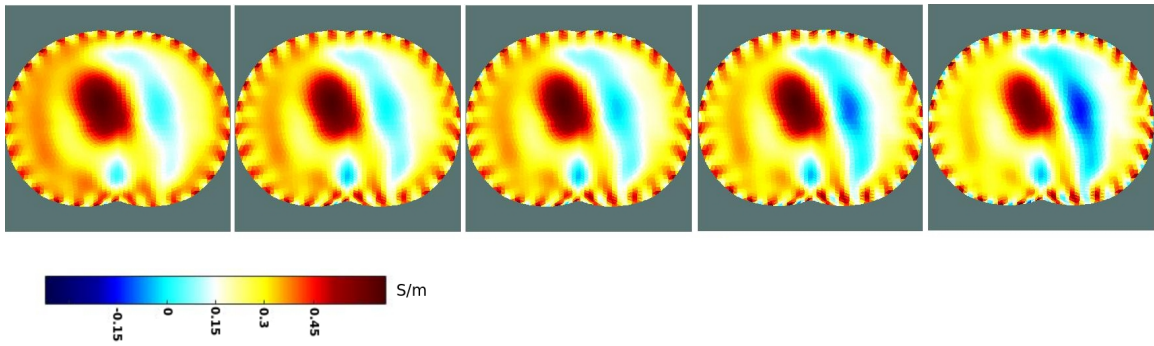


Fig. 7.3.2: From left to right: 100% liver conductivity (healthy), 95% conductivity, 90% conductivity, 80% conductivity, and 70% conductivity.

The reconstructed images from Fig. 7.3.2 are then being processed to include 10% of the minimum value in the liver region. All included elements are then averaged and the results are considered here the effective conductivity in the liver region of each reconstructed result. Fig. 7.3.3 shows the plot of such reconstructed effective conductivity readings vs. model conductivities. We see an excellent linear correlation between the reconstructed and the model.

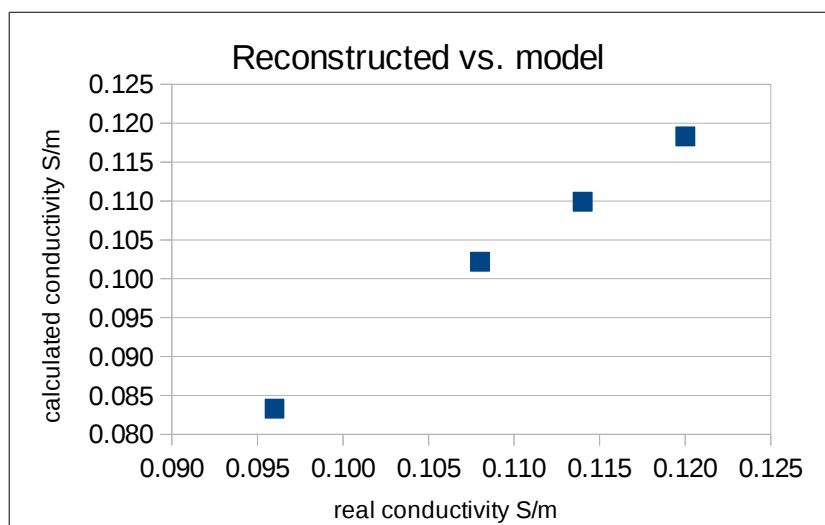


Fig 7.3.3: Reconstructed “effective” conductivity in the liver region vs. the modeled liver conductivity plot.

In practice there will be unavoidable noises in the human body and the instrument. In the following we show how the quality of reconstructed image are affected by adding random noise to voltage data. Fig. 7.3.4 shows with 1% random noise added to all channels the image is distorted from the correct shapes. However, calculated conductivity in the no noise and 1% noise case are 0.0835S/m and 0.0807S/m respectively, 3.3% different. Adding 1% noise seems not to be affecting the conductivity readings significantly in the liver region. We can see this is obvious not the case of spinal cord, visually the noise added reconstruction image shows a significant different color on the same scale. The fact that liver's effective conductivity has not changed significantly could be due to the large area of the organ.

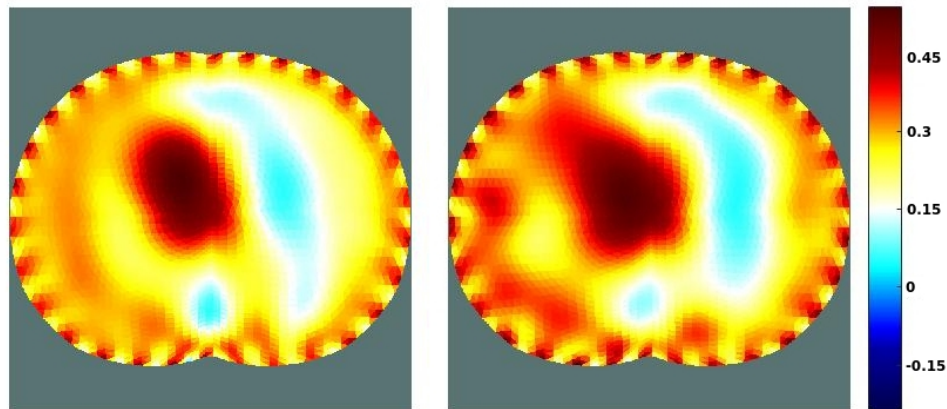


Fig 7.3.4: Left: FEM model used to generate voltage data. Right: Reconstructed image with 1% added random noise. (a) no noise added. conductivity in liver region is 0.0835S/m (b) 1% noise added, conductivity in liver region is 0.0807S/m.

Now we show the effect of geometry mismatch on the reconstructed image. Fig. 6.3.5(b) shows that a “ghost” region appears when using a non-matching geometry (circular shape) to image the thorax geometry. Since in a real human thorax the conductivity distribution is much more complex due to multiple organs being present. It would be difficult to differentiate whether an image region is a ghost or a real organ. Hence we conclude that accurate geometry is needed in order to accurately image the organs.

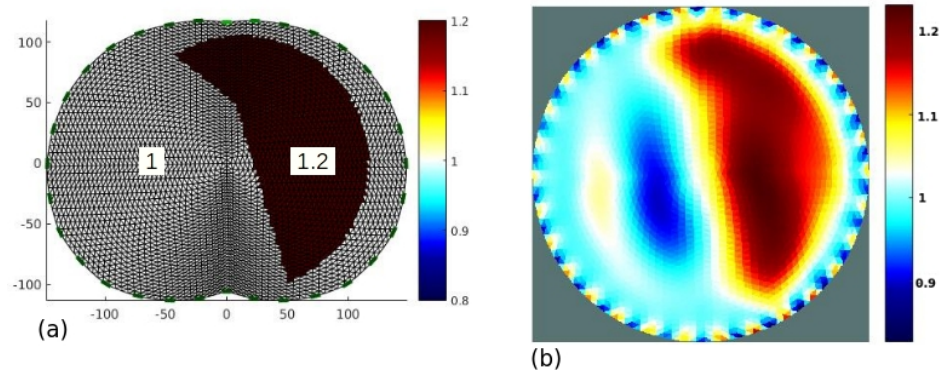


Fig. 7.3.5: Left: FEM model (b) reconstructed image with inaccurate thorax geometry

We now build an FEM model based on the realistic CT scan cross-sectional anatomy to study in more rigor the conductivity accuracy we can resolve by employing a prior information. Fig. 7.3.6 shows the CT scan and FEM model.

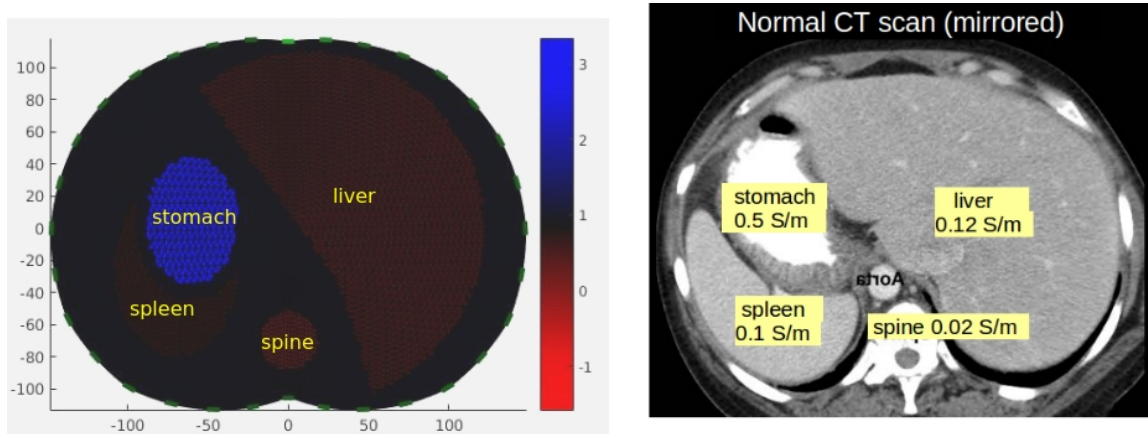


Fig. 7.3.6: Left: FEM model used for simulation study based on the CT scan. Right: CT scan image (mirrored).

We can utilize the a priori information about the location of the liver and the fact that the conductivity of the tissue is approximated to be uniform. Hence we employ such information in the regularization matrix, shown in Equation 7.3.1. Then we solve the Tikhonov regularization based on minimizing 7.3.2.

Fig. 7.3.7(c) shows the reconstruction result of the such smoothness constrained case. We can see that compared to Fig. 7.3.7(b) we are much closer in terms of the conductivity estimate. In practice it is difficult to obtain the exact shape and location of the liver in the human body, which requires CT or MRI scan. Fig. 7.3.7(d) shows such smoothness constrain applied to an imperfect region, as an estimated liver location. The conductivity estimate in such a case has a negligible 0.3% difference. We can conclude that such smoothness constrain scheme will work well on estimated liver region without accurate knowledge of the shape and location of the liver.

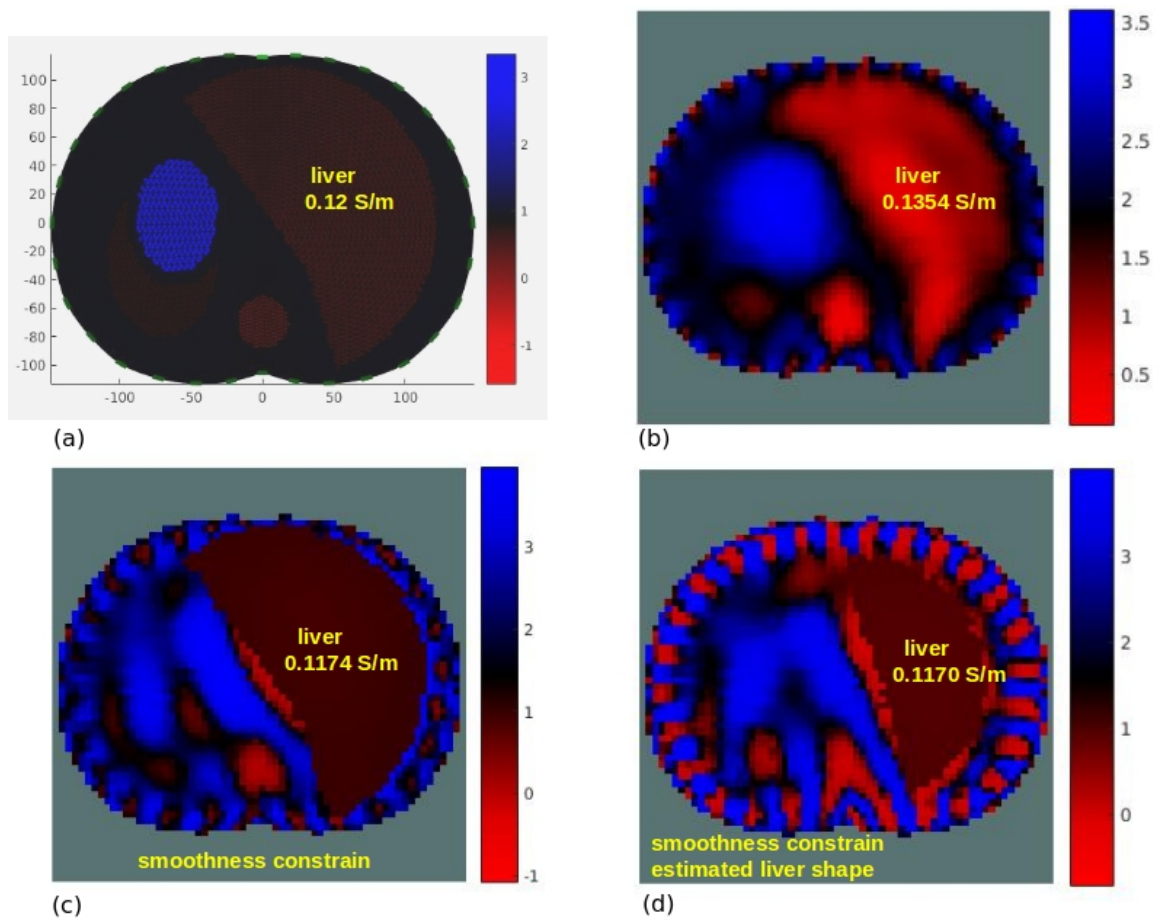


Fig. 7.3.7: (a) FEM model to generate voltage data (b) unconstrained higher order solver (c) smoothness constrain with a priori matrix in the liver region (d) smoothness constrain with a priori matrix in the liver region with shape error.

7.4 Phantom experiments

In this section the results of phantom experiment in saline tank is presented. The experimental setup is shown in Fig. 7.4.1(left). A saline tank (6 inches in diameter) is drilled 32 equal spacing holes, and stainless steel electrodes are placed through the each

hole flush to the tank inner surface. The diameter of each electrode is 3mm. The tank is filled with saline with conductivity of 1.5 S/m. An agar gel is casted with NaCl added to create a uniform conductivity of 0.3 S/m.

Fig. 7.4.1(b) shows the reconstructed image using difference method. The frequency of the injection current is 250Khz. We can see that both the shape has been resolved to a good degree. Since the image is from difference data of saline and saline with agar gel. To show the correct conductivity of the agar gel, the scale bar readings has been added by 1.5 S/m, the background conductivity.

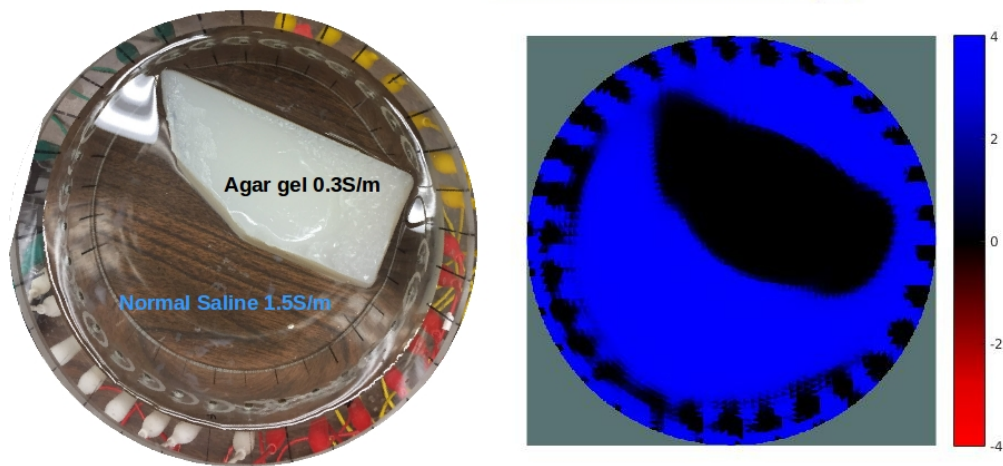


Fig. 7.4.1: Left: tank setup with 32 stainless steel electrodes. Saline background with 1.5S/m conductivity and agar gel object with 0.3S/m conductivity. Right: Reconstructed image with difference data at 250Khz. The scale bar readings are added by 1.5 S/m.

Removing the electrode effect

In the reconstructed image in Fig. 7.4.1 we see “ghost” images around the electrodes. This is due to the non-perfect modeling of electric field potential in the forward problem. We can see that from the sensitivity map in Fig. 7.4.2. [83-86] that around the current injecting electrodes are elements among the most sensitive region, this is understood because of the high current density in such region. Hence errors in modeling in this region become magnified easily to become the “ghost” images. One prominent error in the FEM model and in the tank is contact impedance. We can see in Fig. 7.4.3 [87,88] that contact impedance at the interface of the electrode and the body changes the current flow around the electrode. To be more specific lack of contact impedance (or a very low value) creates singularities in the electric field at the electrode edge hence creates high current density. Forward modeling errors in this highly sensitive region will reconstruct to ghosts consequently. In order to mitigate this problem we need to incorporate reasonable valued contact impedance into the complete electrode model.

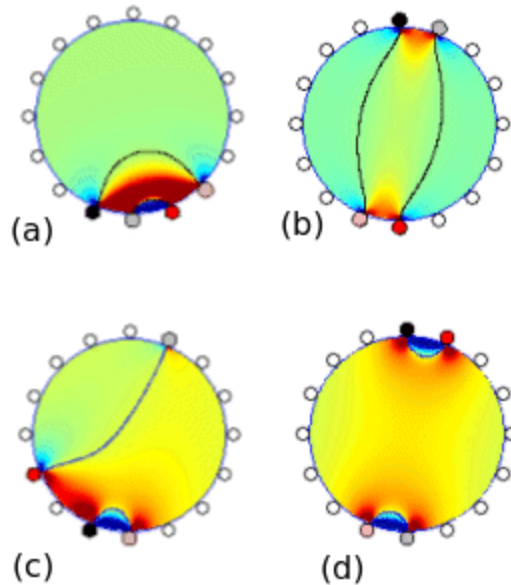


Fig. 7.4.2. (a)(b)sensitivity field of adjacent injection pattern (c)(d) sensitivity field of opposite injection pattern [89]

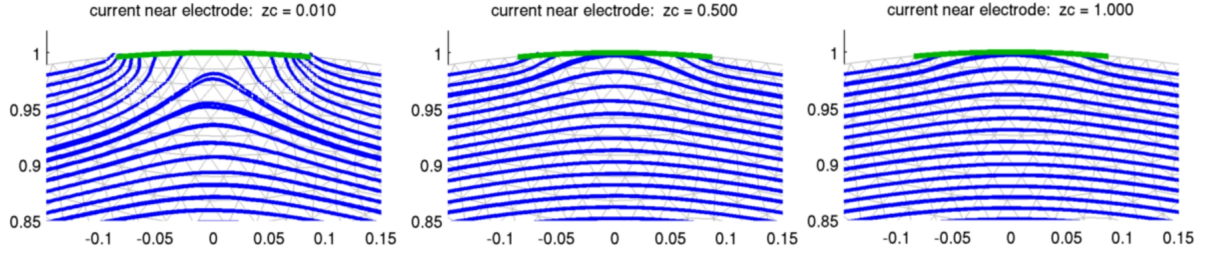


Fig. 7.4.3 current lines near electrode with different contact impedance values from $z=0.01$ Ohm to $z = 10$ Ohm.

In order to calculate each electrode's contact impedance, we use the total impedance between injection pair measured during experiment. If we assume the resistance of saline between each electrode pair is the same then we can formulate a linear system of equations and solve 7.4.1:

$$\min_x \frac{1}{2} \|C \cdot x - d\|_2^2 \quad 7.4.1$$

where $x = [x_1, x_2, \dots, x_{33}]^T$ contains the individual contact impedance and x_{33} is the resistance of saline, and $d = [d_1, d_2, \dots, d_{32}]^T$ contains the 32 measured impedance, and:

$$C = \begin{bmatrix} 1 & 0 & 0 & 0 & 0 & 1 & 0 & 0 & \dots & 1 \\ 0 & 1 & 0 & 0 & 0 & 0 & 1 & 0 & \dots & 1 \\ \cdot & \dots & 1 \\ \cdot & \dots & 1 \\ \cdot & \dots & 1 \\ 0 & 0 & 0 & 0 & 1 & 0 & 0 & \dots & 1 & 1 \end{bmatrix}$$

Fig. 7.4.4 (bottom) shows the calculation result of the individual electrode contact impedance. To get point-wise impedance we divide each contact impedance by the electrode surface area. Fig. 7.4.5 shows the result of the reconstructed image with calculated contact impedance modeled in.

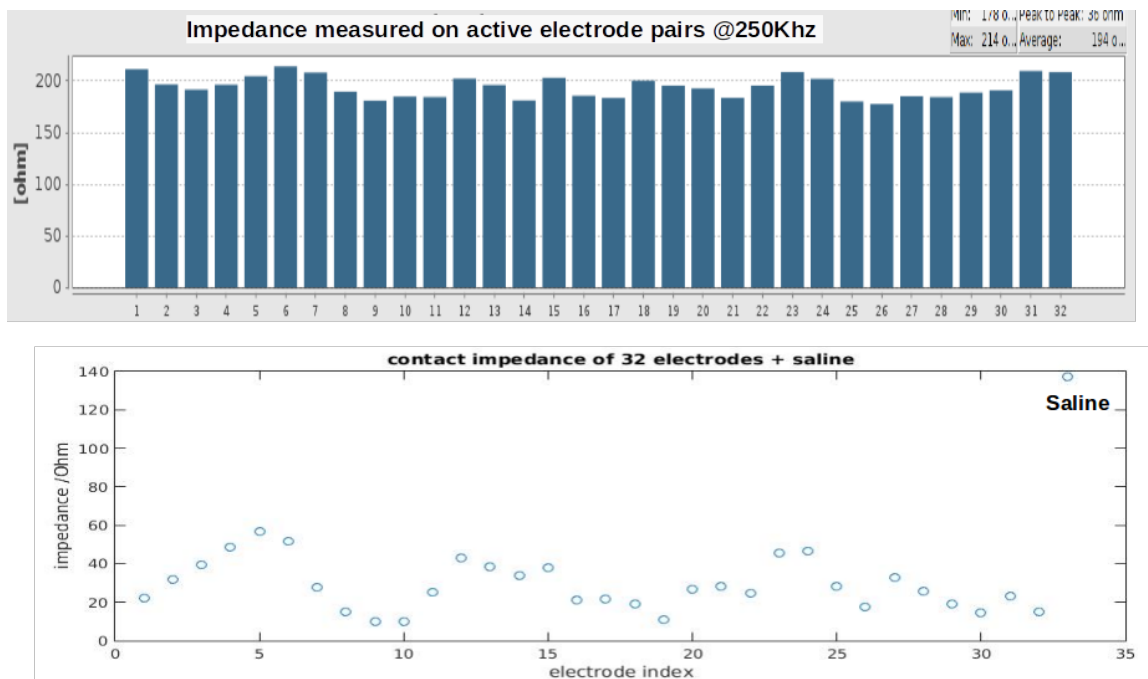


Fig. 7.4.4: Top: electrode pair contact impedance in series with saline. Bottom: Calculated contact impedance for each electrode. The last impedance is the resistance of saline.

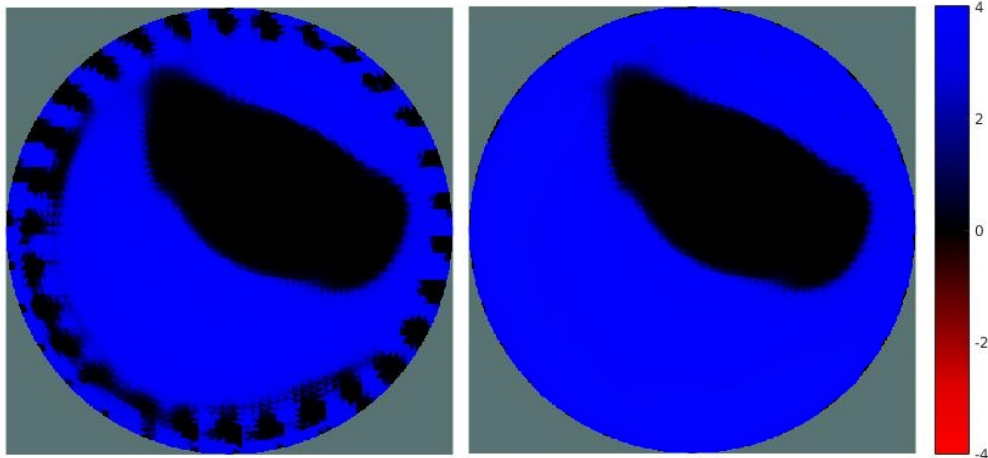


Fig. 7.4.5: Left: reconstructed image with no contact impedance. Right: reconstructed image with calculated contact impedance incorporated.

Absolute Imaging

It is also possible to reconstruct “absolute” conductivities with one set of measurement data. By replacing the reference tank data used in difference imaging and calculate the reference data numerically, we are able to reconstruct images with correct conductivity levels. Figure 6.4.6. - 6.4.6. shows the results of absolute imaging with comparison to difference imaging. The conductivities used in the agar gel is $1/8$ of normal saline (0.19S/m) and the background is $1/4$ of normal saline (0.38S/m).



Fig. 6.4.4: phantom tank with $1/8$ normal saline conductivity agar gel and $1/4$ normal saline background.

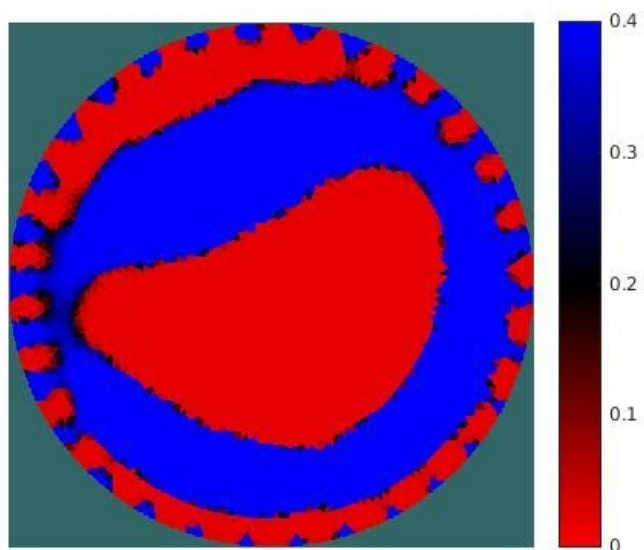


Fig. 6.4.5: Difference imaging

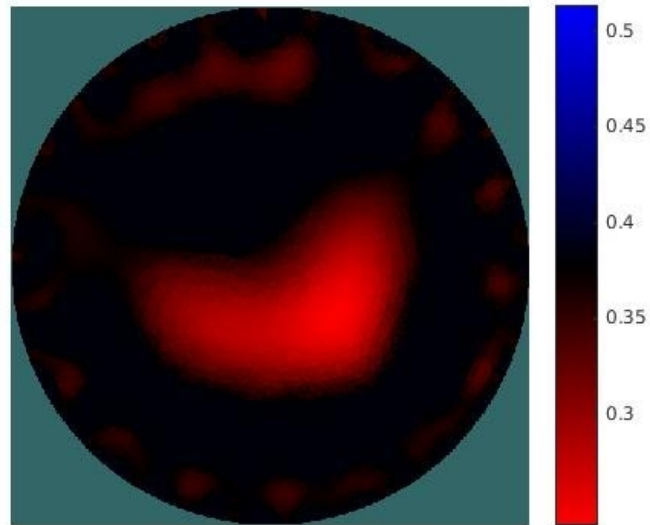


Fig. 6.4.6: Absolute imaging. The scale bar shows correct conductivity reading.

7.5 Ex-vivo experiment

In this section two experiments are conducted, first one is with pork fat to mimic the subcutaneous fatty tissue, the second experiment is with pork liver. We use difference imaging at 50Khz for both experiment, and higher order forward and inverse solver discussed in Chapter 3.

Pork liver is purchased from xxx and fat is purchased from local supermarket. Electrical Impedance Spectroscopy is performed on liver, fat and saline as shown in Fig. 7.5.1. Since the EIS is performed with two electrode method, we need to consider the equivalent circuit to be the tissue in series with two electrode contact impedance. Under

low frequencies the contact impedance dominates the tissue impedance and hence the curve shows a roughly 20dB/decade downward slope (can be roughly estimated as a capacitor). We can see that above 1KHz the impedance roll-off due to contact impedance has reduced to a negligible level and the impedance reflect the tissue property from here on. We can see that fat has a much higher impedance in general, about 2x that of liver. Saline with 0.37 S/m conductivity is also measured and is shown as the blue curve. Since the geometry of the EIS measurement is the same we can estimate the liver and fat conductivities to be proportional to the impedance modulus reading to saline. Such conductivity estimates are used to verify reconstruction results.

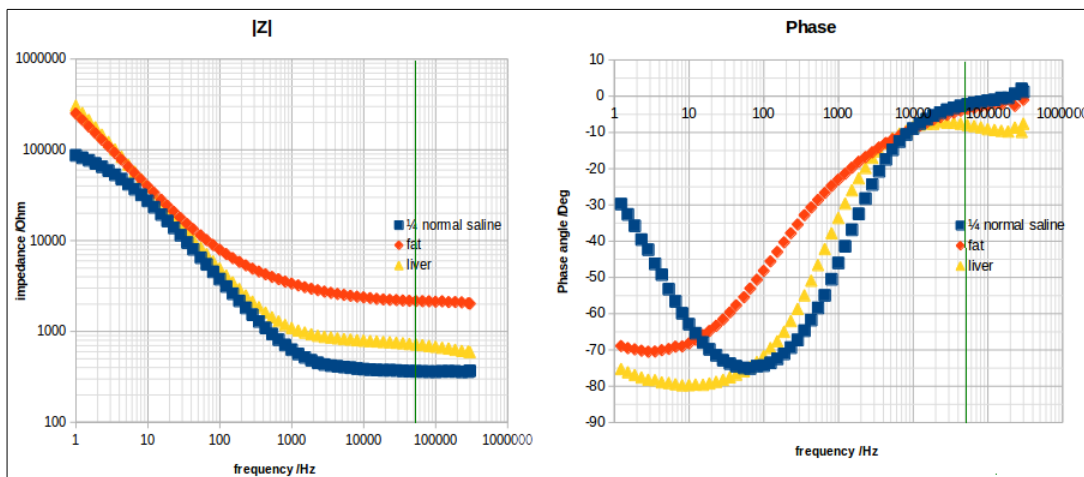


Fig. 7.5.1: Impedance modulus (left) and phase angle (right) EIS with two electrode method.

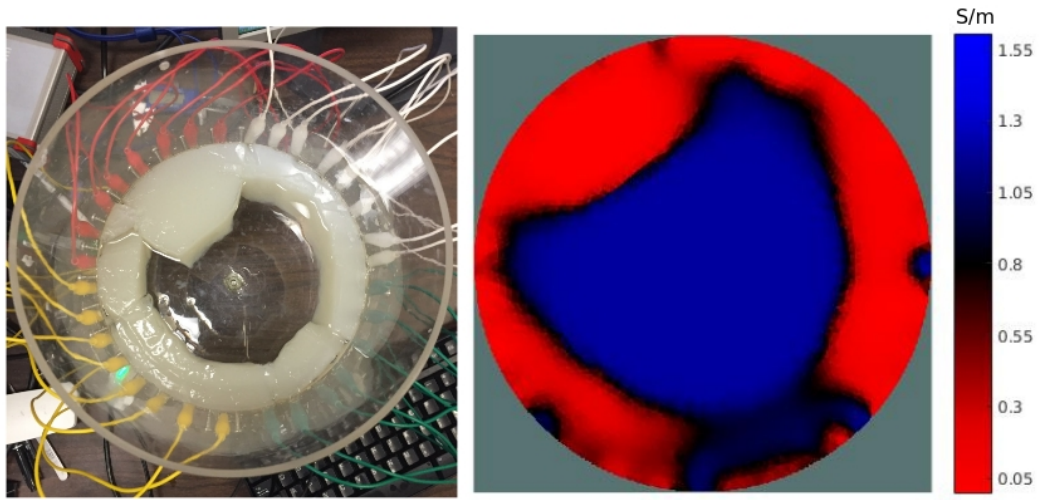


Fig. 7.5.2 and Fig. 7.5.3 show the experimental setups and reconstruction results of the fat and liver experiment respectively. We can see good shape correlation as well as conductivity estimation in both cases.

Fig. 7.5.2: Agar gel mimicing subcutaneous fat in saline. Left: experimental setup. Right: Reconstructed image.

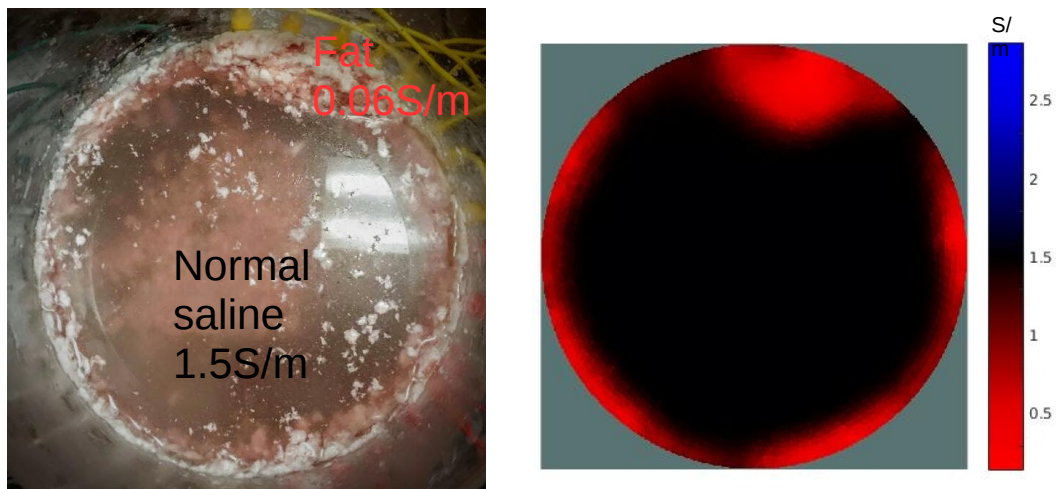


Fig. 7.5.3: Subcutaneous fat experiment with pork fat in saline. Left: experimental setup. Right: Reconstructed image.

Fig. 7.5.2 and Fig. 7.5.3 show the experimental setups and reconstruction results of the fat and liver experiment respectively. We can see good shape correlation as well as conductivity estimation in both cases.

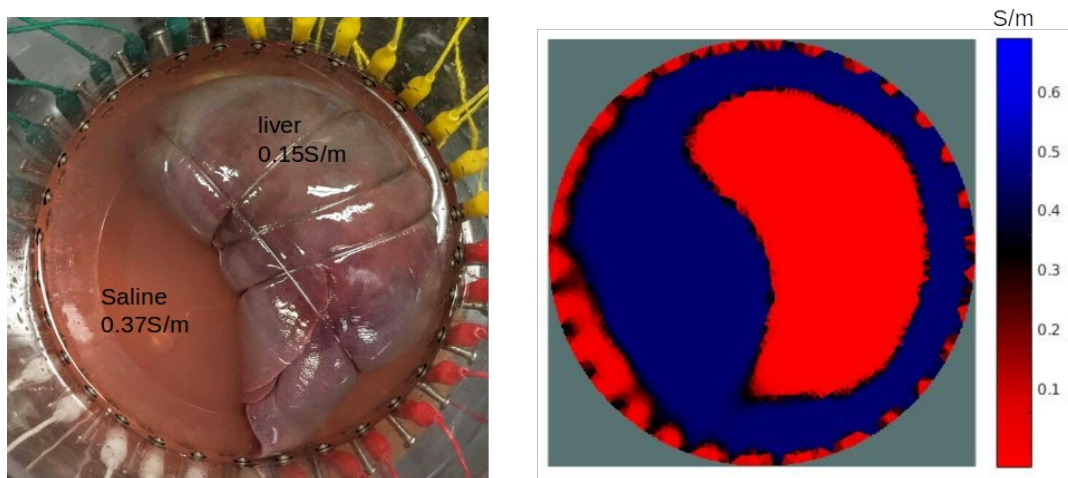


Fig. 7.5.4: Liver experiment with pork liver. Left: experimental setup. Right: Reconstructed image.

7.6 Human experiments

In this section we show some preliminary results of human experiments. The electrode setup is described in detail at the beginning of this chapter. Fig. 7.6.1 shows the electrode numbering, electrode No. 1 is in the front of the test person, then the numbering increases in clock-wise fashion looking down onto the belt. Electrode 16 is in the back center close to the spinal cord.

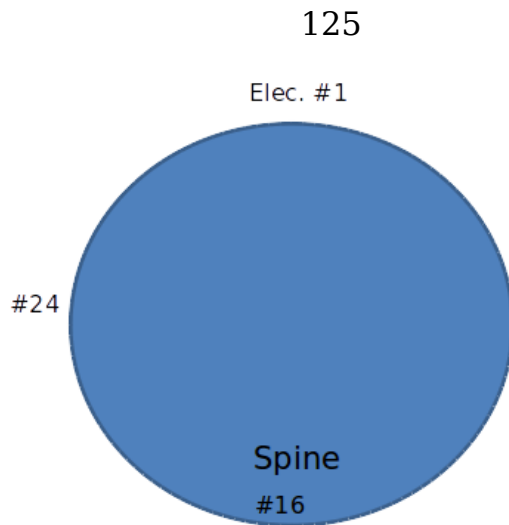


Fig. 7.6.1: Electrode numbering on test person.

First we will attempt to reconstruct the subcutaneous fat. The difference data are taken from two different levels on the body as shown in Fig. 7.6.2 (left). The top arrow points to the reference level and the bottom arrow points to a fattier level. By subtracting data from these two levels we attempt to reconstruct the difference in subcutaneous fat. It is worth mentioning that the current injection pattern employed here is skip 1. This current pattern has high sensitivity fields on the edge of the tank compared to in the center.

The electrodes used are ECG type Ag/AgCl electrodes. As explained in Chapter 2 such electrodes are non-polarizing and can be seen as purely resistive, hence such electrodes are suitable for Multi-frequency usage. However, we still see “ghost” near electrodes after putting in calculated contact impedance. Here the ghosts are most likely caused by the mismatch of the belt placement in upper and lower levels. Further study is needed for a confident conclusion.

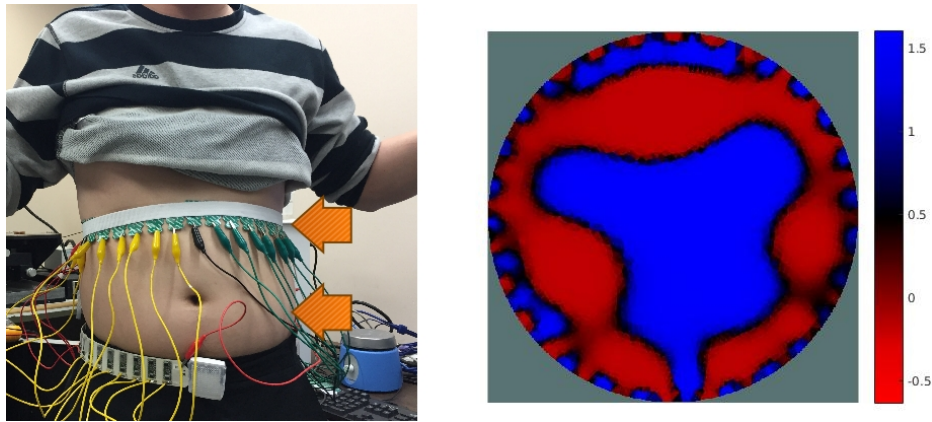


Fig. 7.6.2: Left: experiment setup. Right: Reconstructed image with location difference data.

Fig. 7.6.3 shows the result of thorax imaging of two males. The images are reconstructed with Multi-frequency difference data taken at 1Khz and 100Khz. The estimated organ regions are highlighted on the images, although the truthfulness of such estimate needs to be validated by high resolution imaging modalities such as CT or MRI scan.

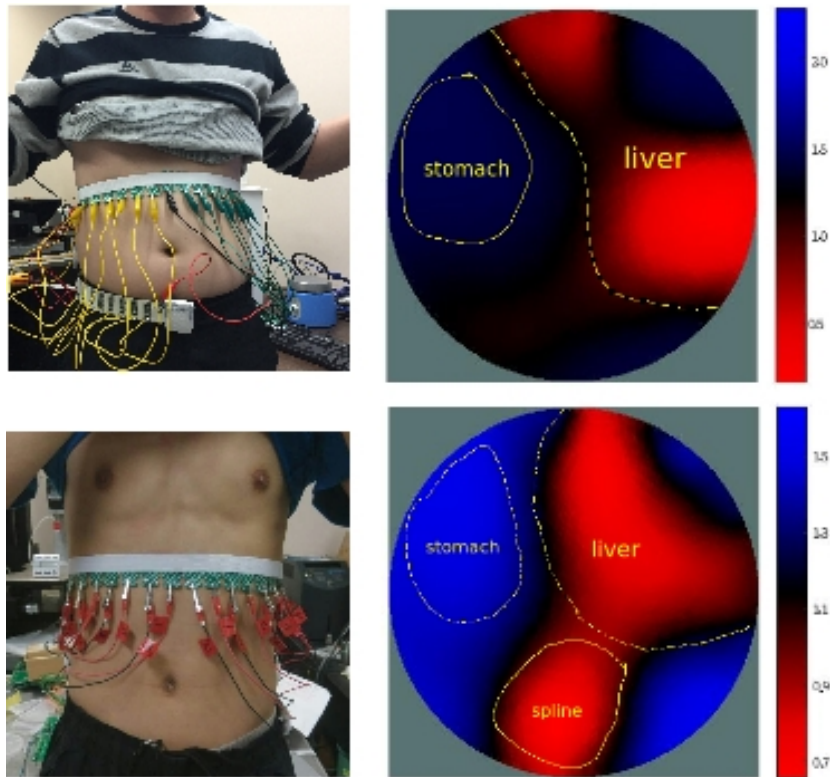


Fig. 7.6.3: Left: two male test subjects with electrode belt position shown. Right: Reconstructed images correspondingly.

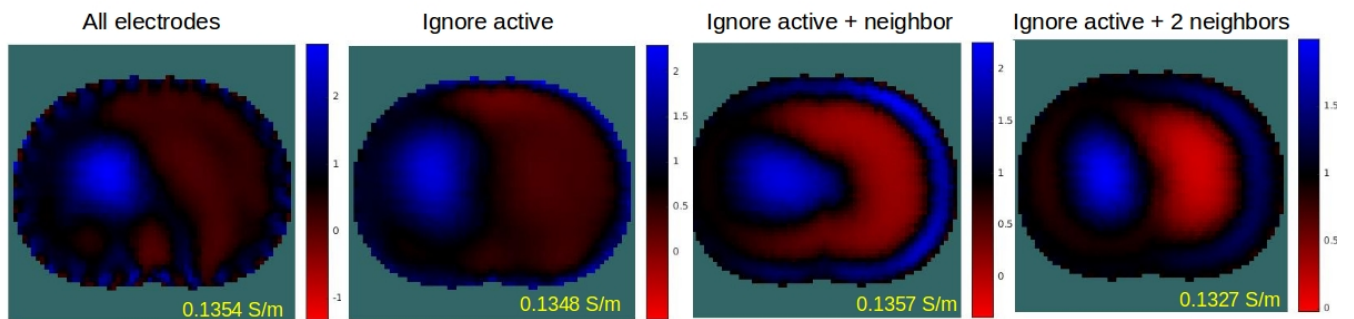


Fig. 7.6.4: Reconstructed images with conductivity readings from simulation study ignoring different neighboring electrodes.

CONCLUSIONS

Despite advances in diagnosis and therapy, atherosclerotic cardiovascular disease remains the leading cause of morbidity and mortality. Predicting metabolically active atherosclerotic lesions has remained an unmet clinical need. Specially, atherosclerotic plaques that are prone to rupture are of extremely high-risk and can cause detrimental heart attacks and/or strokes, leading to sudden death. It has been shown that atherosclerosis is correlated to the level of obesity of an individual [90-93] Usually in clinical practice, the doctor will assess a patient's "risk factor" based on his or her Body Mass Index (BMS), and measurement of the waist circumference. Meanwhile the level of fatty droplet deposits in the liver is an important bio-marker to assess the patient's risk factor, however the patient will need to undergo radiation imaging such as CT scan or MRI scan.

For the vulnerable plaques that can lead to sudden rupture, the ability to distinguish them at an early stage remains largely lacking. Therefore it is of great clinical interest to find improved diagnostic techniques to identify and localize such vulnerable plaques. Meanwhile, lipid has significantly lower electrical impedance than the rest of the vessel tissues in certain frequency bands [2][94]. In this thesis we explored spectroscopic and tomographic methods to characterize such plaques. In addition, with the Electrical

Impedance Tomography method we will propose a novel method to detect fatty liver in an early stage with non-radiating and non-invasive manner.

We have known in the previous chapters that electrical impedance spectroscopy and electrical impedance tomography can be used to assess the risks of vulnerable plaque rupture and obesity related diseases indicated by fatty liver. We have known in this thesis that Electrical Impedance Spectroscopy together with Electrical Impedance Tomography have great potential in accurate assessment of patient risks associated with obesity and heart related diseases.

BIBLIOGRAPHY

- [1] Alpert MA, Hashimi MW. Obesity and the heart. *Am J Med Sci.* 1993;306:117-123.
- [2] Packard, Rene., Zhang, Xiaoxiao., Luo, Yuan., et al., "The next generation of stretchable sensors for intravascular electrochemical impedance spectroscopy of varying levels of lipid burden and atherosclerosis," American Heart Association (AHA) Health Tech, Session Title" Emerging Technologies (November 2015), vol. 132 no. Suppl 3 A18004. doi:10.1016/j.bios.2013.11.059
- [3] Henderson RP, Webster JG, "An impedance camera for spatially specific measurements of the thorax", *IEEE Trans Biomed Eng.*, 1978, 25(3):250-4.
- [4] Cole KS, Curtis HJ, "ELECTRIC IMPEDANCE OF THE SQUID GIANT AXON DURING ACTIVITY," *Gen Physiol.* 1939 May 20; 22(5):649-70.
- [5] Weinhold C, Reichenspurner H, et al., "Registration of thoracic electrical bioimpedance for early diagnosis of rejection after heart transplantation," *J. Heart Lung Transplant*, 1993 Sept-Oct; 12(5):832-6
- [6] Muller JE, Tofler GH, Stone PH. "Circadian variation and triggers of onset of acute cardiovascular disease.," *Circadian variation and triggers of onset of acute cardiovascular disease. Circulation.* 1989; 79: 733–743.

- [7] Moreno PR, Bernardi VH, et al. "Macrophages, smooth muscle cells, and tissue factor in unstable angina: implications for cell-mediated thrombogenicity in acute coronary syndromes," *Circulation*. 1996; 94: 3090–3097.
- [8] DeMaria AN, Narula J, Mahmud E, Tsimikas S. "Imaging vulnerable plaque by ultrasound." *J Am Coll Cardiol* 2006;47:C32–9.
- [9] Di Mario C, The SH, Madretsma S, et al. "Detection and characterization of vascular lesions by intravascular ultrasound: an in vitro study correlated with histology." *J Am Soc Echocardiogr* 1992;5:135– 46.
- [10] Toussaint JF, Southern JF, Fuster V, Kantor HL. "Water diffusion properties of human atherosclerosis and thrombosis measured by pulse field gradient nuclear magnetic resonance." *Arterioscler Thromb Vasc Biol* 1997;17:542– 6.
- [11] Caplan JD, Waxman S, Nesto RW, Muller JE. "Near-infrared spectroscopy for the detection of vulnerable coronary artery plaques." *J Am Coll Cardiol* 2006;47:C92– 6.
- [12] Madjid M, Willerson JT, Casscells SW. Intracoronary thermography for detection of high-risk vulnerable plaques. *J Am Coll Cardiol* 2006;47:C80 –5.
- [13] Casscells W, Hathorn B, David M, et al. Thermal detection of cellular infiltrates in livingtherosclerotic plaques: possible implications for plaque rupture and thrombosis. *Lancet* 1996;347:1447–51.

- [14] Verheye S, De Meyer GR, Van Langenhove G, Knaapen MW, Kockx MM. In vivo temperature heterogeneity of atherosclerotic plaques is determined by plaque composition. *Circulation* 2002;105: 1596 – 601.
- [15] Krams R, Verheye S, van Damme LC, et al. In vivo temperature heterogeneity is associated with plaque regions of increased MMP-9 activity. *Eur Heart J* 2005;26:2200 –5.
- [16] Rzeszutko L, Legutko J, Kaluza GL, et al. Assessment of culprit plaque temperature by intracoronary thermography appears inconclusive in patients with acute coronary syndromes. *Arterioscler Thromb Vasc Biol* 2006;26:1889–94.
- [17] Briain D. MacNeill, et al., "Intravascular Modalities for Detection of Vulnerable Plaque," *J. AHA., Arteriosclerosis, Thrombosis, and Vascular Biology*, 2003 August. 1079-5642.
- [18] Falk E, Shah PK, Fuster V. Coronary plaque disruption. *Circulation* 1995;92:657–71.
- [19] Raggi P, Gongora MC, Gopal A, Callister TQ, Budoff M, Shaw LJ. Coronary artery calcium to predict all-cause mortality in elderly men and women. *J Am Coll Cardiol* 2008;52:17–23.

- [20] Ridker PM, Paynter N, Rifai N, Gaziano JM, Cook NR. C-reactive protein and parental history improve global cardiovascular risk prediction: the Reynolds risk score for men. *Circulation* 2008;118: 2243–51.
- [21] Falk E. Pathogenesis of atherosclerosis. *J Am Coll Cardiol* 2006;47: C7–12.
- [22] Kazuhiro Osawa, Toru Miyoshi, et al., "Nonalcoholic Hepatic Steatosis Is a Strong Predictor of High-Risk Coronary-Artery Plaques as Determined by Multidetector CT," *PLoS One*, 2015; 10(6): e0131138.
- [23] Hansson GK. Inflammation, atherosclerosis and coronary artery disease. *N Engl J Med* 2005;352:1685–95.
- [24] Bjorkbacka H, Kunjathoor VV, Moore KJ, et al. Reduced atherosclerosis in MyD88-null mice links elevated serum cholesterol levels to activation of innate immunity signaling pathways. *Nat Med* 2004;10:416 –21.
- [25] Littlewood TD, Bennett MR. Apoptotic cell death in atherosclerosis. *Curr Opin Lipidol* 2003;14:469 –75.
- [26] Jones CB, Sane DC, Herrington DM. Matrix metalloproteinases: a review of their structure and role in acute coronary syndrome. *Cardiovasc Res* 2003;59:812–23.

- [27] Virmani R, Kolodgie FD, Burke AP, Farb A, Schwartz SM. Lessons from sudden coronary death: a comprehensive morphological classification scheme for atherosclerotic lesions. *Arterioscler Thromb Vasc Biol* 2000;20:1262–75.
- [28] DeMaria AN, Narula J, Mahmud E, Tsimikas S. Imaging vulnerable plaque by ultrasound. *J Am Coll Cardiol* 2006;47:C32–9.
- [29] Di Mario C, The SH, Madretsma S, et al. Detection and characterization of vascular lesions by intravascular ultrasound: an in vitro study correlated with histology. *J Am Soc Echocardiogr* 1992;5:135– 46.
- [30] Baquis GD, Brown WF, Capell JT, et al. Technology review: The Neurometer Current Perception Threshold (CPT) Muscle and Nerve.;22(4):523–531.
- [31] Valentinuzzi ME, "Bioelectrical impedance techniques in medicine." *Crit Rev Biomed eng.* 1996;24(4-6):223-55.
- [32] Katchalsky, and Curran, "Nonequilibrium Thermodynamics in Biophysics." Book, 1965.
- [33] David E. Goldman. POTENTIAL, IMPEDANCE, AND RECTIFICATION IN MEMBRANES. *J Gen Physiol.* 1943 Sep 20; 27(1): 37–60. PMID: PMC2142582.

- [34] A.L. Hodgkin and B. Katz, The effect of sodium ions on the electrical activity of the giant axon of the squid. *J. Physiol.* 1949;108;37-77.
- [35] Miller WT, Geselowitz DB. "Simulation studies of the electrocardiogram. I. The normal heart. " *Circ Res.* 1978 Aug;43(2):301-15.
- [36] Herman P. Schwan and Harold J. Morowitz, "Electrical Properties of the Membranes of the Pleuropneumonia-Like Organism," *Biophysical Journal.* Vol. 2. Issue 5. 1962, pp 395-407.
- [37] Andre Vorst, Arye Rosen, Youji Kotsuka, *RF Microwave Interaction with Biological Tissues*, Wiley Series in Microwave and Optical Engineering, Honoken NJ, 2006.
- [38] Pethig R, Kell DB. The passive electrical properties of biological systems: their significance in physiology, biophysics and biotechnology. *Phys Med Biol.* 1987 Aug; 32(8):933-70.
- [39] Tom Timdswell, Adam Gibson, Richard Bayford, and David Holder, "Three-Dimensional Electrical Impedance Tomography of Human Brain Activity". *NeuroImage J.* 2001, pp: 283-294.
- [40] R. M., Geselowitz, D. B., Briller, S.A., and Trost, R. F., Quadrupole components of the human surface electrocardiogram, *Am. Heart J.*, 83,663, 1972.

- [41] Nicholas Polydorides, "Image reconstruction algorithms for soft-field tomography," University of Manchester Institute of Science and Technology, 2002, Ph.D. thesis.
- [42] Stern, O., Z. Elektrochem., 30, 508 (1924)
- [43] H. Helmholtz (1853), "Ueber einige Gesetze der Vertheilung elektrischer Ströme in körperlichen Leitern mit Anwendung auf die thierisch-elektrischen Versuche" (in German), Annalen der Physik und Chemie 165 (6): pp. 211–233
- [44] Esin and Markov, Acta Physicochim. 10, 353 (1939). 62.
- [45] Randles, J. E. B. (1947). "Kinetics of rapid electrode reactions". Discussions of the Faraday Society. 1: 11.
- [46] Brewer PJ, Brown RJ. "Effect of Structural Design of Silver/Silver Chloride Electrodes on Stability and Response Time and the Implications for Improved Accuracy in pH Measurement." Sensors. 2009;9(1):118-30.
- [47] Kochowski, S; K. Nitsch (21 May 2002). "Description of the frequency behaviour of metal-SiO₂-GaAs structure characteristics by electrical equivalent circuit with constant phase element" (PDF). Thin Solid Films. 415: 133–137.
- [48] oke. M., Electrical imaging surveys for environmental and engineering studies. 2000.

- [49] Krautblatter, M. and C. Hauck, Electrical resistivity tomography monitoring of permafrost in solid rock walls. *Journal of Geophysical Research*, 2007. 112(F2).
- [50] Bolton, G.T., et al., Development of an electrical tomography system for operation in a remote, acidic and radioactive environment. *Chemical Engineering Journal*, 2007. 130 (2–3): p. 165-169.
- [51] Johnson, T.J., "Analysis of dynamic transmissibility as a feature for structural damage detection". 2002, Purdue University.
- [52] Günther, T., C. Rücker, and K. Spitzer, Three-dimensional modelling and inversion of dc resistivity data incorporating topography - II. Inversion. *Geophysical Journal International*, 2006. 166(2): p. 506-517.
- [53] S. Heinrich, H. Schiffmann, A. Frerichs, A. Klockgether-Radke, I. Frerichs, Body and head position effects on regional lung ventilation in infants: an electrical impedance tomography study. *Intensive Care Med.*, 32:1392–1398, 2006.
- [54] Adler A., Amato M.B., Arnold J.H., Bayford R., Bodenstein M., Böhm S.H., Brown B.H., Frerichs I., Stenqvist O., Weiler N., Wolf G.K. (2012) "Whither lung EIT: where are we, where do we want to go and what do we need to get there?" *Physiol. Meas.* 33(5):679–94.

- [55] Wi H, Sohal H, McEwan AL, Woo EJ, Oh TI. Multi-frequency electrical impedance tomography system with automatic self-calibration for long-term monitoring. *IEEE Trans. Biomed. Circuits Syst.* 2014;8(1):119-128.
- [56] Kuen J, Woo EJ, Seo JK. Multi-frequency time-difference complex conductivity imaging of canine and human lungs using the KHU Mark1 EIT system. *Physiol. Meas.* 2009;30(6):S149-S164.
- [57] Ahn S, Oh TI, Jun SC, Seo JK, Woo EJ. Validation of weighted frequency-difference EIT using a three-dimensional hemisphere model and phantom. *Physiol. Meas.* 2011;32(10):1663–1680.
- [58] Calderón A.P. (1980) "On an inverse boundary value problem", in Seminar on Numerical Analysis and its Applications to Continuum Physics, Rio de Janeiro.
- [59] Cheney M., Isaacson D. and Newell J. C. (1999) "Electrical impedance tomography". *"SIAM review"* 41(1): 85–101.
- [60] *Electrical Impedance Tomography: Methods, History and Applications*, Institute of Physics, 2004. ISBN 0-7503-0952-0.
- [61] Mueller J L and Siltanen S (2012), *Linear and Nonlinear Inverse Problems with Practical Applications*. SIAM.

- [62] Lionheart W.R.B. (2004) "EIT reconstruction algorithms: pitfalls, challenges and recent developments" (Review Article). *Physiol. Meas.* 25: 125–143.
- [63] O.P. Ferreira, et al. Local convergence analysis of Gauss-Newton method under a majorant condition. *Journal of Complexity*, vol 27, issue 1, 2011, pp 111-125.
- [64] J.P. Dedieu, M.H. Kim. Newton's method for analytic systems of equations with constant rank derivatives *J. Complexity*, 18 (1) (2002), pp. 187–209
- [65] J.P. Dedieu, M. Shub Newton's method for overdetermined systems of equations *Math. Comp.*, 69 (231) (2000), pp. 1099–1115
- [66] L. Borcea. Electrical Impedance Tomography: Topical Review. *Inverse Problems* 18 (2002) R99-R136. Institute of Physics Publishing.
- [67] Andy Adler, William Lionheart. Uses and abuses of EIDORS: an extensible software based for EIT. *Physiological Measurement*. 2006;27(5).
- [68] Packard, Rene., Zhang, Xiaoxiao., Luo, Yuan., et al., "The next generation of stretchable sensors for intravascular electrochemical impedance spectroscopy of varying levels of lipid burden and atherosclerosis," American Heart Association (AHA) Health Tech, Session Title" Emerging Technologies (November 2015), vol. 132 no. Suppl 3 A18004.

- [69] D. Kang, A. Stanley, J. H. Chang, Y. Liu, and Y.-C. Tai, "Effects of deposition temperature on Parylene-C properties," in *Micro Electro Mechanical Systems*
- [70] Y. Lei, Y. Liu, W. Wang, W. Wu, and Z. Li, "Studies on Parylene C-caulked PDMS (pcPDMS) for low permeability required microfluidics applications," *Lab on a Chip*, vol. 11, pp. 1385-1388, 2011 2011.
- [71] J. H. C. Chang, L. Yang, K. Dong yang, and T. Yu-Chong, "Reliable packaging for parylene-based flexible retinal implant," in *Solid-State Sensors, Actuators and Microsystems (TRANSDUCERS & EUROSENSORS XXVII)*, 2013 Transducers & Eurosensors XXVII: The 17th International Conference on, 2013, pp. 2612-2615.
- [72] J. M. Hsu, L. Rieth, S. Kammer, M. Orthner, and F. Solzbacher, "Effect of thermal and deposition processes on surface morphology, crystallinity, and adhesion of Parylene-C," *Sensors and Materials*, vol. 20, pp. 87-102, 2008.
- [73] H.E. Ayliffe and A.B. Frazier, "Electric impedance spectroscopy using microchannels with integrated metal electrodes", *Journal of Microelectromechanical Systems*, vol. 8, pp. 1, 1999.

- [74] C. Gabriel, S. Gabriely and E Corthout, "The dielectric properties of biological tissues: I. Literature survey", *Physics in Medicine and Biology*, vol. 41, pp. 2231, 1996.
- [75] M.J. Hayat, N. Howlader, M.E. Reichman and B.K. Edwards, "Cancer statistics trends and multiple primary cancer analyses from the Surveillance Epidemiology and End Results (SEER) program", *Oncologist*, vol. 12, pp. 20, 2007.
- [76] Fei Yang, Robert Patterson, A novel impedance-based tomography approach for stenotic plaque detection: A simulation study, *International Journal of cardiology* 144(2):279-83.
- [77] Bastian Harrach, Marcel Ullrich, Resolution Guarantees in Electrical Impedance Tomography, *IEEE Transactions on Medical Imaging*, vol. 34, Issue 7. 2015.
- [78] D. Barber and B. Brown, "Applied potential tomography", *J. Phys. E Sci. Instrum.*, vol. 17, no. 9, pp. 723-733, 1984.
- [79] A. Wexler, B. Fry and M. Neuman, "Impedance-computed tomography algorithm and system", *Appl. Opt.*, vol. 24, no. 23, pp. 3985-3992, 1985.
- [80] J. Newell, D. G. Gisser and D. Isaacson, "An electric current tomograph", *IEEE Trans. Biomed. Eng.*, vol. 35, no. 10, pp. 828-833, Oct. 1988.

- [81] P. Metherall, D. Barber, R. Smallwood and B. Brown, "Three dimensional electrical impedance tomography", *Nature*, vol. 380, no. 6574, pp. 509-512, 1996.
- [82] D. Gisser, D. Isaacson and J. Newell, "Electric current computed tomography and eigenvalues", *SIAM J. Appl. Math.*, vol. 50, no. 6, pp. 1623-1634, 1990.
- [83] P. Kauppinen, J. Hyttinen, J. Malmivuo, Sensitivity Distribution Simulations of Impedance Tomography Electrode Combinations, *IJBEM*, Vol. 7, No. 1, 2005.
- [84] J. Malmivuo & R. Plonsey, *Bioelectromagnetism: Principles and Application of Bioelectric and Biomagnetic Fields*. Oxford University Press, New York, 1995.
- [85] P. Kauppinen, "Application of lead field theory in the analysis and development of impedance cardiography," Ph.D. thesis, Tampere University of Technology, Tampere, Finland, 1999.
- [86] J. Jossinet, G. Kardous, "Physical study of the sensitivity distribution in multi-electrode systems", *Clin Phys Physiol Meas*, vol. 8, Suppl A: 33-7, 1987.
- [87] Boon K G and Holder D S, Effect of skin impedance on image quality and variability in electrical impedance tomography: a model study *Med. Biol. Eng. Comput.* 34 351-4. 1996.

- [88] Geddes L and Valentinuzzi M 1973 Temporal changes in electrode impedance while recording the electrocardiogram with 'Dry' electrodes *Ann. Biomed. Eng.* 1 356–67
- [89] Scholarly articles for Kauppinen, P., Hyttinen, J. & Malmivuo, J. Sensitivity Distribution Visualizations of Impedance Tomography Measurement Strategies. *International Journal*. 2006. Vol. 8, No. 1, pp: VII/1 - VII/9.
- [90] Robert H. Eckel, et al. Obesity and Heart Disease: A statement for healthcare professionals from the nutrition committee, American Heart Association, *Articles*, 1997. Vol. 96, Issue 9.
- [91] Lissner L, Heitmann BL. Dietary fat and obesity: evidence from epidemiology. *Eur J Clin Nutr.* 1995;49:79-90.
- [92] Rabkin SW, Mathewson FA, Hsu PH. Relation of body weight to development of ischemic heart disease in a cohort of young North American men after a 26 year observation period: the Manitoba Study. *Am J Cardiol.* 1977;39:452-458.
- [93] Matts JP, Buchwald H, Fitch LL, Campos CT, Varco RL, Campbell GS, Pearce MB, Yellin AE, Smink RD Jr, Sawin HS Jr, Long JM. Subgroup analyses of the major clinical endpoints in the program on the surgical control of the hyperlipidemias (Posch): overall mortality, atherosclerotic coronary heart disease (ACHD) mortality, and ACHD mortality or myocardial infarction. *J Clin Epidemiol.*

- [94] Ulrik Birgersson, *Electrial Impedance of Human Skin and Tissue Alterations: Mathematical Modeling and Measurements*, Karolinska Institutet, Stockholm, Swisston, 2012.

Appendix A: Matlab code

Script: real_data_inward_ring_or_patch.m

%%Set Parameters Here%%

skip = 4; %skip pattern

inj_current = 0.007; %unit is Amp

contact_imp = 10; %in ohm

hp = 1.15e-4; %hyperparameter

zeros = get_v_data(['/home/shell/Research/EIT/data/', 'zero_ignore1.txt']);
%zero_ignore0, zero_ignore1, zero_ignore2

%%Import data into vh,vi begin%%

datadir =

'/home/shell/Research/EIT/data/2016_08_11_liver_fat_gel_tank/skip14/50k/
gel/data/';

vi = get_v_data([datadir, 'data_0.txt']); %

vi = abs(vi);

%%Reconstruction FEM Model%%

% Make the model Netgen constructive solid geometries (CSG)

n = 32;

147

```
[shape_str, elec_pos, elec_shape, elec_obj] = mk_inward_ring_elec(n);
```

```
 %[shape_str, shape_str_inhomo, elec_pos, elec_shape, elec_obj] =  
 mk_patch_elec(8,4);
```

```
fmdl = ng_mk_gen_models(shape_str, elec_pos, elec_shape, elec_obj);
```

```
imdl = select_imdl(fmdl);
```

```
% Set stimulation patterns. Use meas_current
```

```
imdl.fwd_model.stimulation = mk_stim_patterns(n,1,[0 skip+1],[0 skip+1],  
 {'meas_current'},inj_current);
```

```
imdl.fwd_model.meas_select = zeros; % This is what we added compared to  
 before
```

```
%imdl.fwd_model = thorax_geometry( imdl.fwd_model, 3);
```

```
for i = 1:n;
```

```
    imdl.fwd_model.electrode(i).z_contact = contact_imp(i);
```

```
end
```

```
%show_fem( imdl.fwd_model, [0,1,0]);
```

```
ctrs= interp_mesh(imdl.fwd_model);
```

```
xe= ctrs(:,1); ye= ctrs(:,2);
```

```

re= sqrt(xe.^2+ye.^2);

region= re > 95; % for imdl

%liver=(( 28*ye + 95*xe>100*22) & re1<90); % for imdl

%%%%%%%%%%%%%%%%%%%%%%%%%%%%%%%%%%%%%%%%%%%%%%%%%%%%%%%%%%%%%%%%%%%%%%%%Set Solver Params Here%%%%%%%%%%%%%%%%%%%%%%%%%%%%%%%%%%%%%%%%%%%%%%%%%%%%%%%%%%%%%%%%%%%%%%%%

imdl.solve = @inv_solve_abs_GN_constrain ;
%@inv_solve_abs_GN_prior; % @inv_solve_abs_pdipm
@inv_solve_diff_pdipm;; %@tutorial151_diff_nonlinearGN; %

imdl.parameters.term_tolerance= 1.1e-5;

imdl.parameters.max_iterations=1;

%imdl.hyperparameter.value= hp*ones(1,length(imdl.fwd_model.elems)) +
hp*0*region';

imdl.hyperparameter.value= hp;

imdl.inv_solve.calc_solution_error = 0;

imdl.reconst_type= 'static';

imdl.RtR_prior = @prior_laplace; % @prior_tikhonov; %

imdl.parameters.min_s = 0.;

imdl.parameters.max_s = 1.6/4; %4;

%imdl.parameters.best_homog = 2;

% imdl.R_prior= @prior_TV;

```

```
% imdl = rmfield( imdl, 'RtR_prior');

imdl.jacobian_bkgnd.value= 0.1;%1.25;

%%%%%%%%%%%%%%%%%%%%%%%%%%%%%%%%%%%%%%%%%%%%%%%%%%%%%%%%%%%%%%%%%%%%%%%%Reconstruction begins%%%%%%%%%%%%%%%%%%%%%%%%%%%%%%%%%%%%%%%%%%%%%%%%%%%%%%%%%%%%%%%%%%%%%%%%

rec_img = inv_solve(imdl,vi);

solve_time = toc;

%%%%%%%%%%%%%%%%%%%%%%%%%%%%%%%%%%%%%%%%%%%%%%%%%%%%%%%%%%%%%%%%%%%%%%%%Result image display%%%%%%%%%%%%%%%%%%%%%%%%%%%%%%%%%%%%%%%%%%%%%%%%%%%%%%%%%%%%%%%%%%%%%%%%

img_max = (max(rec_img.elem_data)-min(rec_img.elem_data))/2;

img_ref = img_max;

PLANE = [inf,inf,0];

%figure;

calc_colours('defaults');

calc_colours('cmap_type','blue_black_red');

rec_img.calc_colours.npoints = 128*4;

%rec_img.calc_colours.ref_level = 0;

% rec_img.calc_colours.max_scale = img_max;
```

```

figure(1);

show_slices(rec_img,PLANE);

eidors_colourbar(rec_img);

% rot_im = imrotate(im,-90);

% mir_im = flip(rot_im);

% image(mir_im);

% eidors_colourbar(img_max,img_ref);

axis equal

axis off

axis tight

%%%%%%%%%%%%%%%%%%%%%%%%%%%%%%%%%%%%%%%%%%%%%%%%%%%%%%%%%%%%%%%%%%%%%%%%Reconstruction end%%%%%%%%%%%%%%%%%%%%%%%%%%%%%%%%%%%%%%%%%%%%%%%%%%%%%%%%%%%%%%%%%%%%%%%%

Script : simulation_inward_32_thorax.m

%clear;

n_elec= 32;

mdl= mk_common_model('j2C',32); %j2C

% Set stimulation patterns. Use meas_current

mdl.fwd_model.stimulation = mk_stim_patterns(32,1,[0 5],[0 5],{'meas_current'});

```

```
mdl.fwd_model = rmfield( mdl.fwd_model, 'meas_select');

mdl.fwd_model = thorax_geometry(mdl.fwd_model, 3);

for i = 1:n_elec

    mdl.electrode(i).z_contact = 0.1;

end

mdl.electrode(1).z_contact = 0.1;

%mdl.solve = @fwd_solve_1st_order;

%mdl.system_mat = @system_mat_1st_order;

mdl.get_all_meas = 1;

img1 = mk_image( mdl.fwd_model, 1); % make uniform conductive artery

img2 = img1;

scale = 10;

%select_fcn = inline('(x-60).^2+(y-0).^2<40^2','x','y','z');

%img2.elem_data = 1 + elem_select(img2.fwd_model, select_fcn);

% Identify block in centre

ctrs= interp_mesh(mdl.fwd_model);

xe= ctrs(:,1); ye= ctrs(:,2);

re1= sqrt((xe-12).^2+ye.^2);
```

```
liver=((5*ye + 7*xe>10*5 | 28*ye + 95*xe>95*22) & re1<110); % for mdl
```

```
fatty = 1;
```

```
img2.elem_data(liver) = fatty * 0.047 * scale;
```

```
re2= sqrt(2*(xe+60).^2+(ye-5).^2);
```

```
stomach = re2<40;
```

```
img2.elem_data(stomach) = 0.333* scale;
```

```
re3= sqrt(2*(xe+70).^2+(ye+25).^2);
```

```
re4= sqrt(2*(xe+60).^2+(ye-5).^2);
```

```
spleen = (re3<55 & re4>50);
```

```
img2.elem_data(spleen) = 0.067* scale;
```

```
re5= sqrt((xe).^2+(ye+70).^2);
```

```
spine = (re5<18);
```

```
img2.elem_data(spine) = 0.013* scale;
```

```
figure(1);
```

```
show_fem(img2,[1,0,0]);
```

```
img2.calc_colours.ref_level = 1;
```

```
eidors_colourbar(img2);

% Simulate Voltages and plot them

vh= fwd_solve(img1);

vi= fwd_solve(img2);

imdl= mk_common_model('h2C',32); %j2C

% Set stimulation patterns. Use meas_current

imdl.fwd_model.stimulation = mk_stim_patterns(32,1,[0 5],[0 5],{'meas_current'});

imdl.fwd_model = rmfield( imdl.fwd_model, 'meas_select');

imdl.fwd_model = thorax_geometry(imdl.fwd_model, 3);

imdl.jacobian_bkgnd.value = 1;

ctrs= interp_mesh(imdl.fwd_model);

xe= ctrs(:,1); ye= ctrs(:,2);

re1= sqrt((xe-12).^2+ye.^2);

liver=((5*ye + 7*xe>10*5 | 28*ye + 95*xe>95*22) & re1<110); % for imdl

%liver=(( 28*ye + 95*xe>100*22) & re1<90); % for imdl

hp = 0.5e-5; %hyperparameter for background other than liver
```

```
%  
  
imdl.solve = @inv_solve_abs_GN_constrain ; %@inv_solve_abs_GN_prior; %  
@inv_solve_abs_pdipm @inv_solve_diff_pdipm;; %@tutorial151_diff_nonlinearGN; %  
  
imdl.parameters.term_tolerance= 1.1e-5;  
  
imdl.parameters.max_iterations= 1;  
  
imdl.hyperparameter.value=hp;  
  
imdl.hyperparameter.value= hp*ones(1,length(liver)) + hp*0*liver';  
  
imdl.inv_solve.calc_solution_error = 0;  
  
imdl.reconst_type= 'static';  
  
imdl.RtR_prior= @prior_laplace; %@prior_tikhonov;  
  
imdl.parameters.min_s = 0.001;  
  
imdl.parameters.max_s = 4;  
  
% imdl.R_prior= @prior_TV;  
  
% imdl = rmfield( imdl, 'RtR_prior');  
  
  
dv = vh.meas-vi.meas;  
  
rec_img1 = inv_solve(imdl, -dv);  
  
figure(2);  
  
show_slices(rec_img1);
```

```
eidors_colourbar(rec_img1);

imdl.solve= @inv_solve_TV_pdipm;

imdl.R_prior= @prior_TV;

imdl.reconst_type= 'difference';

imdl.parameters.max_iterations= 1;

imdl.hyperparameter.value=1e-3;

imdl.parameters.term_tolerance= 1e-5;

imdl.parameters.keep_iterations= 0;

imdl.inv_solve_TV_pdipm.alpha1 = 0.01e-3;

imdl.inv_solve_TV_pdipm.beta =1e-4;

imdl.fwd_model = mdl_normalize(imdl.fwd_model, 1);

%imdl.jacobian_bkgnd.value = rec_img1.elem_data;

imdl.jacobian_bkgnd.value = 1;

%vh= fwd_solve(rec_img1);

rec_img = inv_solve(imdl, vh.meas, vi.meas);

rec_img.calc_colours.npoints = 128*4;
```

```
%rec_img.calc_colours.ref_level = 1;
```

```
figure(3);
```

```
h1 = subplot(1, 2, 1);
```

```
show_fem(img2);
```

```
h2 = subplot(1, 2, 2);
```

```
rec_img.elem_data = imdl.jacobian_bkgnd.value + rec_img.elem_data;
```

```
show_slices(rec_img1);
```

```
rec_img1.calc_colours.cb_shrink_move = [.4,.6,-0.08];
```

```
common_colourbar([h1,h2],rec_img1);
```

```
%eidors_colourbar(rec_img);
```

```
liver_mean_GN = mean(rec_img1.elem_data(liver)) * (1.5/scale)
```

```
liver_mean_TV = mean(rec_img.elem_data(liver)) * (1.5/scale)
```

```
%%%%%%%%%%%%%%%%%%%%%%%%%%%%%%%%%%%%%%%%%%%%%%%%%%%%%%%%%
```

Function : get_v_data.m

```
function v = get_v_data( filename )
```

```
% filename is the complete file path with file name
```

```
% v_i is the real part of data
```

```
% v_q is the imaginary part of data
```

```
delimiterIn = '\n';
```

```
v = importdata(filename,delimiterIn);
```

```
if length(v) > 1024
```

```
    v = v(2:end,:); %first line is number of voltages, 2048
```

```
end
```

```
end
```

```
%%%%%%%%%%%%%%%%%%%%%%%%%%%%%%%%%%%%%%%%%%%%%%%%%%%%%%%%%
```

```
Function : mk_inward_ring_elec.m
```

```
function [shape_str, elec_pos, elec_shape, elec_obj] = mk_inward_ring_elec(n)
```

```
l = 10;
```

```
r_outter = 101; %4.8
```

```
cyl = sprintf('cylinder(0,0,%f; 0,0,%f; %f)',-1*l,l,r_outter);
```

```
p1 = sprintf('plane(0,0,%f;0,0,1)',l/2);
```

```
p2 = sprintf('plane(0,0,%f;0,0,-1)', l/(-2));
```

```
shape_str = [ 'solid p1= ',p1,;\n'...
```

```
            'solid p2= ',p2,;\n'...
```

```
            'solid cyl = ',cyl,;\n'...
```

```
'solid mainobj = p1 and p2 and cyl -maxh=6.5;\n'...
```

```
'tlo mainobj -col=[1,0,0] -transparent;\n'
```

```
];
```

```
%electrodes
```

```
th = linspace(pi/2,pi/2-2*pi, n+1)'; th(end) = []; %number of electrode + 1
```

```
cs = [cos(th), sin(th)];
```

```
%elec_pos = [cs*r_balloon, 0*th, cs, 0*th];
```

```
elec_pos = [cs*r_outter, 0*th, cs, 0*th];
```

```
elec_shape= [10,10]; %5mm diameter copper wire electrode
```

```
clear elec_obj;
```

```
for i=1:n;
```

```
    elec_obj{i} = 'cyl';
```

```
end
```

```
%%%%%%%%%%%%%%%%%%%%%%%%%%%%%%%%%%%%%%%%%%%%%%%%%%%%%%%%%
```

```
Function : mk_patch_elec.m
```

```
function [shape_str, shape_str_inhomo, elec_pos, elec_shape, elec_obj] =  
mk_patch_elec(n_row,n_col)
```

```
%2.54mm male connector in saline
```

```

elec_spacing = 2.54; %spacing between two electrodes

m = n_row; %electrodes: number of rows (y)

n = n_col; %electrodes: number of columns (x)

x_dim = (n-1)*elec_spacing;

y_dim = (m-1)*elec_spacing;

x2 = (x_dim/2)*1.5; %upper right x corner of the model

y2 = (y_dim/2)*1.2; %upper right y corner of the model

z2 = 0; %upper right z corner of the model

x1 = -x2; %lower left x corner of the model

y1 = -y2; %lower left y corner of the model

z1 = -6; %lower left z corner of the model

% homogeneous model

brick = sprintf('orthobrick(%f,%f,%f;%f,%f,%f)',x1,y1,z1,x2,y2,z2);

shape_str_homo = ['solid top    = plane(0,0,0;0,0,1);\n' ...

    'solid mainobj= top and ',brick,' -maxh=0.8;\n'];

shape_str_inhomo = ['solid top    = plane(0,0,0;0,0,1);\n' ...

    'solid rod = ',brick,' and cylinder(0,0,-2; 1,0,-2; 1.5); tlo rod;\n' ...

    'solid mainobj= top and ',brick,' and not rod -maxh=0.5;\n'];

```

```
[elec_pos_x,elec_pos_y] = meshgrid(linspace(-x_dim/2,x_dim/2,n),linspace(y_dim/2,-
y_dim/2,m));
```

```
elec_pos = [ elec_pos_x(:), elec_pos_y(:), ones(size(elec_pos_x(:)))*[0,0,0,1] ];
```

```
elec_shape=[0.55,0.55]; %radius of electrode
```

```
elec_obj = 'top';
```

```
shape_str = shape_str_homo;
```

```
end
```

```
%%%%%%%%%%%%%%%%%%%%%%%%%%%%%%%%%%%%%%%%%%%%%%%%%%%%%%%%%%%%%%%%%%%%%%%%%
```

```
Function : show_sensitivity_field.m
```

```
function sens = show_sensitivity_field(fmdl,index)
```

```
%sensitivity field from assumed conductivity
```

```
img = mk_image( fmdl, 1);
```

```
J = calc_jacobian(img);
```

```
sens = J(index,:)./get_elem_volume(fmdl);
```

```
img_s = mk_image(fmdl, Sens);
```

```
show_slices(img_s,PLANE); %show slice at z=0 plane
```

```
eidors_colourbar(img);
```

```
%%%%%%%%%%%%%%%%%%%%%%%%%%%%%%%%%%%%%%%%%%%%%%%%%%%%%%%%%%%%%%%%%%%%%%%%%
```

```
Function : calculate_resolution.m
```

161

```
function [resolution,spread,img_processed] =  
calculate_resolution(img,r_tank,r_obstacle,thr_level)
```

```
% img is the reconstructed image, r_obstacle is the original obstacle in
```

```
% the simulation model or in experiment
```

```
if nargin < 4
```

```
    thr_level = 0.25;
```

```
end
```

```
area_sim = pi* (r_obstacle^2); %area of the true obstacle
```

```
area_tank = pi* (r_tank^2); %area of the tank
```

```
fmodel = img.fwd_model;
```

```
elem_data = img.elem_data;
```

```
elem_areas = calculate_elem_area(fmodel);
```

```
elem_data_processed = -1 * elem_data; % make the LOW conductivity positive and high  
negative
```

```
thr = thr_level * max(elem_data_processed);
```